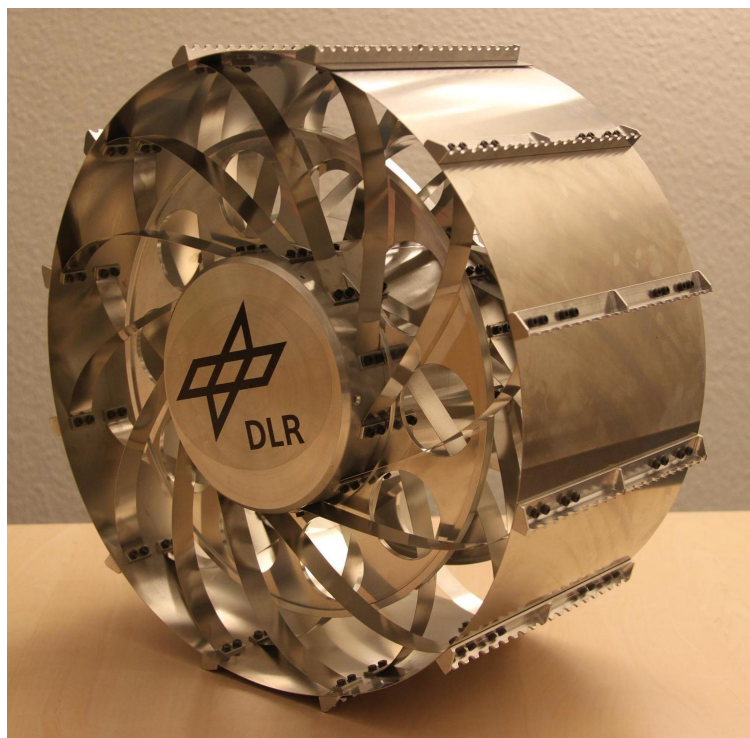


Concept Development and Design of a Flexible Metallic Wheel with an Adaptive Mechanism for Soft Planetary Soils



Christian Grimm

Master of Science
Space Engineering - Space Master

Luleå University of Technology
Department of Computer Science, Electrical and Space Engineering



CRANFIELD UNIVERSITY

CHRISTIAN GRIMM

SCHOOL OF ENGINEERING

MSc THESIS

CRANFIELD UNIVERSITY

SCHOOL OF ENGINEERING

MSc THESIS

Academic Year 2010-11

Christian Grimm

Concept Development and Design of a Flexible Metallic Wheel with an
Adaptive Mechanism for Soft Planetary Soils

Supervisor: Dr. Kevin Hughes (CU)
 Caroline Lange (DLR)
 Olaf Krömer (DLR)

July 1, 2011

This thesis is submitted in partial (45%) fulfillment of the requirements for the degree of Master
of Science

© Cranfield University 2011. All rights reserved. No part of this publication may be reproduced
without the written permission of the copyright owner.

ABSTRACT

Within the RIMRES project, a modular reconfigurable multi-robot system is being developed, which should demonstrate key technologies required for the exploration of challenging and difficult planetary terrain, as is found at the lunar south pole. For this purpose, key technologies in the area of autonomy, navigation and locomotion are being investigated and hardware engineered with the overall aim of having a system with interchangeable but compatible components, connected via unique mechanical and electrical interfaces.

This thesis was written in close collaboration with the German Aerospace Centre (DLR) at the Institute of Space Systems in Bremen and deals with the concept development and design of a flexible metal wheel with an adaptive mechanism for soft planetary soils.

The concept presented here builds upon the DLR wheel design developed for the ESA ExoMars mission, which incorporated flexible metal spokes to enlarge the wheels ground contact area. The new wheel design will be equipped with an intelligent sensor system to monitor and characterise soil properties. Dependent upon whether the rover is rolling over a hard or soft soil area, an integrated adaptable stiffness mechanism will then actively adjust the wheels flexibility. Equivalent to the inflation of a rubber tyre, by increasing the stiffness of the wheel the rolling resistance can be minimised when running on hard ground, whilst decreasing the wheels stiffness will maximise the tractive force when running over soft ground.

The work of this thesis in particular, deals with the concept development of such an adaptable system. The previous investigated ideas have been analysed in detail leading to a better understanding of their working principles. Subsequently, a new flexible wheel design was proposed based on the tensioned spoke wheel (bicycle wheel). With the help of computer based finite element analysis the non-linear deformation behaviour of the flexible elements was then evaluated.

It has been shown, that the new wheel design, with near-parabolic shaped tension blades, permits large deflections $\geq 10\%$ of the wheels diameter with low stress levels by maintain a relatively harmonic oval shape of the wheels tread. Also simulated were cases of high torques and side skid (driving across slopes). In each load case the wheels deformation behaviour was analysed and cross checked from a structural mechanics point of view. The results found with the simulation, achieving the best performance in terms of deflection distance and applied load, were then used to design and construct a new breadboard demonstrator wheel, which will undergo extensive testing at DLR in the forthcoming months.

DECLARATION

I hereby declare that I have written this thesis without any help from others and without the use of documents and aids other than those stated, and that I have mentioned all sources used and that I have cited them correctly according to established academic citation rules.

Place and date

Christian Grimm

CONTACT

Cranfield University
School of Engineering
Cranfield
Bedfordshire MK43 0AL
United Kingdom

Dr. Kevin Hughes
MSc Course Director / Lecturer
Dep. of Applied Mechanics and Astronautics
Crashworthiness, Impact and Structural
Mechanics Group
Cranfield University, BEDS, MK43 0AL
Phone: (+44) 1234 750111-5172
Email : k.hughes@cranfield.ac.uk

Christian Grimm
SpaceMaster R5
Mechelnbusch 3
D-22559 Hamburg
Phone: (+49) 162-1026019
E-Mail: cgrimm@cranfield.ac.uk
cgrimm@engineer.com

DLR - Deutsches Zentrum
für Luft- und Raumfahrt
Institute of Space Systems
Dep. of Exploration Systems
Robert Hooke-Str. 7
D-28359 Bremen

Caroline Lange
DLR-HBRY Dep. ES
Robert-Hooke-Str. 7
D-28359 Bremen
Phone: (+49) 421 24420-159
E-Mail: caroline.lange@dlr.de

Olaf Krömer
DLR-HBRY Dep. ES
Robert-Hooke-Str. 7
D-28359 Bremen
Phone: (+49) 421 24420-138
E-Mail: olaf.kroemer@dlr.de

MASTER THESIS

Concept Development and Design of a Flexible Metallic Wheel
with an Adaptive Mechanism for Soft Planetary Soils

"We can lick gravity, but the paperwork is sometimes overwhelming."

[*Wernher von Braun*]

PREFACE

Before I start the technical part of this thesis, I would like to make a couple of statements in order to explain how this paper came into existence. The work presented here, is a final image of my work and study over the past 2 years. Having finished my bachelor degree in 2009, I was on the verge of starting a job in industry, when I was encouraged by the people I talked with during this time to continue to a higher degree with the SpaceMaster Program. As it reflects my own perception from the experiences I made over the years I have spent in university, and because it fits well to the project of this thesis, there is a special quote I would like to mention which was originally delivered by John F. Kennedy at Rice University in Houston, Texas on September 12, 1962.

"We choose to go to the moon..., we choose to go to the moon in this decade and do the other things, not because they are easy, but because they are hard, because that goal will serve to organize and measure the best of our energies and skills, because that challenge is one that we are willing to accept, one we are unwilling to postpone, and one we intend to win, and the others, too."

This might have been directed to the space race at that time, but in general, it speaks to every single person who is willing to accept a personal challenge and to have the courage and ambition to do the very best to achieve the desired aim. "Not because it is easy, but because it is hard."

And doing the SpaceMaster program was indeed a challenge, bringing together students not only from Europe, but from all over the world. It is essential in our business to collaborate with many people from different technical, as well as different ethnic backgrounds, and trying to figure out the best ways to overcome personal endeavours and working in unity, was one of the major challenges during this time.

Looking back, I personally think that having "shared objectives" and "a common goal" is not only the key to achieve a specific problem but also the way to accomplish the goals of tomorrow!

Another quote I came along during this time was made by Anthony J. D'Angelo, who has done a lot of work in motivating young adults in higher education.

"Don't reinvent the wheel, just realign it."

First of all, it should be a general piece of advice specifically for engineers. Before inventing a completely new idea, take a look around and maybe find a pre-existing approach to develop further or to transform to the question at hand. One could argue that this is the very baseline of human development and evolution. Thanks to the work of our ancestors, we enjoy the comforts of modern life. And hopefully with the problems solved by us, our descendants will be able to explore new worlds and uncover even bigger questions.

Secondly, this quote summarises much of the work of this thesis. The idea of a metallic flexible wheel with its current ExoMars design was combined with the concept of a bicycle wheel, which in itself can be viewed as a masterpiece of the engineering work of the past century. The interesting thing about the bicycle wheel is that it was actually an unorthodox idea, carrying a compressive load with an element (a wire or a long thin rod) which only supports loads in tension. Invented around the 1870's, the load carrying mechanism of a tensioned spoke wheel is today not only used on bicycles, motorcycles and cars, but also on the massive constructions of Ferris wheels. The original Ferris Wheel (1893) was in fact the first to use the bicycle principle on such constructions.

In terms of planetary rover technology, the result of combining a flexible metal wheel with the tensioned spoke principle is a wheel capable of large deflections and carrying at the same time high loads by maintaining relative low stress levels in the material. In addition, the new design leaves enough space in order to accommodate the envisaged electromechanical system to adjust the wheels flexibility, which will be of great interest for future modular systems.

But enough of the chit chat, let us begin.

July 1st, 2011

Christian D. Grimm

CONTENTS

Preface	i
Acknowledgments	ix
List of Figures	xii
List of Tables	xiii
Abbreviations	xv
Symbols	xvi
I INTRODUCTION	1
1 OVERVIEW	3
1.1 Motivation	3
1.2 Objectives	4
1.3 Report Organization	5
2 SCIENTIFIC BACKGROUND	6
2.1 Terrestrial Locomotion	6
2.2 Rover Wheels in Space	7
2.2.1 Lunokhod	8
2.2.2 Modular Equipment Transporter	9
2.2.3 Lunar Roving Vehicle	10
2.2.4 Microrover Flight Experiment	10
2.2.5 Mars Exploration Rovers	11
2.2.6 Mars Science Laboratory	12
2.2.7 ExoMars	13
2.3 Wheel-Soil Interaction	14
2.3.1 Soil Mechanics	14
2.3.2 Rigid vs Flexible Wheels	15
2.3.3 Hard and Soft Soil Conditions	20
2.3.4 Adaptive Wheel Design	22
2.4 Summary	23
II SYSTEM DESIGN	25
3 CONCEPT ASSESSMENT	27
3.1 Baseline Wheel Design	27

3.2	RIMRES Requirements	30
3.2.1	Forces and Moments	30
3.2.2	Wheel Operation Mode	31
3.3	Assessment of Previous Concepts	32
3.3.1	Pulling Strings	33
3.3.2	Concept 3 - Revision	34
3.3.3	Linear Moving Pins	39
3.3.4	Concept 2 - Revision	40
3.3.5	Radial Springs	44
3.3.6	Concept 1 - Revision	44
3.4	Assessment of Flexible Spokes	45
3.4.1	Waved Bands	45
3.4.2	Shear Plates	46
3.5	Adaptive Mechanism	48
3.6	Statement	51
4	WHEEL DESIGN	53
4.1	Requirements Review	53
4.1.1	Load Cases	53
4.1.2	Materials and Stress Criterion	54
4.1.3	Wheel Stiffness and Deflection	55
4.2	Analysis Method	57
4.3	Shear Plates	59
4.3.1	Buckling Columns	59
4.3.2	Deflection Curve Models	60
4.3.3	Analysis	63
4.4	Tension Blades	70
4.4.1	Variant A - End Curved	70
4.4.2	Variant B - Near-Parabolic Curved	75
III	CONCLUSIONS	85
5	RESULTS	87
6	DISCUSSIONS	89
7	CONCLUSION	93
	Bibliography	97
	APPENDIX	A-2
A	STRESS LEVEL DUE TO SIDE SKID	A-3
B	CAD MODEL	A-5
C	DATA SHEETS	A-9

ACKNOWLEDGMENTS

F*irst* I must thank my academic advisor Dr. Kevin Hughes. He accepted my ideas and plans for this thesis without question and was always keen to follow my progress. I thank him for his help and input, for his always friendly and fair-minded attitude and for all the encouragement.

Thanks to Dr. Tim van Zoest, Head of the DLR Department Exploration Systems. I am very glad that he gave me the opportunity to do my thesis on such an interesting and challenging space project.

A very special thanks to my project supervisors, Caroline Lange and Olaf Krömer, for all their guidance and assistance. Especially the fact that they entrusted me with the task of the wheel design and accepted my ideas and the approaches I took during the concept trade-off and design phase. They confirmed my passion and ability in engineering and showed me once more that my work and ambition are directed in the right way.

Special thanks also to my colleague and mentor, Dr. Marco Scharringhausen, for all the support and technical advise.

Thanks to my collaborators from the Hochschule Bremen - University of Applied Sciences, Jens Wolter and Christian Oeckermann. Only with their support was it possible to perform the non-linear analysis of the new wheel design and to refine the concept to its current state.

Thanks to my fellow student and proof reader, Leigh Glasgow, who helped to maintain a readable structure of this thesis and to diminish the number of typographical and grammatical errors.

And big thanks goes also to the whole DLR-RY-ES team, (in alphabetical order) Jens Große, Tra-Mi Ho, Eugen Ksenik, Roland Rosta, Silvio Schröder, Susanne Wagenbach and Lars Witte. I have already experienced the work in other departments and companies and can therefore truly say, that the teamwork encountered here was both good-natured and professional alike.

Finally, I have to thank once more my parents Detlef Grimm and Helga Grimm. Without these two most important persons in my life I would have never been able to come to this point. Always listening, supporting and faithfully accepting my decisions to follow a path I have chosen myself. I know this path is not always easy but it is straightforward and each step well deliberated. I am very grateful for everything you have done for me so far, thank you both so much!

LIST OF FIGURES

1.1	RIMRES rover	4
2.1	Types of animal locomotion	7
2.2	Lunokhod	9
2.3	Modular Equipment Transporter	9
2.4	Lunar Roving Vehicle	10
2.5	Sojourner	11
2.6	Mars Exploration Rovers	12
2.7	Curiosity	12
2.8	ExoMars rover	13
2.9	Mechanics of rigid and flexible wheels	15
2.10	Equivalent stiffness of a flexible wheel	16
2.11	Effect of grousers	17
2.12	Other flexible wheel designs	18
2.13	Fundamental load-carrying mechanics of wheels	19
2.14	Variation of total rolling resistance	20
2.15	Motion resistance of a flexible wheel on soft sand	21
2.16	RIMRES scenario	22
3.1	Baseline wheel	28
3.2	RIMRES rover configuration	31
3.3	RIMRES wheel operation mode	32
3.4	Concept 3 - Pulling Strings principle	33
3.5	Concept 3 - BB setup	34
3.6	Concept 3 - Stiffness evolution	35
3.7	Concept 3 - Stiffness variation	37
3.8	Concept 3 - Deformation variation	37
3.9	Concept 3 - Increased tensile forces at fixation points	38
3.10	Concept 2 - Linear Moving Pins principle	39
3.11	Concept 2 - Baseline wheel modification	40
3.12	Concept 2 - Stiffness evolution	41
3.13	Theory of a simply supported beam	41
3.14	Concept 2 - Secondary effect	42
3.15	Concept 2 - Stiffness variation	43
3.16	Concept 2 - Deformation variation	43
3.17	Concept 1 - Radial Springs principle	44
3.18	Waved spoke plastic distortion	45
3.19	Shear plate alternative	46
3.20	Shear plate feasibility test	47
3.21	Spring-damper-system	49
3.22	Electro-mechanical solenoid	50

4.1	Load Cases	54
4.2	Shear plate wheel	57
4.3	Compliant Mechanisms	58
4.4	Columns of buckling	59
4.5	Shear plate deflection models	60
4.6	Shear plate FE-model	64
4.7	FEA - Shear Plate concept	65
4.8	Stress/strain diagram	66
4.9	Shear displacement	67
4.10	Bicycle wheel principle	70
4.11	Tension blades single spoke analysis variant A.1	72
4.12	Tension blades single spoke analysis variant A.2	72
4.13	Tension blades single spoke analysis variant A.3	73
4.14	Tension blades single spoke analysis variant A.4	73
4.15	Tension blades full wheel analysis variant A	74
4.16	Tension blades variant B	75
4.17	Resistance of the wheel	77
4.18	Theory of a cantilever beam	78
4.19	Load Case 1 (xy-plane)	80
4.20	Load Case 1 (perspective view)	80
4.21	Load Case 2 (xy-plane)	81
4.22	Load Case 2 (perspective view)	81
4.23	Load Case 3 (xy-plane)	82
4.24	Load Case 3 (perspective view)	82
4.25	Comparison GCP-1	83
4.26	Comparison GCP-2	83
B.1	DLR INFLATE wheel design	A-7

LIST OF TABLES

2.1	Comparison of robotic mobility systems	8
2.2	Soil parameter	14
3.1	Baseline wheel characteristics	29
3.2	Baseline wheel materials	29
3.3	RIMRES mass budget	29
3.4	RIMRES wheel dimensions	30
3.5	Results of concept 3 BB testing	34
3.6	Results of concept 3 data calibration	35
3.7	Trade-off decision matrix	51
4.1	Wheel stiffness and deflection	56
4.2	Shear plate deflection models	62
4.3	Tension blades single spoke bending test	71
6.1	Tension blades - Pros and Cons	91

ABBREVIATIONS

BB	Breadboard
BC	Boundary Condition
Bevometer	Bekker Value Meter
BSD	Bump Stop Disc
C	Concept
CAD	Computer Aided Design
Caltech	California Institute of Technology
COTS	Commercial off-the-shelf
CU	Cranfield University
DC	Direct Current
Decco	Detroit Coil Company
DFKI	Deutsches Forschungszentrum für Künstliche Intelligenz
DLR	Deutsches Zentrum für Luft- und Raumfahrt
EADS	European Aeronautics Defense and Space company
ES	Explorations Systeme
ESA	European Space Agency
FE	Finite Element
FEA	Finite Element Analysis
GCP	Ground Contact Point
INFLATE	INtelligent FLExible Adaptive TEnsion-blades
IRS	Institut für Raumfahrtssysteme
JPL	Jet Propulsion Laboratory
LRV	Lunar Roving Vehicle
LSS	Locomotion Sub-System
MARUM	Zentrum für Marine Umweltwissenschaften
MDA	Macdonald Dettwiler and Associates, Canada
MER	Mars Exploration Rover
MET	Modular Equipment Transporter
MFEX	Microrover Flight EXperiment
Michelin	Manufacture Française des Pneumatiques Michelin
MOVE!	Autonomous moving vehicle for underwater investigations (University of Bremen/MARUM)
MSC	MSC Software (formerly: MacNeal-Schwendler Corporation)
MSL	Mars Science Laboratory
MSR	Mars Sample Return
NASA	National Aeronautics and Space Administration
NPC	Near-Parabolic Curve
N/S	Not specified
OSZ	Oerlicon Space AG, Zürich / Switzerland (now RUAG Space)
RIMRES	Reconfigurable Integrated Multi-Robot Exploration System
RUAG	RUAG Holding AG (formerly: Project "RüstungsUnternehmen-AktienGesellschaft" of the swiss government)
RY	Raumfahrt Systeme
TBC	To be confirmed
TBD	To be determined
TPM	Tractive Prediction Model
TRL	Technology Readiness Level
w/o	without
wrt	with respect to
ZARM	Zentrum für angewandte Raumfahrttechnologie und Mikrogravitation

SYMBOLS

ROMAN LETTERS

Symbol	Name	Symbol	Name
A	Area	c	Soil cohesion
D	Diameter (wheel)		Characteristic spring constant
E	Modulus of elasticity	b	Width
	Energy	d	Diameter (hub)
F	Force		Distance
G	Shear modulus	g	Gravity acceleration
H	Tractive force		Air gap
I	Second moment of area	h	Hight
	Electronic current	k_ϕ	Frictional soil modulus
K	Effective length factor	k_c	Cohesion soil modulus
L	Length	l	Length
	Inductance	l_t	Contact length
M	Moment	m	Mass
N	Number	n	Soil deformation exponent
P	Power		Number
R	Resistance	p_{gr}	Ground pressure
	Reaction force		Equivalent Stiffness
S	Slippage	r	Radius
	Rod (Stab)		Element length
T	Torque	s	Slope/Curve length
W	Wheel load	t	Thickness
		u	Displacement in x-direction
		v	Displacement in y-direction
DP	Drawbar Pull	w	Beam deflection
FS	Factor of Safety	z_0	Sinking coefficient
F_G	Total System Mass		
F_s	Side skid force		
R_m	Tensile strength		
$R_{p0.2}$	Yield strength		

GREEK LETTERS

Symbol	Name
ϕ	Internal friction angle
κ	Soil shear def. modulus
τ	Shear strength Shear stress
σ	Normal stress
σ_v	Von Mises stress
σ_y	Yield stress
γ	Shear strain
ε	Normal strain
η	Efficiency
ω	Angular velocity
δ	Wheel deflection
ν	Poisson's ratio Speed
μ_0	Absolute permeability
μ_s	Friction coefficient (static)

INDICES

Symbol	Name	Symbol	Name
M	Momentary	adj	Adjusted
N	Nominal	bs	Bump stop
		cat	Catenary
b	Bulldozing	eqs	Equivalent system
	Blade	gr	Ground
	Bending	is	Inner spoke
c	Compression	mv	Measured value
e	Element	os	Outer spoke
f	Field	seg	Segment
g	Gravity Grouser		
h	Hysteresis Hub Half		
r	Ring		
s	Spoke		
w	Wheel		

Part I

INTRODUCTION

1

OVERVIEW

This master thesis was written in collaboration with the German Aerospace Centre (DLR) at the Institute of Space Systems (IRS) in Bremen as a contribution to the Reconfigurable Integrated Multi-Robot Exploration System (RIMRES) project, which is currently being undertaken in close cooperation with the German Research Center for Artificial Intelligence (DFKI) and the Center of Applied Space Technology and Microgravity (ZARM). The following describes the overall project goals and the distribution of development tasks between the collaborating partners.

1.1 Motivation

Within the RIMRES project, a modular reconfigurable multi-robot system is being developed, which should demonstrate key technologies required for the exploration of challenging and difficult planetary terrain, as is found at the lunar south pole. For this purpose, key technologies in the area of autonomy, navigation and locomotion are being investigated and hardware being engineered, with the overall aim of having a system with interchangeable components, connected via unique mechanical and electrical interfaces. The demonstrator which is to be built, shall realise the basic functions of a typical exploration system, i.e. providing locomotion, energy supply, data handling and the performance of scientific investigations. In addition, the system shall be designed to be reconfigurable, i.e. being able to adapt its configuration to undertake urgent tasks and changing environmental conditions. This adaptabilities will be achieved via a two-robot team, consisting of a rover and a scout, both of which are equipped with the aforementioned mechanical and electrical interfaces for configuration change.

The rover in Figure 1.1 is being developed by DFKI as the prime contractor. DLR provides the wheel design, drawing upon many years of experience in the development and testing of flexible wheels, examples of which are used on the ExoMars Rover to be launched in 2018. The goal of the wheel development within the RIMRES project is based on the overall project objective of being reconfigurable/adaptable. Thus, an intelligent wheel has been proposed, which will allow an effective, flexible and robust locomotive performance of the rover whilst taking into consideration the minimisation of energy consumption and the maximisation of tractive force for varying system masses and soil conditions.

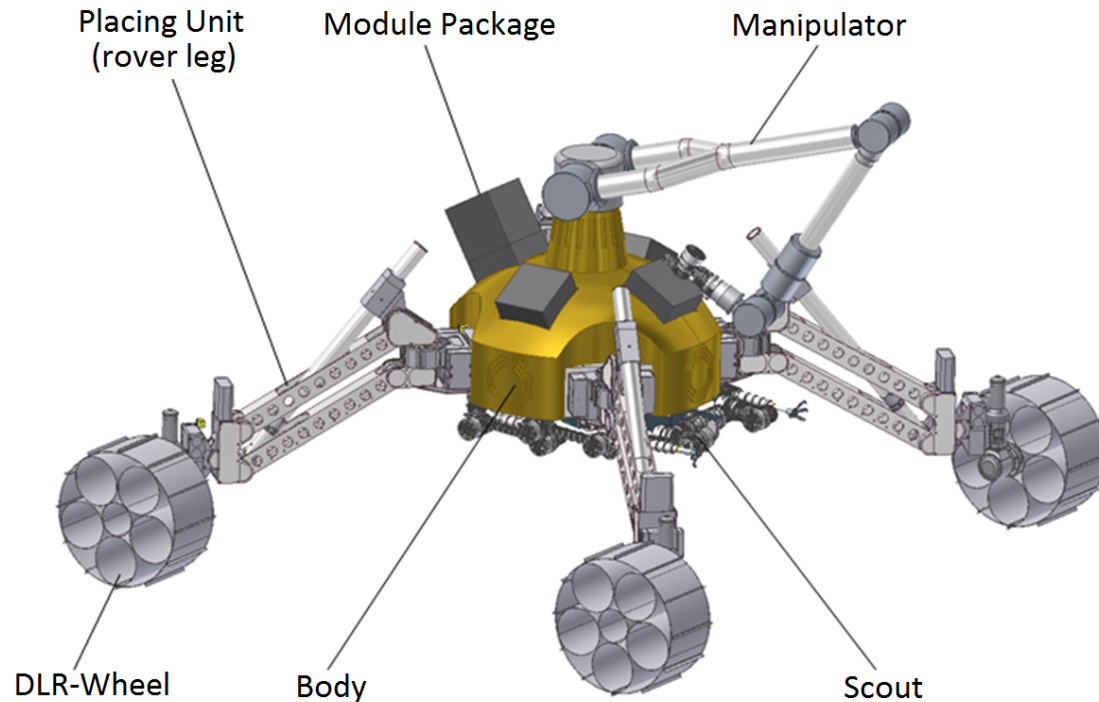


Figure 1.1: The rover for the planned Reconfigurable Integrated Multi-Robot Exploration System (RIM-RES) showing the rovers principle of a 4-legged walking excavator. The manipulator arm on top of the rovers body is used to place the different payloads, which are enclosed in standardized module packages, on and off the rover for transportation. Underneath the rover a 6-legged walking scout is carried, which is able to detach itself to autonomously investigate areas of rough terrain or slopes with high inclination. (Credit: DFKI)

1.2 Objectives

The main objectives and tasks of this master thesis were outlined as follows:

- To define requirements for the stiffness adaptation mechanisms.
- To assess the previously investigated options for variation of the wheel's stiffness.
- To develop (if necessary) a new design of a flexible metal wheel, including the design of the spokes and the concept of an adaptation mechanism.
- To perform a detailed mechanical design of the wheel and the adaptation mechanism, using required engineering methods.
- To produce 3D models, 2D production drawings and undertake the selection and purchase of components.
- To document all work to the appropriate standard (e.g. by means of requirements or system design documents as well as a final thesis report).

1.3 Report Organization

To structure the work and to make it convenient for the reader, this report is organized in three parts.

1. Introduction – Overview and background information
2. System Design – The engineering work of this thesis
3. Conclusions – Results, discussions and conclusion, list of used references

The first part "Introduction" provides an overview of the project and this report. The scientific background is outlined to give detailed information concerning robotic rover exploration in general as well as information about wheel-soil interactions, which form the baseline for the later system design.

The second part "System Design" shows the main work of this project, and deals with the development and design of the flexible metallic wheel and the adaptation mechanism to adjust the stiffness for locomotion on soft planetary soils. The procedure used is stated, leading to a first concept trade-off where the previous work is reviewed in detail and critically analysed, before providing a final recommendation which concept to pursue for detailed design and manufacture. Here can also be found the FE analysis for the new wheel design.

Part three "Conclusions" summarises the results obtained during this work. The discussion relates the objectives of the project to the reviewed literature and lists the achievements of this thesis. The report is then concluded with a final statement.

2

SCIENTIFIC BACKGROUND


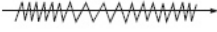

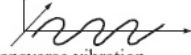
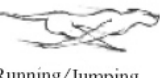



This chapter provides background information in regards to terrestrial locomotion principles and their affect on robotic locomotion. A short summary of past and future planetary rover missions is given with a special focus on the technology of the rovers locomotion systems. Furthermore, the difference between rigid and flexible wheels is outlined explaining the effect of how these wheels interact with the soil.

2.1 Terrestrial Locomotion

If one is being asked to name the most dominant type of locomotion on land, the answer would unquestionable be the rolling motion of a wheel. The concept of land locomotion was not invented by mankind, however, but materialized through nature in many forms. Most interestingly though, with the exception of the wheel!

Through evolution, nature has developed different types of locomotion on land, including crawling, sliding, running and jumping. The concept of walking, though similar on first glance to running, might be seen as entirely different. For running and jumping, a simplified pattern could be compared to a multi-joint pendulum. The pattern of walking, however, is more closely related to the mechanics of a rolling polygon, in which the length of the polygons sides equal the step length of a walking person (Figure 2.1). The smaller the step size, the shorter the side length of the polygon. So it could be concluded that the biped nature almost ideally approached the concept of a wheel [1].

Nature perfected the walking mechanism, which is superior in soft soil conditions to a pneumatic tyre. Nevertheless, the wheel has become the universal means of locomotion in the human world, because of its overall efficiency and relative simplicity. For this reason, the first form of robot locomotion, even for semi-rough terrain, has been focused on the use of wheels.

Type of motion	Resistance to motion	Basic kinematics of motion
Crawl 	Friction forces	Longitudinal vibration 
Sliding 	Friction forces	Transverse vibration 
Running/Jumping 	Loss of kinetic energy	Oscillatory movement of a multi-link pendulum 
Walking 	Gravitational forces	Rolling of a polygon 

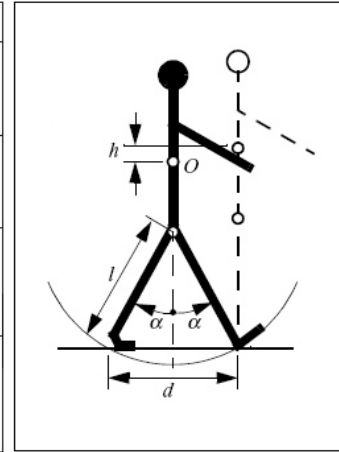


Figure 2.1: Types of animal locomotion depending on the type of mechanism used. Locomotion through running and jumping, or the swinging action of extremities, may be compared to a multi-joint pendulum. Sliding and crawling involve the oscillatory movement of the driving elements in the plane of translation. Walking, in an extreme case, may be compared to the rolling of a rimless wheel, with the legs (spokes) supporting the load. (Reproduced from [1])

2.2 Rover Wheels in Space

A rover, which could also be termed as an off-road or cross-country vehicle, is generally used in areas with rough terrain, steep slopes and no dedicated driving paths. As for robotic rovers, they are designed particularly to explore undiscovered ground. On Earth, robotic rovers are used primarily in situations where a place is not accessible for a human body (e.g. inspecting pipes) or if it is thought to be too dangerous for humans (mined areas). This in particular, makes them also extremely valuable for planetary and lunar exploration, opening the possibility to get a first impression of the probable hostile environment, performing basic measurements and validating the possibility for later human exploration.

Different locomotion principles for movable robots have been proposed and studied over the last few decades. A state-of-the-art survey, conducted in 2010 by the DLR Institute of Robotics and Mechatronics in Oberpfaffenhofen [2], listed the most eminent forms and compared them against each other based on selected parameters, including, amongst others, slope climbing capability, energy consumption and technology readiness level (TRL). The results showing the advantages and disadvantages of the considered systems can be seen in Table 2.1.

According to this survey, the locomotion system that is the least complex, most reliable and with the highest energy and cost efficiency is a wheeled system. For these reasons, all rover missions in space, so far have used wheels. And future missions will continue to use wheeled systems unless an alternative is required for a specialised task. In light of the RIMRES project, it should be noted that a hybrid system which combines the advantages of two systems whilst at the same time minimising or canceling the disadvantages of the other, would be the most optimal solution.

Table 2.1: Advantages and disadvantages of robotic mobility systems for space applications. (Reproduced from [2])

System	Advantages	Disadvantages
Wheels	<ul style="list-style-type: none"> • Better speed in even terrain • Simple and mature technology • Adequate redundancy (mobility) • High payload capacity • Relatively low power consumption rates and energy efficient 	<ul style="list-style-type: none"> • Relatively low slope climb capacity due to wheel slippage • Obstacle traverse capability relatively low compared to other concepts
Tracks	<ul style="list-style-type: none"> • Good terrain capability • Technology well understood in terrestrial applications • Better traction capability on loose soil • Handles large hinders, small holes, ditches better • Good payload capacity 	<ul style="list-style-type: none"> • Inefficient due to friction of tracks • Low speed operation • Slip turning and friction • Low redundancy, jamming of parts and prone to failure
Legs	<ul style="list-style-type: none"> • Highly adapted to uneven terrain and hence better obstacle and slope traverse capability 	<ul style="list-style-type: none"> • Mechanically complex (Control of walking) • Slow mobility • Impact after each step • Poor payload weight-to-mechanism weight ratio
Hoppers	<ul style="list-style-type: none"> • Better obstacle traverse capabilities • can enable large scale exploration due to better speed 	<ul style="list-style-type: none"> • Impact during landing after hopping, large risk of failure
Hybrids	<ul style="list-style-type: none"> • Shares the advantages of two locomotion concepts 	<ul style="list-style-type: none"> • More complex • Low technology maturity

2.2.1 Lunokhod

The first mobile vehicle on the surface of a planetary body other than the Earth was the unmanned and remotely controlled lunar rover Lunokhod 1 (Figure 2.2) launched and operated by the Soviet Union in 1970/71. It was followed two years later by a second, nearly identical vehicle, Lunokhod 2. Both rovers were comparatively large with masses above 700 kg and a length and height of 2.2 x 1.4 m. The rovers activities included high resolution TV imaging and lunar soil analysis [3].

Although the name translates to "moon walker", Lunokhod was an 8-wheeled rover. Each of its rigid wheels, 510 mm in diameter and 200 mm in width, was independently controllable allowing for skid steering usually employed by terrestrial tracked vehicles. This was adopted for simplicity reasons and in order to achieve an almost 0-degree turning radius [4]. The wheels featured a steel wire mesh as the running surface and three titanium rings interconnected by titanium grousers to enhance tractive performance. Bicycle-like steel spokes connected the rim to the hub making the design very strong and stiff whilst also being very lightweight [5].

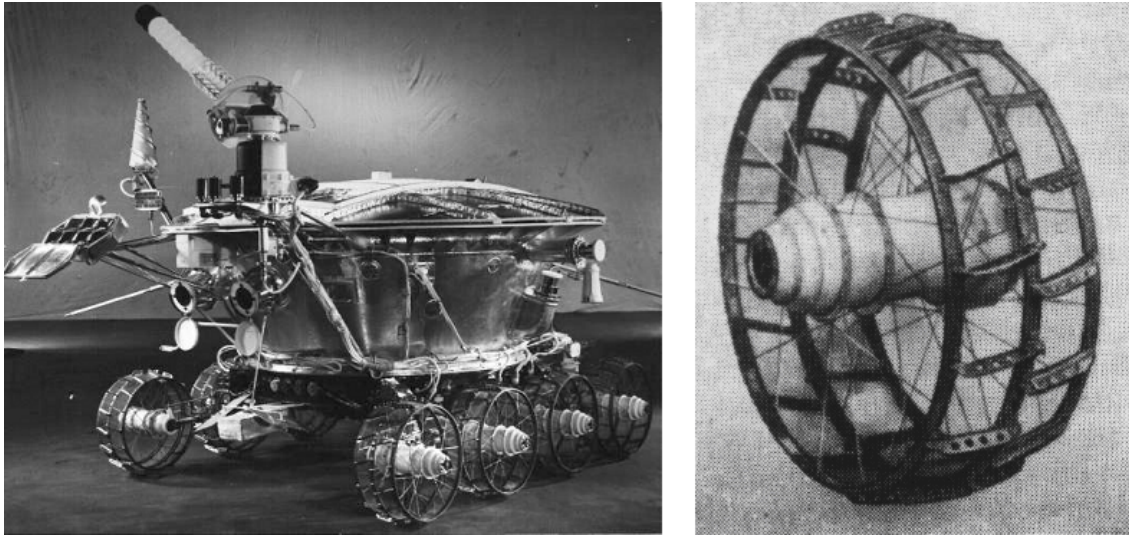


Figure 2.2: Left: Lunokhod series Soviet Moon exploration robot vehicle. Right: Lunokhod wheel. (Courtesy Lavochkin Association)

2.2.2 Modular Equipment Transporter

The first American wheels to touch the lunar surface were, strictly speaking, not part of a rover. The Modular Equipment Transporter (MET) shown in Figure 2.3, was an un-powered, hand-drawn rickshaw-type cart, which was used by the astronauts on the Apollo 14 mission in early 1971 to carry the various geology tools, instruments and lunar samples. The 2-wheeled trailer, equipped with a pulling handle and two resting posts, was able to support up to 75 kg of extra load and is to this day the only planetary mobile vehicle to have been equipped with a pneumatic rubber tyre [4].

The wheels had a diameter of 400 mm and 100 mm width when unloaded. Filled with dry nitrogen gas, the inflation pressure relative to the surrounding vacuum was 0.1 bar. The tyres were designed to have a smooth surface and did not require a tread or grousers due to the fact that no driving torque needed to be transmitted [4]. The design of rubber tyres is also viable in a vacuum but requires a demanding development process to ensure that

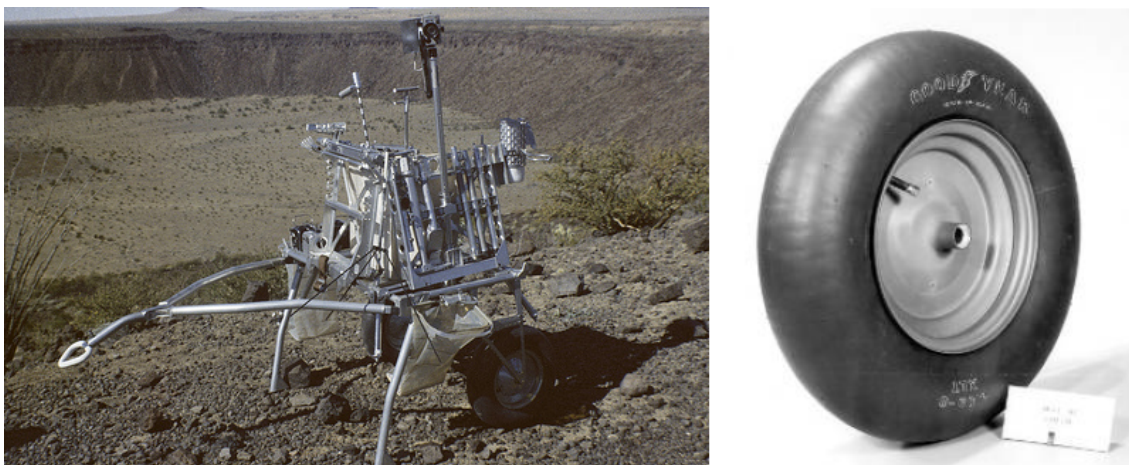


Figure 2.3: Left: A prototype of the Modular Equipment Transporter used by the Apollo 14 astronauts during their geological and lunar surface simulation training in the Pinacate volcano area of northwestern Sonora, Mexico. Right: MET wheel by Goodyear. (Courtesy NASA)

the predetermined desired inflation pressure, which critically determines tyre deflection under load and thus ground contact and sinking, is achieved in operation [6]. Plastic materials have, however, the drawback of higher degradation due to high temperature gradients, solar and cosmic rays and the phenomenon of out-gassing in vacuum.

2.2.3 Lunar Roving Vehicle

The Lunar Roving Vehicle (LRV) shown in Figure 2.4, used during the American Apollo missions 15, 16 and 17 between 1971 and 1972, was the first and so far only manned planetary rover ever developed. It served to carry the crew of two astronauts with their associated gear, including their space suits, dedicated geology equipment and samples. The intention of the LRV was to allow long distance travel for an area-wide exploration around the landing site.

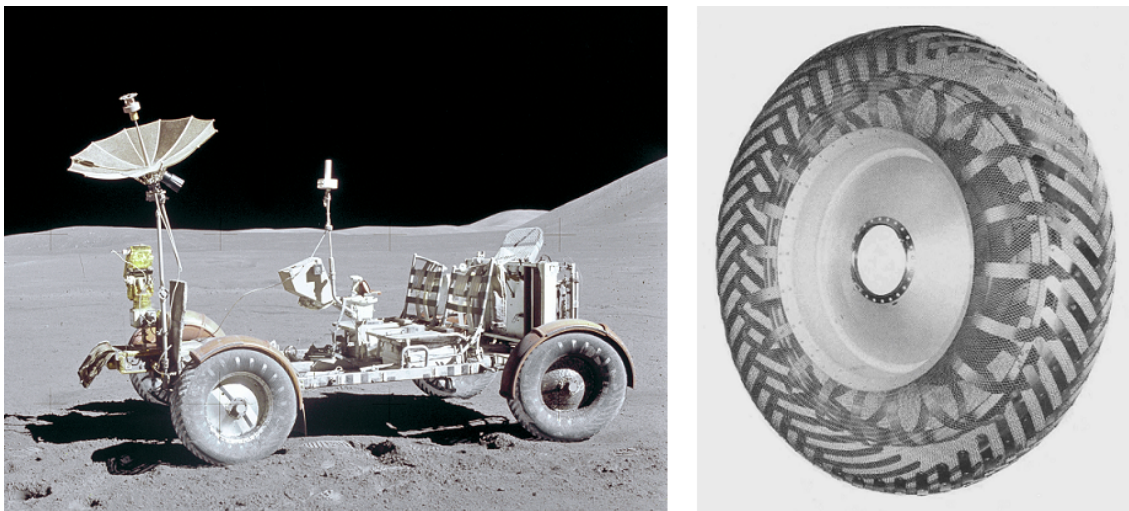


Figure 2.4: Left: Lunar Roving Vehicle photographed alone against the lunar background during Apollo 15. Right: LRV wheel. (Courtesy NASA)

All four wheels of the LRV were driven individually by a DC motor/harmonic drive gear combination allocated within the wheel hub. The wheels were constructed out of a rigid wheel disc surrounded by a fabricated steel wire mesh. The undeformed diameter of the wheel was 810 mm which was deflected by 75 mm under the lunar wheel load, but at higher loading conditions (e.g. running against rocks), the tyre was able to deflect all the way to an internal titanium bump stop [7]. The LRV wheel design represented a flexible wheel concept imitating the deflection capabilities of a pressurized rubber wheel allowing deformation under loading and therefore increasing the contact area on the ground. This, and the flat chevron-shaped titanium cleats covering the wire mesh improved tractive performance on the uneven lunar terrain (see Section 2.3).

2.2.4 Microrover Flight Experiment

After the Moon had been explored to some extent, the next point of interest was our neighboring planet Mars. The Mars Pathfinder mission was originally developed to include the means of a mars sample return to study soil properties here on Earth. Due to cost reductions, however, this was reduced to an one way mission only, but including the instrumentation to perform simple in-situ measurements to examine the chemical composition of the Martian rocks. The Microrover Flight EXperiment (MFEX), later renamed

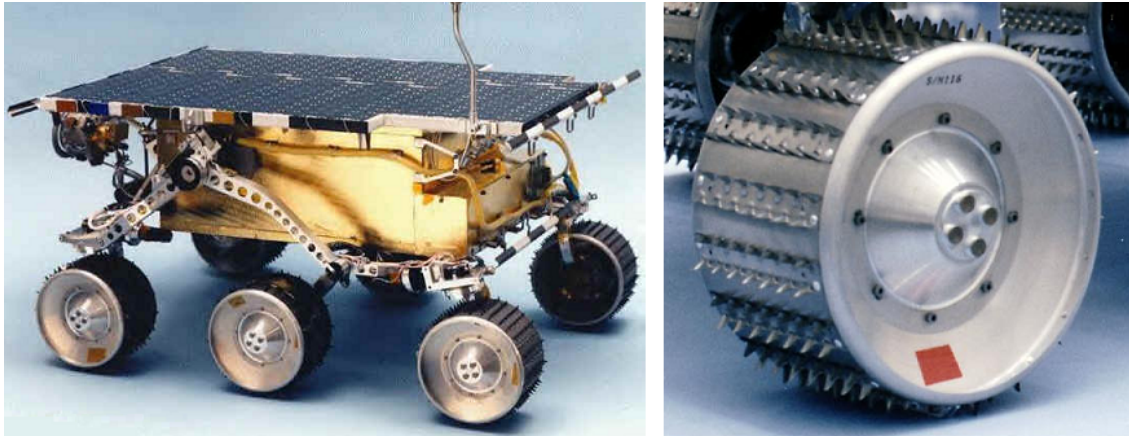


Figure 2.5: Left: The Sojourner rover at the end of its assembly and before integration to the main Pathfinder spacecraft. Right: Sojourner wheel. (Courtesy NASA/JPL-Caltech)

Sojourner (Figure 2.5), touched down in the summer of 1997 and became the first mobile vehicle to operate on the Martian surface. The technology pioneered by Sojourner would be adopted by many successive missions.

When deployed the rover was 650 mm long, 480 mm wide and 300 mm tall with a ground clearance of 130 mm. The total mass was approximately 10.5 kg. With the rocker-bogie suspension system, developed by the JPL, Sojourner was able to overcome obstacles as high as 1.5 wheel diameters. The special ability of these rocker arms was that they distributed the weight of the rover equally on all 6 wheels, which harmonised the torque transmission to the ground. The four corner wheels were steerable making it possible for the rover to turn on the spot, which was thought to be essential for maneuvering on rocky terrain [8].

All six wheels were driven individually by an actuator (brushed DC motor & planetary gearbox) installed in the hub of the comparably wide wheel, having a diameter of 130 mm and a width of 80 mm. The wheel design was cylindrical, structurally closed and rigid with sharp, parallel cleats attached to the rim improving grip on rocks and tractive force on soft soils [9].

2.2.5 Mars Exploration Rovers

The next expedition to the red planet were the Mars Exploration Rovers (Figure 2.6), Spirit (MER-A) and Opportunity (MER-B), which were basically scaled up versions of Sojourner. The rovers were 2.25 m wide, 1.5 m long and 1.5 m tall, including the deployed solar panels and camera mast. The total mass was approximately 180 kg each. Like Sojourner, they utilised a rocker-bogie suspension system and a 6-wheel drive with the four corner wheels being steerable.

Both rovers landed, 3 weeks apart from each other, in January 2004 and had the primary objective of performing field geology on Mars, along with traverses of up to 1 km over a period of 90 Martian days. Both rovers, however, exceeded the planned mission time by far, living through some difficult problems (see Section 2.3.3). With Opportunity currently still operational, the two rovers have covered a combined distance of more than 37 km (as of May 2011) [10].



Figure 2.6: Left: Researchers at JPL simulate the conditions faced by the rover Spirit on Mars, where it was stuck in loose soil, to find the best way to help free it. Right: MER wheel. (Courtesy NASA/JPL-Caltech)

The wheels of the MER's were of a rigid design with a diameter of 250 mm and a width of 160 mm. The spiral-like structure connecting the tyre to the hub served to absorb shocks when driving against rocks or dropping down steps. A particular design feature of the wheels were the curved running surfaces, in order to accommodate the steering actuators within the wheel envelope. In expense of mobility performance, the cleats on the wheels were shallow with no sharp edges, a design compromise required to lower the risk of the wheels picking up lander airbag material [11].

2.2.6 Mars Science Laboratory

The Mars Science Laboratory (MSL), shown in Figure 2.7, more commonly known as Curiosity, is the next step of NASA's Mars Exploration Program and scheduled for launch at the end of 2011. With the size and weight of a medium size car (3.0 x 2.7 x 2.1 m; 900 kg) and currently being built at the Jet Propulsion Laboratory in California, the focus for this mission is to study Mars' habitability [12].

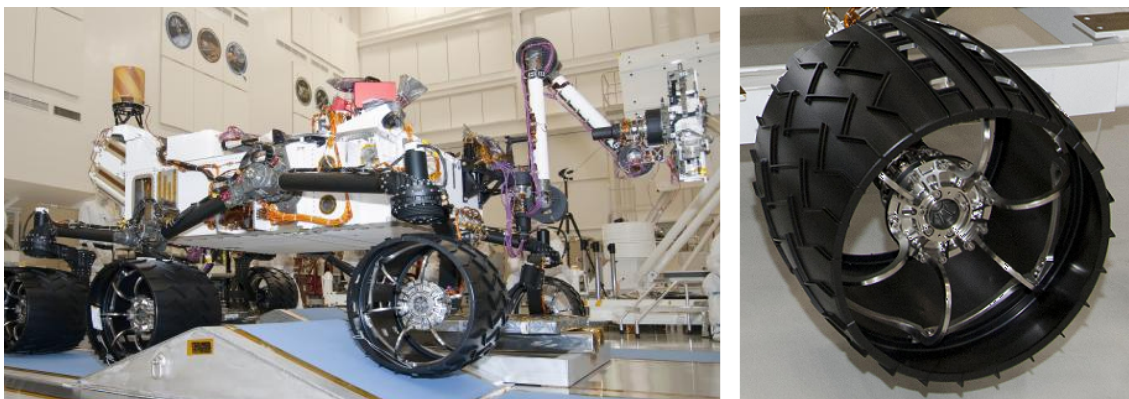


Figure 2.7: Left: Curiosity passes an agility test by successfully navigating a set of ramps. Right: MSL wheel. (Courtesy NASA/JPL-Caltech)

The tubed suspension arms, forming again a rocker-bogie chassis, are made of titanium while the tyres themselves are manufactured out of aluminum. The shell of the tyres is a piece of machined aluminum equal to the thickness of 7 pieces of paper, making them soft and springy, and giving them an equivalent behaviour to rubber tyres [13]. The wheels have a diameter of 510 mm and a width of 300 mm featuring shallow grousers and

visual odometry markers (holes in the tyre) leaving a specific pattern in the wheel track, which can be captured by a camera making it possible to measure the driving distance and to compare it with the distance measured by the driving motors. This is planned as a precaution in order to "foresee" situations where the rover might get stuck in loose sand [13].

2.2.7 ExoMars

The European Space Agency has demonstrated with great success its ability to develop and operate complex space missions. As such, hopes are high for ExoMars, the first flagship mission of the European Aurora Exploration Program, with the first phase planned for launch in 2016 (orbiter and lander). It has the primary objective to search for signs of past and present life on Mars.

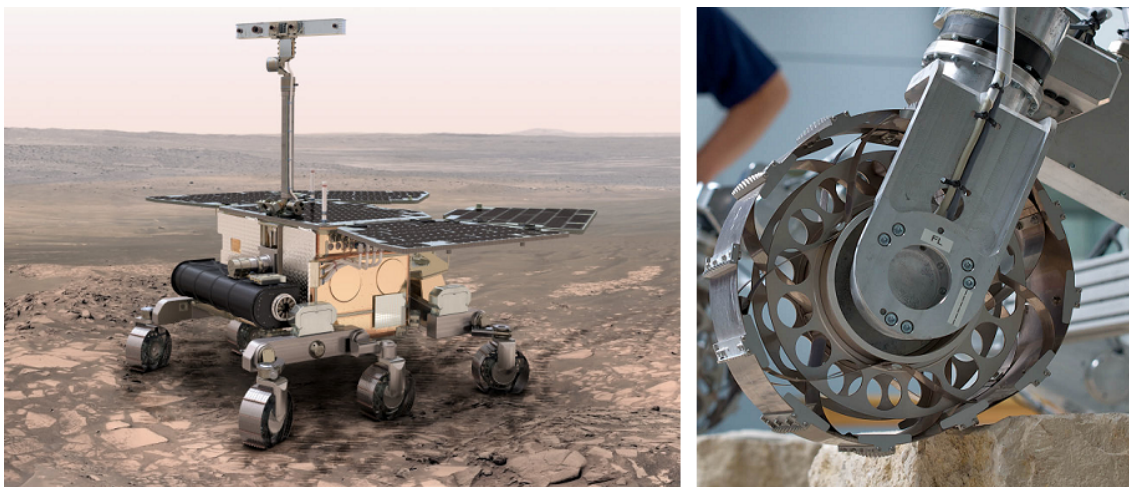


Figure 2.8: Left: ExoMars rover Phase B2 concept. (Credit: ESA) Right: Test of ExoMars Rover locomotion system by RUAG Space in Zürich. (Credit: RUAG)

The second phase of ExoMars, planned for launch in 2018, incorporates the ExoMars rover (Figure 2.8), which draws upon the experience of the American Mars rovers, but represents capabilities not previously flown on any other Mars mission, e.g. sub-surface sampling (drilling) to characterize the water and geochemical environment [14]. The rover, with a footprint of approximately 1.6 x 1.2 m [15], will also have a 6-wheel drive and a "double" rocker-bogie suspension system. The total system mass is currently downsized to approximately 200 kg (previously 300 kg). The unique feature of the locomotion system is an all-metal flexible wheel, which deforms under the rovers mass and due to differing soil conditions (hard rock or loose sand). This, in turn, will dramatically increase the rovers motion performance (see Section 2.3). The wheels have a diameter of 250 mm and a width of 100 mm with the rigid aluminum hub connected via three parallel rows of flexible steel bands, allowing the also flexible rim to deflect like a pneumatic tyre. Grousers, manufactured out of titanium, on the running surface and fins on the side improving climbing ability and skid stability. Two bump stop discs in the centre of the wheel, similar to the one in the LRV wheel, will protect the flexible elements from over-deflection [16].

This flexible wheel design, explained in more detail in the following section, represents the underlying baseline of the concept and design ideas mentioned in later chapters.

2.3 Wheel-Soil Interaction

2.3.1 Soil Mechanics

The principles of soil mechanics are based on the models first proposed in 1956 by M. G. Bekker [1]. He was concerned with developing mathematical models to describe the motion of rolling vehicles interacting with the driving surface and to define parameters to specifically classify soil properties. In his research, he characterized soil behaviour by a set of 6 parameters listed in Table 2.2.

Table 2.2: Set of soil parameter identified by Bekker

Parameter	Property
c	Soil cohesion
ϕ	Internal friction angle
k_ϕ	Frictional soil modulus
k_c	Cohesive soil modulus
n	Soil deformation exponent
κ	Soil shear deformation modulus

With these parameters it is possible to calculate and therefore predict the performance of different rolling systems. The behaviour of the soil to the vertical load is given by n , k_ϕ and k_c , whereas the reaction due to horizontal shear stress is given by c , ϕ and κ . Thus, when all the values are known the ability of a soil to support a vehicles weight and to develop tractive effort can be defined. From the Mohr-Coulomb relation, we can describe the correlation between normal stress σ and shear strength τ as

$$\tau = c + \sigma \tan \phi \quad (2.1)$$

where c is again the soil cohesion, which is the soils component of shear strength that is independent of inter-particle friction ϕ . It can be caused by electrostatic forces, cementing or root cohesion. Through the Bernstein-Bekker equation

$$H_{max} = Ac + W \tan \phi \quad (2.2)$$

the maximal tractive force H_{max} can then be calculated. Where A is the contact area of the wheel on the ground and W is the load onto the wheel. The propelling force, also called the Drawbar Pull DP of a powered system, which is effectively transfered to the ground, is given by the difference of driving force H and the sum of the driving resistance R [17], depending on soil properties and more specifically on the type of wheel used .

$$DP = H - \sum R \quad (2.3)$$

As explained previously, the energy consumption of the rover is a vital factor, as this determines the range a mobile system can travel before recharging. The energy efficiency is also a measure for the dimension of the systems batteries. The more efficient, the smaller the batteries for an equivalent journey and the more room is available for the scientific payload.

The drawbar pull is a good measure by which to determine the capability of a specific system to move over the ground, but to measure the systems efficiency the driving torque T must be taken into account, which defines the force used under a specific momentary condition. The overall efficiency of the drives η is then defined by the shaft power P_{out} over the electric power into the motor P_{in} . This can be rewritten in terms of the wheel parameters drawbar pull and driving torque as

$$\eta = \frac{DP}{T} \quad (2.4)$$

2.3.2 Rigid vs Flexible Wheels

Rigid wheels have been in use since the very concept of the wheel came into existence. Before dedicated roads were available, they were also used on unprepared ground (e.g. horse-drawn carriages moving along loose country roads). At the end of the 19th century, wheel design began to be influenced by the idea of ride comfort, which was judged important from the passengers point of view. Today, the pneumatic tyre is used for road vehicles as well as for off-road vehicles, as these allow for compensation of rough surfaces and reduce shock loads when running against obstacles. As can be seen in Figure 2.9, flexible wheels deform due to the load, leading to an increased contact area and are sinking less into the ground.

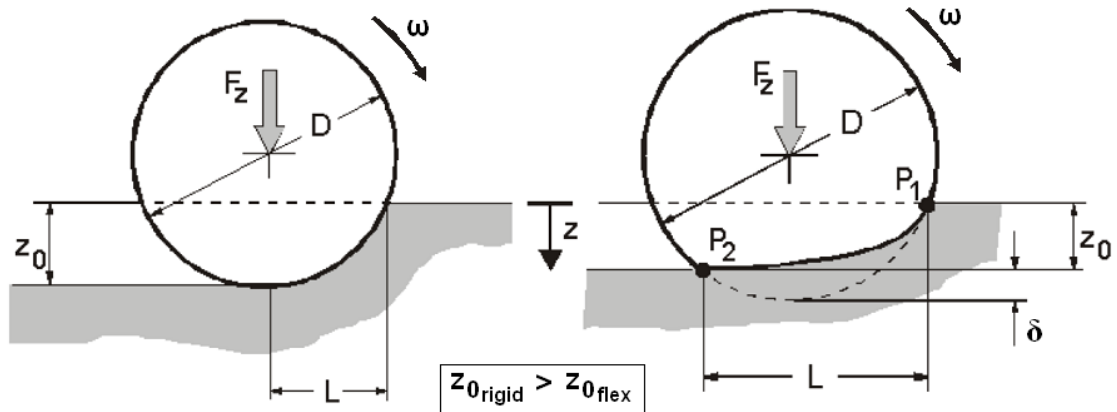


Figure 2.9: Left: Schematic view of the contact contour between rigid wheel and soft soil. Right: Schematic view of the contact contour of an elastic wheel operating on a soft soil surface [18]

To build on the foundations established by Bekker, a great number of investigations attempted to describe the motion of flexible wheels on hard and soft soil conditions. Specifically the work done by J. Y. Wong in 1978 must be mentioned, where he specified the behaviour of pneumatic tyres in terms of the filled air pressure, which can be varied and therefore lead to different deformations under loading. This varying parameter in fact, can be compared to the stiffness of a mechanical spring, where the characteristic spring constant c depends on the material properties. Hooke's law of elastic deformation gives then the amount of deformation of an elastic body by the load W over the resulting deflection δ .

$$c = \frac{W}{\delta} \quad (2.5)$$

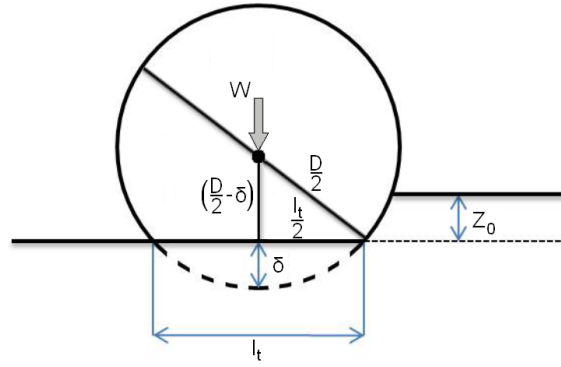


Figure 2.10: Simplified schematic of a flexible wheel pressing on soft soil. The deflection of the wheel is given by the spring equation (Hooke's law). The ground patch can be calculated by the resulting trigonometric function for the side length l_t and the wheel width b leading to the equivalent stiffness of a flexible wheel (Equations 2.6 to 2.9)

The contact or ground pressure p_{gr} of the wheel pressing on the ground is defined by the load over a certain area, which can be stated as

$$p_{gr} = \frac{W}{A} \quad (2.6)$$

where A is the rectangular contact patch of the wheel with the width b and side length l_t .

$$A = b \cdot l_t \quad (2.7)$$

This side length can be derived through trigonometric relations as seen in Figure 2.10.

$$l_t = 2 \sqrt{\delta (D - \delta)} \quad (2.8)$$

where δ is again the deflection derived from Equation 2.5. Substituting this into the above equation for the ground pressure yields an expression in terms of a given wheel load W , its diameter D , width b and its relative compression rate c . This relation is then called the "equivalent stiffness" of a flexible wheel [4], whereas a rigid wheel (infinite c) would lead to maximal ground pressure.

$$p_{gr} = \frac{W}{b \cdot 2 \cdot \sqrt{\frac{W}{c} \left(D - \frac{W}{c} \right)}} \quad (2.9)$$

In other words, an increased contact patch lowers the ground pressure, which in turn causes the wheel to sink less into the loose soil. Figuratively speaking, by deflating the systems wheels the rover will float atop a patch of loose soil.

Wong additionally listed in [17] the requirements that pneumatic wheels have to meet nowadays, which can be used as a baseline for developing new flexible wheel designs. These include:

- Supporting the weight of the vehicle
- Cushioning the vehicle over surface irregularities
- Providing sufficient traction for driving and braking
- Providing adequate steering control and directional stability

Recalling Equation 2.3, one can see that the need to increase the tractive force and to reduce motion resistance is of great concern, as this determines the efficiency of a wheeled system. Friction is necessary to transfer the torque to the ground. If zero or insufficient friction is present, the wheel will slip and the applied torque will not be sufficient to propel the vehicle forward. Slippage S is measured in percentage of the rotating speed of the wheel in relation to the speed of the wheels axle moving along the direction of motion (Equation 2.10) [19],

$$S = \frac{\omega \cdot r - v}{v} \quad (2.10)$$

where ω is the rotational speed of the wheel, r is the wheels radius and v is the vehicles speed over ground. To reduce slip and to improve traction of a powered wheel so called "grousers" can be added around the wheel tread, which dig into the ground and give a certain amount of grip (Figure 2.11). This in particular, is very important when driving on hard surfaces or climbing over rocks.

On the other hand, to reduce the motion resistance acting while driving, one has to separate first the different effects producing this opposing force. According to Bekker [1] and Wong [17], the total resistance of an actuated wheel is the sum of four contributions.

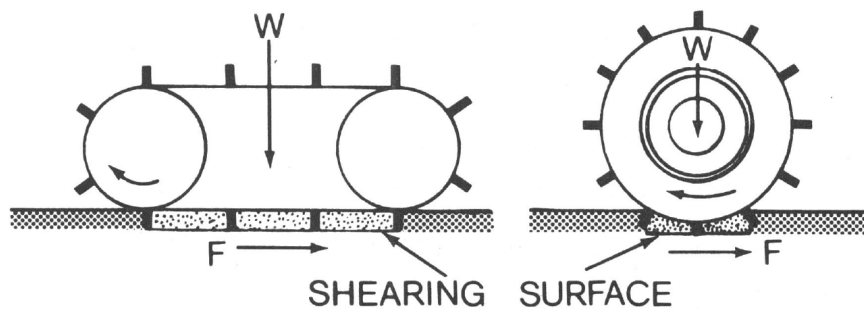


Figure 2.11: Schematic view of a wheel with grousers digging into the ground giving some additional traction. (Reproduced from [17])

- The bulldozing resistance R_b resulting from displacement of the soil in front of the wheel.
- The compaction resistance R_c resulting from compaction of the soil under the wheel.
- The hysteresis resistance R_h due to the deflection of the wheel.
- The gravity resistance R_g resulting from the the downslope force when driving on sloped terrain.

From Equation 2.3 then follows for the drawbar pull

$$DP = (H_{max} + H_g) - (R_c + R_b + R_g + R_h) \quad (2.11)$$

where H_g is the additional tractive force gained by the grousers. The contributions of the resistance to motion are usually empirically measured in experiments, but they can also to some extent be predicted via mathematical models. The Tractive Prediction Model (TPM) is an in-house development by the DLR Institute of Space Systems in Bremen, where the classical Bekker theory has been extended using the basic principles stated above as well as the analytical models of the resisting forces from [17] to calculate applicable parameters such as torque, drawbar pull, sinkage etc. for planetary roving vehicles [20].

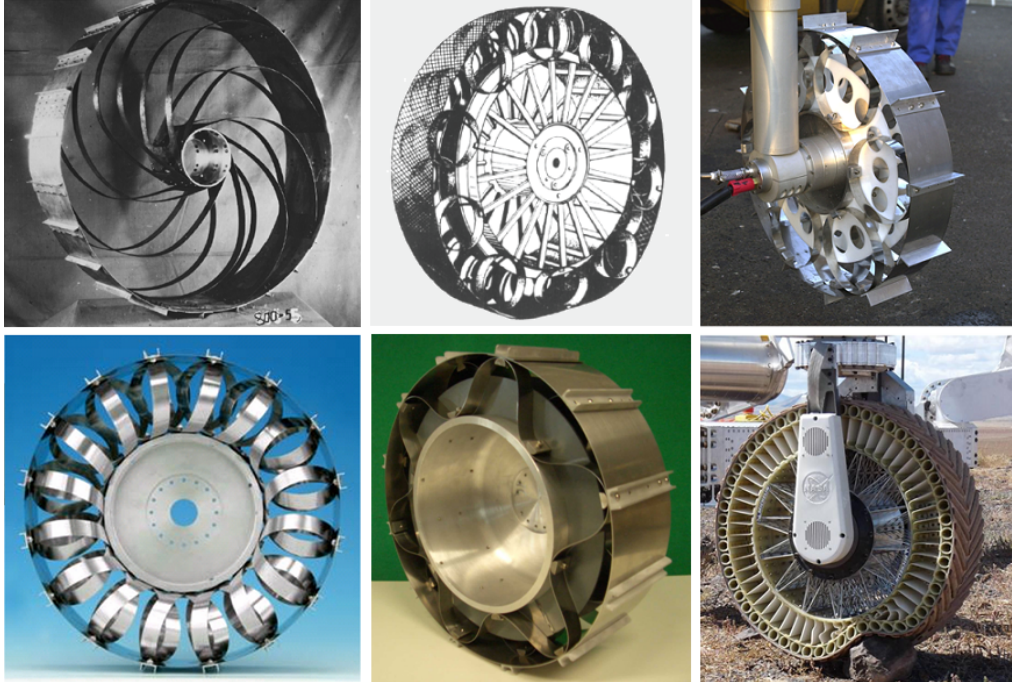


Figure 2.12: Top left to bottom right: Russian spiral spring concept by Markow 1963 [5]. Hoop spring concept by Bendix 1965 as an alternative for NASA's LRV [21]. Cylindrical spring concept by DLR 2002 for the ocean floor vehicle "MOVE!" of the University of Bremen/MARUM [4]. Toroidal coil spring concept by DLR 2006 [4]. Waved spring concept by DLR 2006 for the ExoMars chassis demonstrator "Bridget" [4]. Shear beam concept by Michelin 2008 as a proposal for the next lunar wheel [22].

Although currently designed NASA Mars rovers (refer to Section 2.2.6) do not have flexible tyres, more advanced designs try to take into account the advantages offered by elastically designed wheels. A collection of such designs is shown in Figure 2.12, with each concept having its own characteristic, depending on the materials used and more importantly on the structure and composition of the flexible spokes.

Interesting to note is the flexible wheel design by Michelin (Figure 2.12 bottom right) first introduced in 2005 [22], comprising of composite materials where a "shear beam" is sandwiched between two inextensible membranes. This concept takes advantage of the "top loader" design, where the most prominent example is the tensioned spoke or bicycle wheel. As this information will be of interest in a later chapter of this thesis, it will be explained briefly in the following paragraph.

Rigid wheels, in this context called bottom loaders, support their loading by direct compression from the contact area to the wheel hub. Here, only a small part of the structure beneath the hub carries the load, leading to an overall poor efficiency in terms of load capacity per unit mass. The tensioned spoke wheel, however, reduces the spoke tension locally by a small deformation of the rim due to the contact pressure. In doing so, the load is distributed almost equally along the arc of the wheel above the hub. The whole structure now carries the entire load and as such increases greatly the load capacity per unit mass of the wheel. A pneumatic tyre is also a top loader, as it mimics the load-carrying mechanism of the tensioned spoke wheel by the inflation pressure of the carcass cords. The gain in load capacity per unit mass is similar to the tensioned spoke wheel, but in addition it allows for greater deflections. The top and bottom loader concepts are depicted in Figure 2.13.

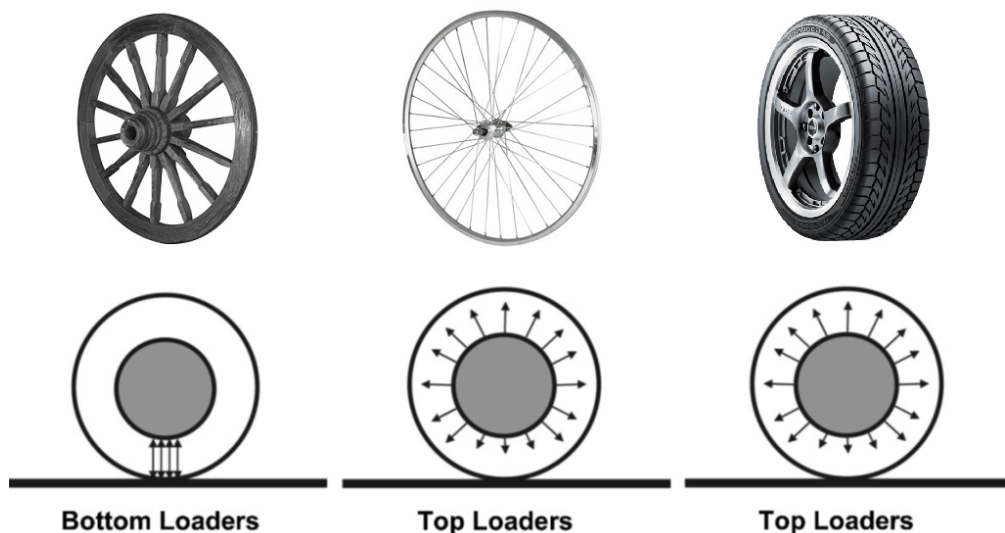


Figure 2.13: Fundamental load-carrying mechanics of wheels. Rigid wheels carry load by direct compression in the contact area (bottom loaders). Tensioned spoke wheels and pneumatic tyres suspend the load from the arch of the wheel above the contact area due to reduction of spoke tension in the contact area (top loaders) [22].

2.3.3 Hard and Soft Soil Conditions

As ground conditions change, the performance of a rigid or flexible wheel changes also. On hard surfaces such as roads, the rolling resistance generally decreases with increasing inflation pressure. This, in turn, reduces the contact patch and therefore the adherence to the ground, which can be of concern on wet and slippery roads. Additionally, with increasing tyre pressure (stiffness) the ability to absorb shocks due to rocks or bumps is reduced. Recalling the statements in the preceding section, on deformable surfaces such as loose soil, a rigid wheel has a higher ground pressure and subsequently a higher sinking rate (higher soil compaction resistance). To counteract this effect, one can either increase the diameter of the wheel or reduce its stiffness making it more flexible (Equation 2.9). The hysteresis or deformation resistance is higher for a soft wheel than it is for a rigid design. As these two resistances have an opposing behaviour, there exists an optimum stiffness for a flexible wheel rolling along a soil surface. The dependency of total motion resistance in terms of stiffness and type of driving surface is shown in Figure 2.14.

All planetary robotic rover missions so far have incorporated a rigid wheel design. The most successful, as widely acknowledged, is the NASA MER mission. Not only did both rovers accomplish their scientific objectives (finding unequivocal mineralogical evidence for the past action of liquid water of the Martian surface) but the rovers far outlived their projected lifetimes (refer to Section 2.2.5). Because Spirit and Opportunity were so successful, receiving also great support from the public, it was a shock when first Opportunity and sometime later, Spirit became stuck in loose sand beds. Intensive Earth-based physical simulations could help to disengage Opportunity, but were unsuccessful in freeing Spirit, which is now, with several of its wheels buried in the sand, permanently immobilized [10].

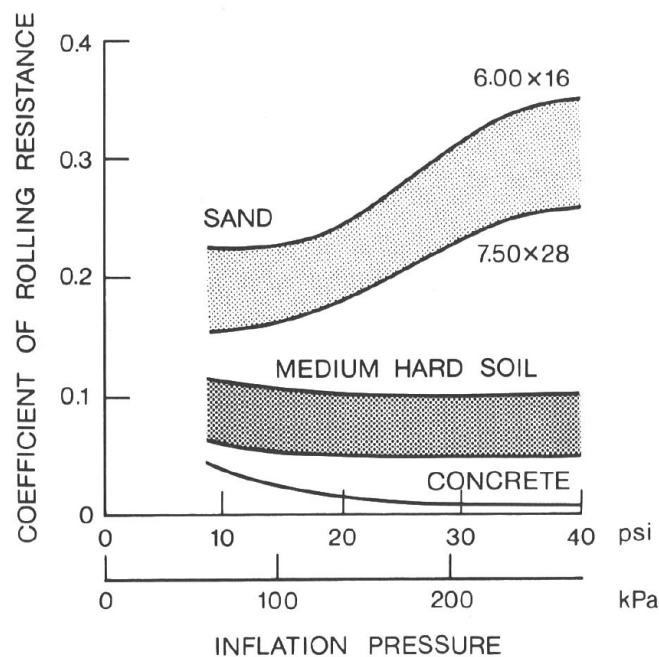


Figure 2.14: Variation of total rolling resistance with inflation pressure for pneumatic tyres on various surfaces. (Reproduced from [17]).

Studies at DLR have concluded, that a flexible wheel design would have performed better in the soft soil conditions encountered by the MER rovers. Equation 2.9 shows the effect of the ground pressure, which leads a flexible wheel on soft soils to achieve:

- An increase in transferable force between the wheel and the ground
- A strong decrease of the bulldozing and compaction resistance
- An increase in hysteresis resistance

On firm ground, however, this is an entirely different matter. Here, the sinking of the wheel is relatively small regardless of whether the wheel is of rigid or flexible design. In this case, the advantage of a deformable wheel to reduce the bulldozing and compaction resistance comes less into play, whereas the hysteresis resistance is still in effect and increases even further. Therefore, the deformation leads on hard soils to:

- An increase in transferable force between wheel and ground
- A relative small decrease of the bulldozing and compaction resistance
- A large increase in hysteresis resistance

In summary it can be said, that flexible wheels have great benefits for certain situations, but need to be carefully evaluated as the deflection heavily affects driving ability and efficiency. Taking into account the formulations above, Figure 2.15 shows an example of the interaction of the different resisting forces acting on a flexible wheel when driving over soft soil. Here can be seen, that for a given soil type there is an optimum (lowest resistance) for the motion performance of a flexible wheel.

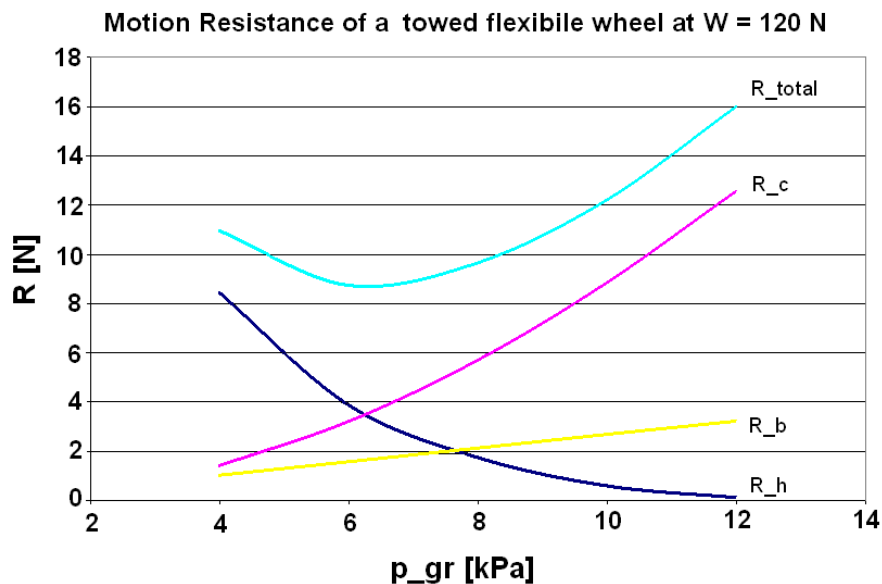


Figure 2.15: Interaction of the different resisting forces acting on a flexible wheel when driving over soft soil. It can be seen, that for a given soil type there is an optimum (lowest resistance) for the motion performance of a flexible wheel. The curves represent the soil compaction resistance R_c , soil bulldozing resistance R_b , tyre hysteresis resistance R_h and their sum R_{total} (total motion resistance) for a towed flexible wheel of 300 mm diameter and 150 mm width at a wheel load of 120 N on a medium soft soil type as a function of equivalent wheel stiffness. (Reproduced with permission from [4])

2.3.4 Adaptive Wheel Design

The RIMRES project goes even further than just looking into the concept of a deformable wheel. Unknown terrains, as will be encountered in unexplored areas of the Moon or Mars, have the undeniable effect of being variable and unpredictable. As discussed above, wheel performance changes significantly between hard and soft ground. To combine the positive behaviour of both concepts, DLR is planning to develop a hybrid wheel capable of adapting its state to the momentary soil situation. Here, a sensor system will collect characteristic soil parameters, on which basis the on-board computer can then select the best deformation state and initialise the necessary stiffness adjustment. This procedure would be equivalent to the inflating or deflating of a car's pneumatic tyre in order to increase fuel efficiency.

The advantage of such an adaptive design becomes even more evident when the rover is reconfigurable, as is planned for the RIMRES rover, where the systems mass changes with the mode of operation. As is shown in Figure 2.16, the rolling rover is able to carry a legged scout vehicle and additional payload packages, which when combined account for approximately a quarter of the total rover mass (see Section 3.2). Recalling once more Equation 2.9, a higher system mass implies a higher ground pressure. If, however, the flexibility of the wheels could be adjusted, it would be possible to balance the higher system mass and to achieve the same ground pressure as for lower system masses. Hence, better overall motion efficiency.

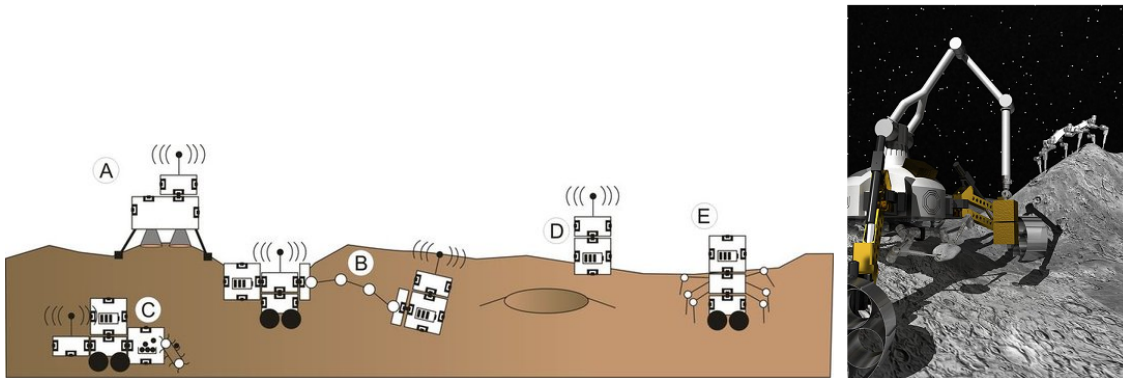


Figure 2.16: Left: Illustration of the envisioned RIMRES system. A: Landing unit with radio module; B: Rover with radio module and additional battery package deploys radio beacon; C: Rover with additional battery and radio module makes use of a sampling module; D: Operating radio module stack; E: Connected rover and scout on their way to a crater for exploration (Reproduced with permission from [23]). Right: RIMRES scenario in an artist impression. The rover in the foreground is about to set out a stack of two modules. The connected scout beneath the rover analyses a small rock sample. In the background, a second scout climbs a slope to steep for the wheeled system (Credit: DFKI).

2.4 Summary

The principle and necessity of flexible wheels used for off-road vehicles has been studied. In particular the difference between the wheel soil interactions for hard and soft ground conditions have shown that a carefully designed wheel concept for a given or expected ground condition can achieve great advantages in terms of energy efficiency and the ability to cope with rough and difficult terrains. The focus here was on previous developments as well as current design approaches of systems for planetary surface operations beyond the Earth.

The advantages of a rolling mobility system over other locomotion principles has been presented. Specifically the current wheel design for the ESA ExoMars rover featuring an all-metal flexible wheel and the Michelin lunar wheel utilising a shear beam concept based on the load carrying principle of the bicycle wheel were outlined. Both designs deform under the influence of the system mass as well as differing soil conditions.

In addition, the expected improvements in motion performance of an adaptable system able to adjust its state to current conditions has been stated. This, in particular, is the baseline for the RIMRES project and this thesis. The following chapters provide the concept development, detailed design as well as the mechanical analysis of this new and innovative wheel design.

Part II

SYSTEM DESIGN

3

CONCEPT ASSESSMENT

In this chapter, the previous work at DLR outlining potential concepts to adjust the stiffness for the envisaged RIMRES wheel are assessed (including extending breadboard tests) and critically analysed in terms of the effective stiffness variation, the differences of the wheel characteristic ground contact points, as well as the overall motion performance. This chapter is then concluded giving a recommendation for which concept to pursue to the detailed design phase.

3.1 Baseline Wheel Design

The German Aerospace Centre (DLR) has already conducted intensive research in the field of rover wheel development. To draw upon these experience, the all-metallic flexible wheel, shown in Figure 3.1, developed by DLR for the Bridget chassis rover demonstrator [15] and later adopted by RUAG Space for the ESA ExoMars rover mission shall function as the baseline wheel design. For the RIMRES project, it is planned to advance this type of wheel to an intelligent sensor version able to collect information about the surfaces soil properties. In addition, it shall then be capable of adjusting its flexibility to the present ground condition.

The baseline wheel, which is available as a demonstrator at the DLR Institute of Space Systems (IRS) in Bremen has a diameter of 250 mm and a width of 110 mm. In 2007, L. Richter [24] recommended the cylindrical shape as the wheel of choice for the ExoMars rover. Richter also addresses the choice of the wheels stiffness by analysing the wheels performance through the wheel-soil Tractive Prediction Model (TPM) [4]. According to this model, the stiffness should be selected that for all specified slopes the wheel remains in "flexible mode" such that no bump stop contact occurs on any of the wheels. A rigid behaviour, meaning no deflection at all, was however defined as permissible. The wheels components and their primary function can be summarised as follows.

The flexible outer ring serves as the tread of the wheel and is the contact interface to the ground, whereas the wheel hub is rigid and houses the harmonic gear drive of the rover's leg. The flexible spring elements (two outer and one inner) are made of three parallel bands of waved sheet metal placed around the rotational axis. Each band is fixed

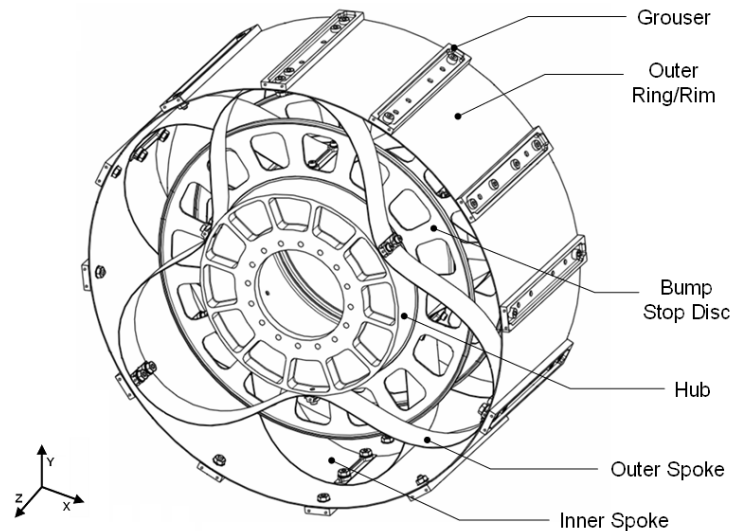


Figure 3.1: Schematics of the Bridget/ExoMars wheel which will be used as the baseline wheel for the new adaptable design. The coordinate system is defined with the origin in its geometrical centre, the x-axis in line with the rovers motion, y-axis radially against the gravity vector and z defines the rotational axis of the wheel. (Credit: DLR)

by six points, three on the hub and three on the outer ring, respectively, spaced equally at 120° intervals along the circumference. The inner band is double the width of an outer band and is rotated by 60° , which leads to a design comparable to a 6-spoked wheel.

Bump Stop Discs (BSD's) are included to enable the wheel to sustain maximum impact load on the flexible outer ring without collapsing. This shall ensure a non-plastic deformation performance of the wheel along all mission phases. The bump stops are placed symmetrically on each side in the gap between the inner and outer flexible elements. The deformable bands are fixed on the hub with rivets which take the shear loads. Intermediary plates are used to obtain a line contact between band and hub as well as between band and outer ring, which was considered to improve the stress distribution.

Grousers are fitted to the wheel to improve traction and hence improve the slope gradeability of the vehicle. Each grouser extends along the entire wheel width. This orientation provides the required tractive effort in the direction of motion due to the shearing of the soil at the leading edge when the grouser comes in contact with the ground during motion (refer to Section 2.3.2). Additional side grousers (not shown in the schematic), also called fins, could be added to reduce side-slippage when driving on a cross-hill slope.

The hub, BSD's, grousers and other fixation elements of the demonstrator wheel were machined from Aluminum. Stainless steel was selected for the flexible bands as well as for the outer ring due to the requirement for high durability. Table 3.1 and 3.2 summarise the main characteristics of the baseline wheel.

Table 3.1: Baseline wheel characteristics

Design Property	Symbol	Value	Unit
Wheel diameter (undeflected)	D	250	mm
Wheel width	b	112	mm
Hub diameter	d_h	120	mm
Hub width	b_h	112	mm
BSD diameter	d_{bs}	190	mm
Designed equivalent stiffness	p_{gr}	11	kPa
Designed wheel load	W	132	N
Wheel overall mass	m_w	1670	g
Outer ring thickness	t_r	0.5	mm
Spoke thickness	t_s	0.3	mm
Outer spoke width	b_{os}	20	mm
Inner spoke width	b_{is}	50	mm
Spoke length	l_s	701.52	mm
Grouser height	h_g	10	mm
Grouser width	b_g	15	mm
Number of grousers	-	12	-
Number of fixation screws	-	16	M3x22

Table 3.2: Baseline wheel materials as specified in [25]

Element	Material	Composition	Euro Norm
Spokes/Bands	Spring stainless steel	X10CrNi18-8	1.4310
Outer ring	Spring stainless steel	X10CrNi18-8	1.4310
Hub	Aluminum	AlSi1MgMn.	EN AW-6082 T6
BSD's	Aluminum	AlSi1MgMn.	EN AW-6082 T6
Grouser	Aluminum	N/S	N/S
Other fixation elements	Aluminum	N/S	N/S

Table 3.3: Estimation of the overall system mass for the RIMRES rover.

Unit	Quantity	Weight (kg)
Scout	1	25
Body	1	30
DLR wheel	4	5
Placing unit (rover leg)	4	27
Module package	5	5
Manipulator	1	25
Total system mass w/o scout	-	208
Total system mass (F_G)	-	233

3.2 RIMRES Requirements

As outlined in Section 2.3, the rover wheels build the contact interface to the ground. Due to this reason, they will be subject to different load cases depending on the rovers operational mode (parking, rolling and climbing). In order to be able to define possible wheel stiffening concepts and selecting a preferred one for the RIMRES rover, the relevant requirements as stated in [26] are reviewed here.

3.2.1 Forces and Moments

Wheel Load

Table 3.3 lists the estimated mass fractions of the different system components, which will be used as a baseline to define the load resting on each wheel. According to this, the total system mass F_G is 233 kg. Although the mission scenario foresees the rover to operate on the surface of the Moon, the current design will be an Earth-based technology demonstrator. With this consideration in mind, we find the equivalent force resting on each wheel by

$$\begin{aligned} W &= \frac{F_G \cdot g}{n_w} [N] \\ &= \frac{233 \text{ kg} \cdot 9.81 \text{ m/s}^2}{4} \\ &= 571.4 \text{ N} \end{aligned} \quad (3.1)$$

where g is the acceleration due to Earth's gravity and n_w is the number of wheels attached to the rover. It shall be noted, that the centre of gravity and therefore the force on each wheel may change when single module packages are taken on or off, when the rover drives on sloped terrain or when driving over obstacles. For the first iteration process, however, the assumption is made that all wheels are loaded equally.

The physical dimensions of the RIMRES wheel were selected to ensure a minimum ground clearance of about 50 mm when the rover is in its lowest possible configuration and with the scout attached (Figure 3.2). The number and sizing of the grousers were taken from the baseline wheel. A summary of the wheel dimension is provided in Table 3.4.

Table 3.4: RIMRES wheel dimension as specified in [26].

Element	Value	Unit
Wheel diameter	400	mm
Wheel width	200	mm
Mounting depth	20	mm
Grouser height	10	mm
Grouser width	15	mm
Number of grousers	12	-

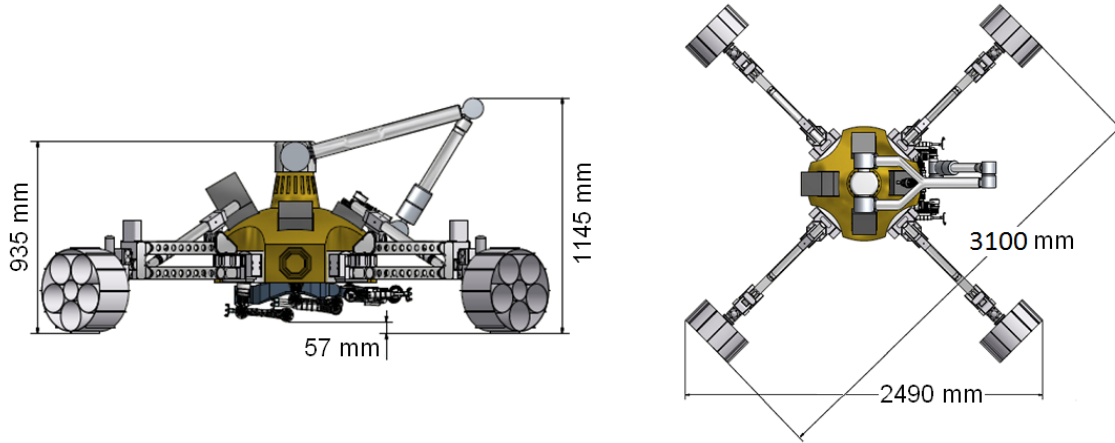


Figure 3.2: RIMRES rover lowest configuration as specified in [26].(Credit: DFKI)

Torque

Each wheel will be actuated by a harmonic drive motor of the type CSG-20-50-2UH (see data sheet in Appendix C), which is of a compact design, featuring high torque capabilities and having a long operating life. The nominal rated torque T_N is given with

$$T_N = 33 \text{ Nm}$$

For the reason that the wheel collides with an obstacle or is jammed (step down manoeuvre) will be part of the rovers operation, which may increase the momentary load on the wheel, for stress analyses we will use the maximum momentary peak torque T_M of the drive unit

$$T_M = 127 \text{ Nm}$$

3.2.2 Wheel Operation Mode

The soil type and terrain conditions the rover will be tested on were proposed by DFKI with a loose sand/rock standard area, a section with soft quartz sand, another one filled with a lunar regolith simulant, lowlands with defined crater slopes and a high plateau with an obstacle course [27]. As it was shown in Section 2.3.3, the soil properties have a significant impact on the deformation of the wheel. The maximum deflection will occur on hard ground as the contact pressure reaches a maximum. For this reason, the wheels deflecting capability will be designed to sustain "maximal nominal deflection" on hard ground loaded with maximum system mass. Furthermore, as mentioned in [4] the wheel shall operate in flexible mode under nominal conditions. The BSD's shall function as fail safe for non-nominal operation only.

This in mind, the following wheel operation modes were developed as part of this thesis (Figure 3.3) in terms of ground characteristic (hard or soft) and wheel deflection (rigid or flexible mode). Thanks to the adjusting capabilities the wheel will behave as a rigid wheel on hard ground and will operate in flexible mode when driving over soft soils. As a fail safe, when the adjustable mechanism will be non-operational, the wheel will be

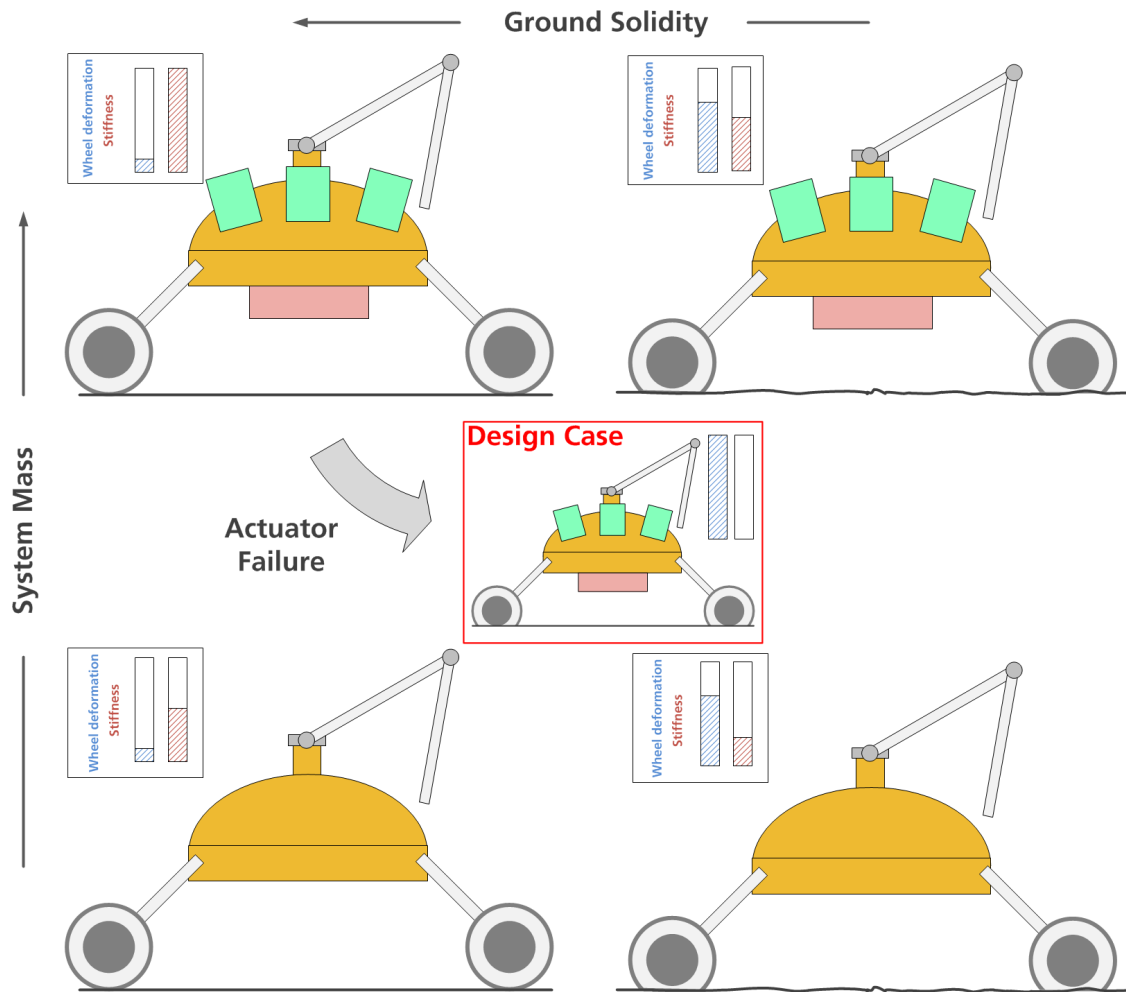


Figure 3.3: Expected RIMRES wheel operation mode. Due to its adjusting capabilities, the wheel will behave as a rigid wheel on hard ground as this will be most efficient with respect to energy consumption. The wheel will, however, operate in flexible mode when driving over soft soils. As a fail safe when the adjustable mechanism will be non-operational, the wheel will be designed to sustain rigid ground scenarios even when loaded with maximal system mass [28].

designed to operate in flexible mode even when driving over solid ground and loaded with maximal system mass. This will be ensured through the design of the basic mechanical stiffness of the wheel elements.

3.3 Assessment of Previous Concepts

The following section reviews the previous outlined concepts to adjust the stiffness of the baseline wheel as they were proposed in [29]. These concepts, named 1, 2 and 3, are then critically analysed and evaluated in terms of their feasibility and performance. In the preceding work, concept 3 was selected as the concept of choice. For this reason, it was the first to be analysed in more detail, followed by concepts 2 and 1. Therefore, the concepts will be described here in reverse order also.

3.3.1 Pulling Strings

Concept 3 (C3) proposes a method to counteract the deformation of the flexible spokes using metal strings or fibres. These strings introduce a tensile force pulling the flexible elements inwards and holding them in place. Figure 3.4 shows the pulling string concept, the red arrows visualise the forces contracting the flexible spokes. The strings are guided through the rim into the inner hub where they are rolled-up onto a coil, which itself is a rotating actuator. This actuator is then used to tighten or loosen the strings, thus increasing or decreasing the inward pulling force on the flexible spokes. It is envisaged to use deflection rollers to guide the strings onto the coil.

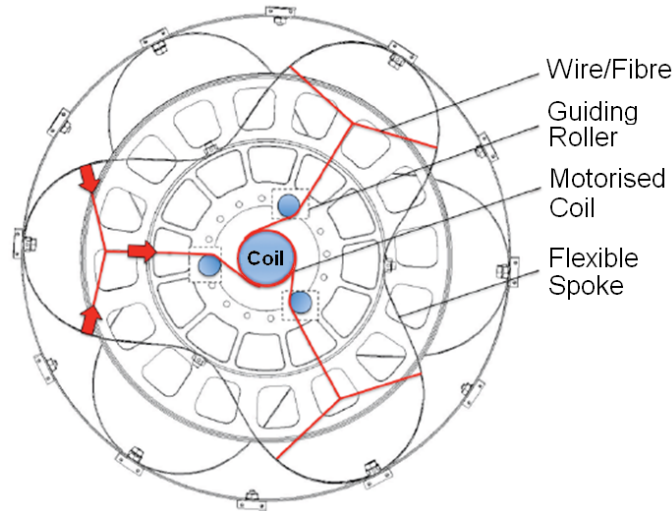


Figure 3.4: Concept 3 - Pulling Strings. To vary the stiffness, the spokes are contracted by a flexible wire coiled-up onto a central coil [29]

Experimental Testing

During the trade-off conducted in [29] this concept was found to be most promising, and as a result was tested experimentally which will be reviewed in the following.

In the breadboard (BB) setup adjustable rod strainers, fixed with a cable tie between the waved spokes, served as the resisting element (Figure 3.5 Left). The stiffness of the spokes and the wheel was then measured using the in-house Bevameter (Bekker Value Meter), which is usually used to analyse the properties of different soil types. Mounted on a vertical rod is a metal plate introducing a defined and equally distributed force on the soil, or in this configuration, the wheel (Figure 3.5 Right). Measured outputs are the applied force and the distance the plate travels along the vertical direction. The specific spring constant is then calculated using Equation 2.5.

Because of the nature of the waved spring elements, the stiffness of the wheel varies along the ground contact points (GCP's). This is due to the fact that the load resting on the wheel deforms predominantly either the inner or outer spokes or the region between them. Thus, the measurements were conducted on the 3 inner and outer spokes and the 6 regions in between respectively. Each measurement, conducted twice to ensure sufficient accuracy, was then averaged to define the mean spring stiffness of each contact point. The average of the GCP's was then used to derive the specific spring constant of the wheel.

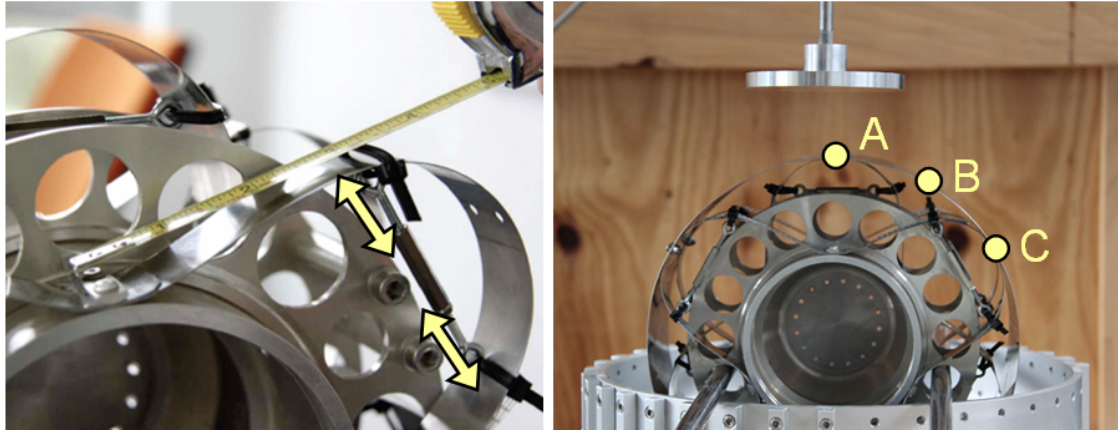


Figure 3.5: Left: Concept 3 BB using rod strainers as the resisting element, which can be varied in length to either contract or expand the spokes. Right: Bevameter setup to measure the wheels stiffness. Note the 3 different ground contact points of the inner spoke (A), inter-spoke region (B) and outer spokes (C).

To acquire different stiffness values the rod strainers were varied in length to either contract or to expand the flexible spokes. The different stiffness states, according to the varied length and the resulting equivalent wheel stiffness (ground pressure) obtained by Equation 2.9, are shown in Table 3.5.

From these results it can be seen, that the alteration length (min to max) of the ground pressure is 7.7 kPa at a nominal wheel load of 150 N. It can also be seen that states 2 and 3 lead to almost the same stiffness values. The inner spokes show no significant changes between states 1 and 2. This was argued in [29] to be a problem caused by the cable ties, which could stretch with increasing load. For this reason and the fact that the foreseen actuator could produce a higher force to contract the spokes, it was estimated that the maximal stiffness value lies above the presented 21.3 kPa.

3.3.2 Concept 3 - Revision

Although the presented results looked very promising, it was doubted that a practical implementation of this concept would be feasible. Concerns about the systems complexity due to the many moving parts, the probable difficult fixation of the strings to the flexible bands as well as the undefined interface through the hub and onto the coil led to the decision to revise this concept as part of this thesis.

Table 3.5: Results of concept 3 BB testing. (Reproduced from [29])

Stiffness state	Spring const. outer spoke [N/mm]	Spring const. inner spoke [N/mm]	Spring const. inter-spoke region [N/mm]	Spring const. wheel [N/mm]	Ground press. at 150 N [kPa]
State 1	55.12	35.46	17.67	36.08	21.3
State 2	48.01	36.48	14.65	33.04	20.4
State 3	49.99	37.74	15.34	34.36	20.8
State 4	35.25	24.06	12.09	23.8	17.4
State 0 (orig.state)	16.34	15.48	11.35	14.39	13.6

Table 3.6: Results of the calibration and new calculation of the equivalent stiffness.

Stiffness state	Spring const. outer spoke [N/mm]	Spring const. inner spoke [N/mm]	Spring const. inter-spoke region [N/mm]	Spring const. wheel [N/mm]	Ground press. at 114 N [kPa]
State 1	47.83	35.18	12.41	18.99	13.6
State 2	62.01	28.78	14.83	21.58	14.5
State 3	53.33	36.21	12.82	19.77	13.8
State 4	29.61	20.08	9.92	14.03	11.7
State 0 (orig.state)	13.78	13.03	9.22	11.64	10.7

Data Calibration and Stiffness Variation

The raw data used to produce the values in Table 3.5 was used directly from the output file of the Bevameter. However, due to a calibration error the data in the output file contains an offset and requires calibration [30]. This can be done using the calibration software developed at DLR. It was also found, that the equivalent stiffness was computed with a load of 150 N, despite the fact that the experiment was run with a load of only 130 N. As a result, the previously acquired raw data was subjected to a new data reduction process.

After calibration, the applied load drops from 130 N to approximately 114 N and as a result the overall stiffness variation decreases to 3.8 kPa (Table 3.6). The table shows also that state 1 has not the highest stiffness value anymore, but state 2. This seems logical, since a contraction leads to a higher stiffness (see explanation below). The equivalent stiffness of the unaltered wheel is also close now to the designed value p_{gr} (refer again to Table 3.1) and only marginally lower since the applied load was lower then the designed wheel load.

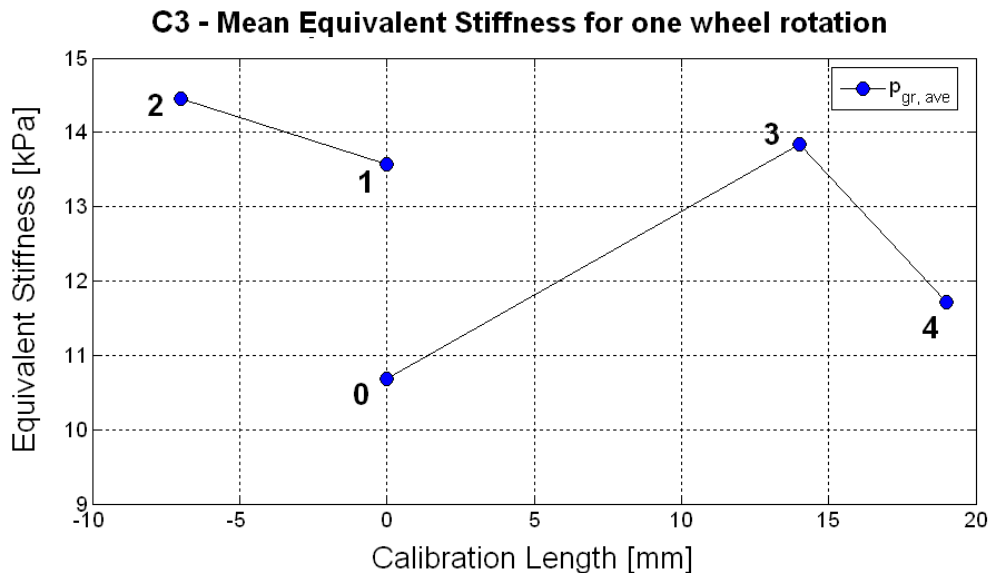


Figure 3.6: Evolution of the equivalent stiffness of Concept 3. From left to right: state 2 (65 mm), state 1 (72 mm), state 0 (no stiffener), state 3 (86 mm) and state 4 (91 mm).

Calibration Length

A stiffness variation of approximately 4 kPa would still be a good measure, but the graph in Figure 3.6 shows the values according to their calibration length. A negative value represents a contraction of the flexible spokes and a positive value corresponds to an expansion with respect to the original state (state 0). At state 1, the spokes are neither expanded nor contracted, but hold tight in their nominal position.

Looking at Figure 3.6, it can be seen that to achieve a proportional increase from most flexible to most stiff, one would have to start with state 0, expand the spoke to state 4, move back to only hold the spokes in place at state 1, expand again to state 3 and finally contract the spokes to state 2. In terms of operation, this is not a desirable behaviour. Furthermore, a clear trend of the stiffness variation is not visible due to the small number of data points.

Though the idea of contracting and expanding the flexible spokes to adjust the stiffness is clear, the concept with a flexible string does not allow to push the spokes outward. Hence, the overall stiffness variation of this concept drops to only 1 kPa (state 1 to state 2). This excludes the jump from state 0 to state 1, which is likewise impractical as it would not be feasible to remove the resisting wire during operation.

Difference between Ground Contact Points

As mentioned previously, the three ground contact points (GCP's) have different stiffness values. In [25] it was pointed out, that an "averaged" wheel stiffness is not applicable in operation since either predominantly a spoke or an inter-spoke region will contact the terrain. In order to have a similar deflection for all GCP's these differences should be kept as small as possible. The two graphs in Figure 3.7 and 3.8 show the evolution of the stiffness difference and the progress of the deflection, respectively. The load of 114 N is again the calibrated value from the set value of 130 N at the Bevameter.

It is visible that this method dramatically increases the stiffness difference of the GCP's (factor of 10). This would lead in a worst case that the wheel deforms only a little when resting on an inner or outer spoke, while undergoing large deflection close to the BSD when the inter-spoke region makes contact with the ground. The net effect would be a bouncing motion of the wheel during operation.

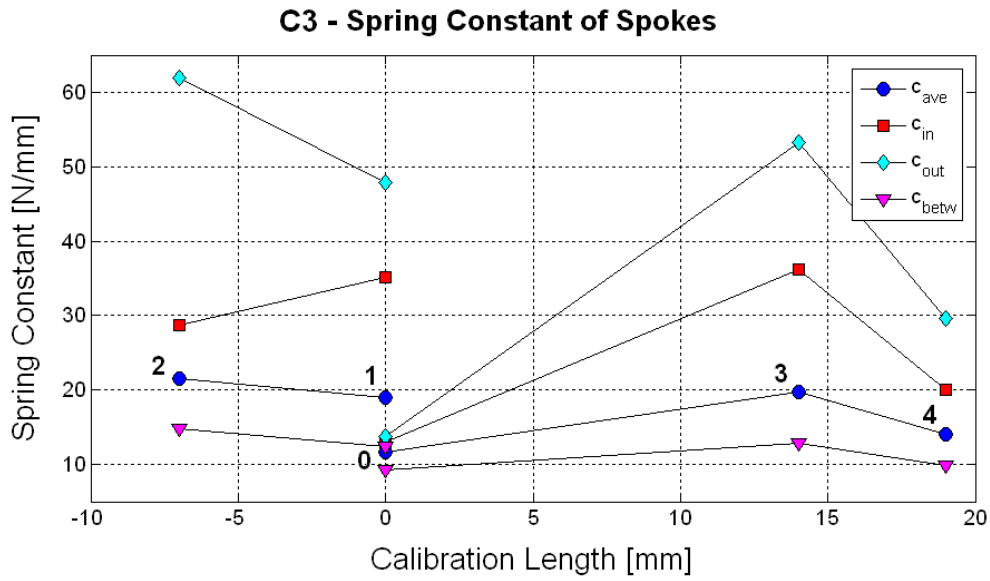


Figure 3.7: Concept 3 - Progress of the stiffness variation of the inner spokes (\square -) outer spokes (\diamond -) as well as the inter-spoke region (∇ -). The (\circ -) line represents the average over one full wheel turn.

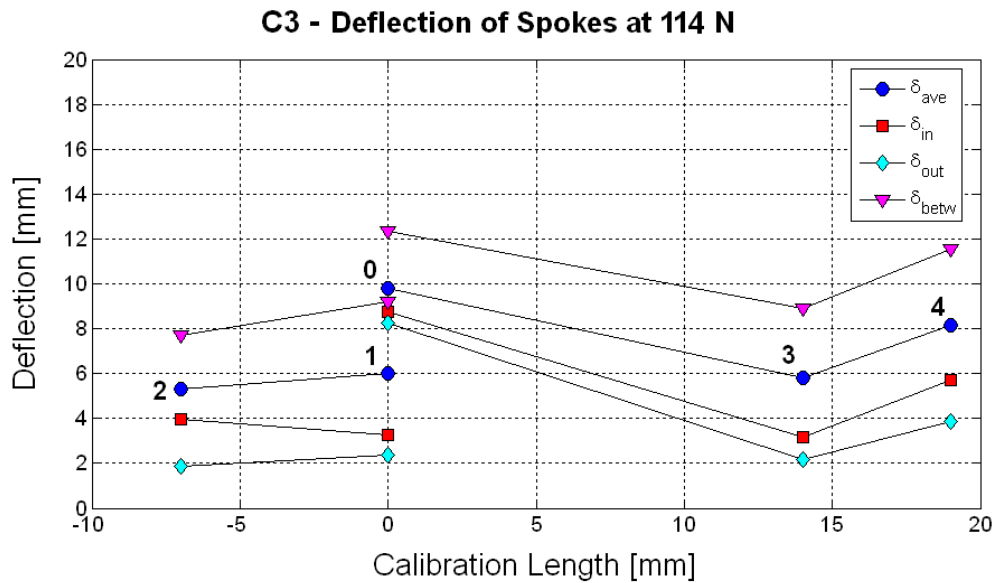


Figure 3.8: Concept 3 - Progress of the deformation variation of the inner spokes (\square -) outer spokes (\diamond -) as well as the inter-spoke region (∇ -). The (\circ -) line represents the average over one full wheel turn.

Implication on Bump Stop Functionality

As previously mentioned, the calculation of the equivalent stiffness was originally done using a value of 150 N. After clarifying the boundary conditions to the performed test, it was identified that the first measurements with the rod strainer were indeed performed with a load of 150 N. This was reduced, however, due to the fact that while testing the fixation could not hold leading to the rupture of a cable tie.

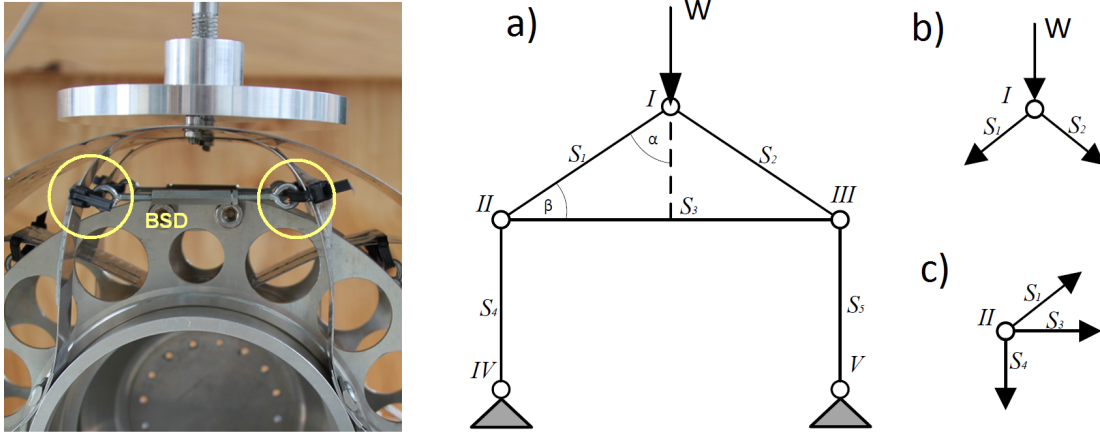


Figure 3.9: Problem of increased tensile forces at fixation points when resisting elements between the spokes are used. In a first approximation, the spoke is simplified as a truss structure (a). The forces in the members lead to the combined forces applied at each node (b and c).

Owing to the fact that the rod strainer prevents the spoke from deforming outward, the force distribution can be approximated using a static approach. Here the spoke is simplified as a truss, with the curved band replaced by rods connected via nodes (Figure 3.9).

$$I \quad \swarrow : S_1 + W \cdot \cos \alpha = 0 \quad (3.2)$$

$$\searrow : S_2 + W \cdot \cos \alpha = 0 \quad (3.3)$$

$$\Rightarrow S_1 = S_2 = -W \cdot \cos \alpha$$

$$II \quad \downarrow : S_4 - S_1 \cdot \sin \beta = 0 \quad (3.4)$$

$$\rightarrow : S_3 + S_1 \cdot \cos \beta = 0 \quad (3.5)$$

$$\Rightarrow S_4 = S_1 \cdot \sin \beta$$

$$\Rightarrow S_3 = -S_1 \cdot \cos \beta$$

Equations 3.2 and 3.3 show the forces of the members at node I, whilst the forces of the members at node II are given in Equation 3.4 and 3.5. Assuming the force $W = 150 \text{ N}$ and estimating the angle $\alpha = 55^\circ$ and $\beta = 35^\circ$ then the horizontal components of members S_1 and S_3 will tear at the node II with a combined force of

$$F_{II} = S_1 \cdot \cos \beta + S_3 \quad (3.6)$$

$$= 70 \text{ N} + 70 \text{ N}$$

$$= 140 \text{ N}$$

An applied force of $W = 130\text{ N}$ would result only in a combined force of $F_{II} \approx 110\text{ N}$. Investigating the tensile strength of the used cable tie confirmed that rupture occurs above 30 lb (135 N), see Appendix C. The truss model is of course only a rough estimate of the local force development at the fixation point. If one assumes the curved band behaves like a straight rod and neglecting element masses as well as notch effects at the fixation, then the value of the angles α and β define the total force at node II. Changing these values can lead easily to higher forces. But it becomes clear, that the used approach, with the cable tie fixation, can fail when the setup is applied to 150 N while withstanding a load of 130 N.

The cable tie rupture has in fact revealed a major problem with implication on the wheels fail safe mechanism. Though the introduced tensile force of the rod strainers is not critical in terms of deforming the spokes permanently while testing, this still increases locally the stress on the spokes. Having an increased stress level at points, which lie well above the bump stop, can have a dramatic effect in operation. If for example the wheel were to be subjected to shocks, when contacting hard surfaces, the yield strength of the spokes could be reached without the possibility of making contact with the BSD. In other words, the bump stop would lose its fail safe function.

3.3.3 Linear Moving Pins

Concept 2 (C2) uses linear moving pins to push the contact points on the hub outwards and so manipulating the shape of the flexible spokes (Figure 3.10). The red arrows show the position where the force is introduced and the green bars symbolise the moving pins. Deforming the spokes increases the internal stresses and the effective deflection becomes smaller. This results in a higher stiffness of the wheel [29].

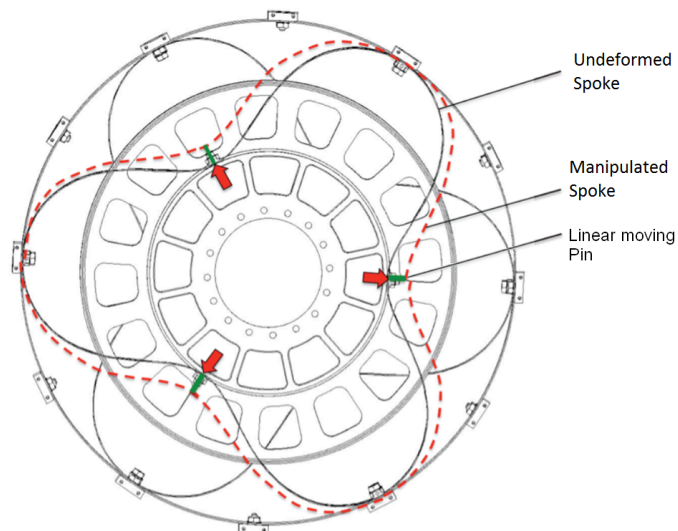


Figure 3.10: Concept 2 - Linear Moving Pins. To vary the stiffness, the contact points on the hub are pushed outward in order to manipulate the shape of the spokes [29]

During the previous trade-off study it was argued that the higher number of motors/actuators in this concept would lead to higher energy consumption and a higher mass fraction when directly compared to C3. Due to this assumption, it was not investigated further. However, an experimental analysis, similar to that carried out for C3, was encouraged to confirm the theory behind the C2 design. This proposed analysis was conducted as part of this thesis and will be outlined in the following section.

Experimental Testing

In order to move the contact points on the hub outwards, the baseline wheel was modified so that it could accommodate long screws. These separators were then fixed both at the side of the spokes and the side of the hub (Figure 3.11). This was done to ensure that the bands were held tight in the desired position.

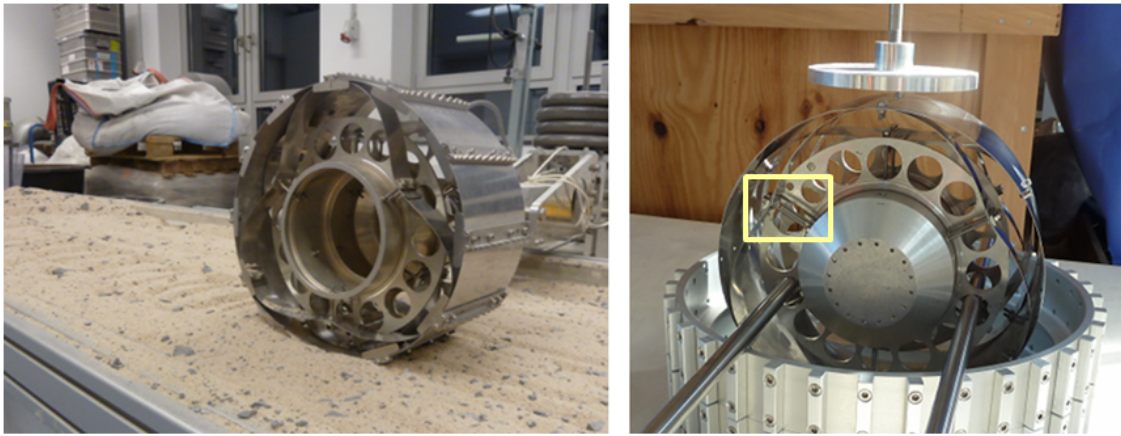


Figure 3.11: Concept 2 - Baseline wheel modification. Left: Test on the Single Wheel Testbed. Right: Bevameter BB setup to measure the equivalent stiffness and to determine the behaviour of the C2 stiffening concept. Note the modification of the baseline wheel with long separators, in order to vary the distance between the hub and the flexible elements.

The test procedure as well as the calculation process of the equivalent stiffness of C2 was the same as for C3 (refer to Section 3.3.1). The Bevameter is used again to measure the force applied to the wheel and to measure the distance of the deformed outer ring (Figure 3.11 right)

3.3.4 Concept 2 - Revision

Stiffness Variation and Alteration Rate

The calibration length of the separators is from 0 mm (original state) to 40 mm (maximum distance reaching the height of the BSD's). During testing, a maximum distance of 35 mm could be achieved due to limiting length of the screws/threaded bar and the locking nut. The data set displayed in Figure 3.12 shows an overall decrease in the equivalent stiffness (point 0 to point 3), which is the opposite effect from the previous assumption. The variation of the stiffness, is with approximately 1.5 kPa relatively small. The curve, after reaching a minimum, makes a turn and the stiffness increases again (point 3 to point 5). The reason for this behaviour is explained hereafter.

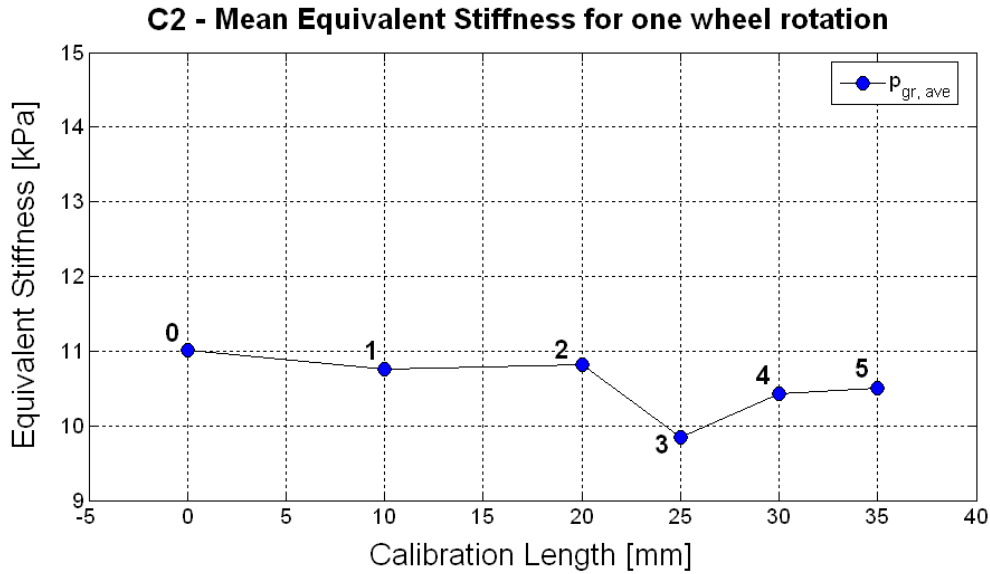


Figure 3.12: Evolution of the equivalent stiffness of Concept 2 tested with the Bevameter

To explain the effect of the decreasing stiffness, we can utilise the bending theory of beams (Figure 3.13). The maximum deflection of a simply supported beam is given by

$$w_{max} = \frac{F \cdot L^3}{EI \cdot 48} \quad (3.7)$$

where E is the modulus of elasticity of the material and I the moment of inertia of the beams cross section. As can be seen from this formula and Figure 3.13, the further apart we place the supports the longer L becomes and hence much larger the deflection for the same force. This is the same case for the manipulated spoke in C2. As the supports are pushed outwards, they move further apart from each other. The increase in deflection, however, is not as strong as one would expect from the theory described above (L^3). Though the bending theory of a simply supported beam is straightforward and explains the increased flexibility, it can not be used to calculate the actual deflection of the spoke elements. This is because they undergo large deflections, and the small angle approximation of linear statics no longer holds. It is therefore only assumed that due to the non-linear behaviour of the waved spokes, increasing the distance between the supports has not such a large effect as for a straight and simple supported beam.

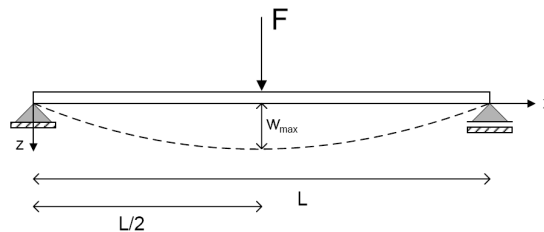


Figure 3.13: Theory of a simply supported beam. If the beam is loaded with a force at length $L/2$ the maximal deflection of the beam centreline is given with w_{max} . For the same force, increasing the distance between the supports increases w_{max} .

The turn in the stiffness curve is due to a secondary effect. To explain this, one must look not only on the centre inner spoke, which deforms due to the applied load, but also on the parallel spokes shifted 60° to the left and right, as measured from the central vertical axis (Figure 3.14).

When the separators are fully extended, the right arm of the left outer spoke and the left arm of the right outer spoke form an almost horizontal line. When the wheel is now loaded with a force, the centre inner spoke still wants to deform, but now the two arms forming the horizontal line transform into tension bands, which hold the outer rim in place. This counteracting tensile force decrease again the deflection. The same is true, when the outer spokes serve as the centre spoke. In this case, the two arms of the left and right inner spoke would transform into tension bands holding the outer rim in place.

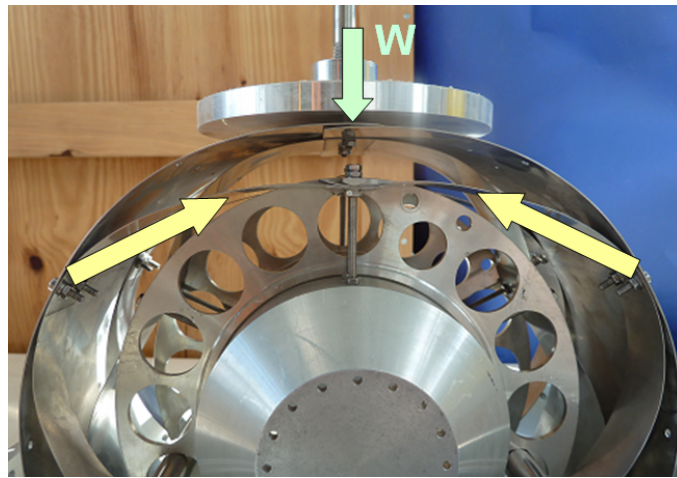


Figure 3.14: Concept 2 - Secondary effect leading to the turn in the stiffness progression. When the separators are fully extended and the wheel is loaded with a force the centre inner band wants to deform, but the outer bands are stretched and hold the ring in place. This counteracting tensile force decrease again the deflection.

Difference between Ground Contact Points

The difference of the stiffness at the different GCP's increases also, although not as much as for C3. The difference remains approximately constant in the beginning, but after the turn in the stiffness progression the difference increases slightly, which is also due to the secondary effect described above. The following two graphs (Figures 3.15 and 3.16) show the progress of the stiffness difference and the evolution of the deflection. The y-axes were adjusted to match the graphs for the same effect encountered by C3 (see Figures 3.7 and 3.8). The load of 131 N is the calibrated value from the set value of 150 N at the Bevameter.

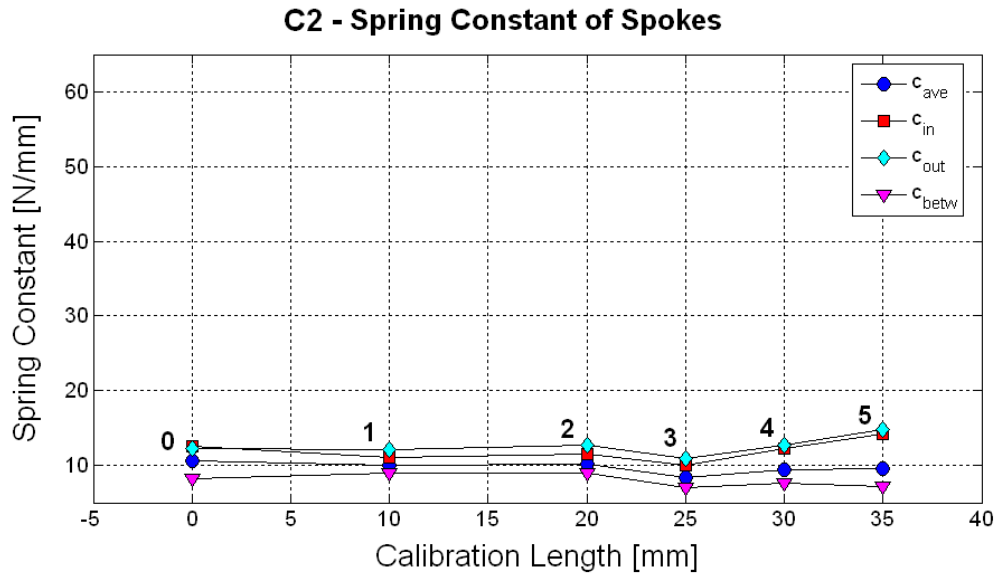


Figure 3.15: Concept 2 - Progress of the stiffness variation of the inner spokes (\square -) outer spokes (\diamond -) as well as the inter-spoke region (∇ -). The (\circ -) line represents the average over one full wheel turn.

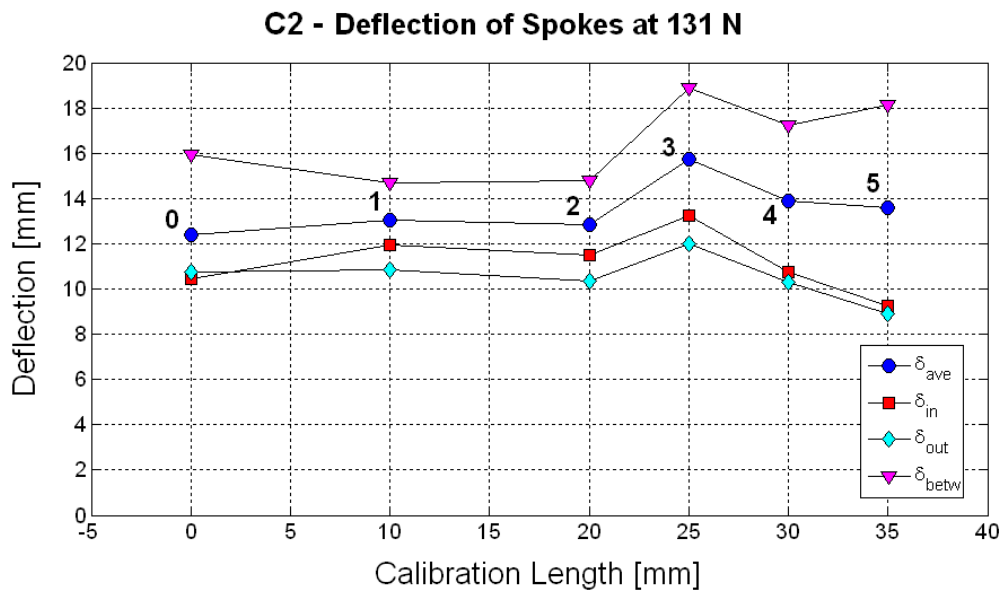


Figure 3.16: Concept 2 - Progress of the deformation variation of the inner spokes (\square -) outer spokes (\diamond -) as well as the inter-spoke region (∇ -). The (\circ -) line represents the average over one full wheel turn.

3.3.5 Radial Springs

The concept previously termed Concept 1 (C1), uses radial springs, which are placed between the wheel hub and the outer ring (Figure 3.17 Left). These springs, according to the required stiffness value, can be preloaded and compressed, thus giving the wheel a higher stiffness. When reducing the load again, the springs can relax and the wheel returns to its previous more flexible state.

The red arrows at the outer ring show the position where the load of a spring pushes against the ring, making it stiffer. The green arrows at the hub interface are required to be replaced by a mechanism to preload the springs. This could be done with an actuator and a linear moving pin or screw. This concept could also foresee progressive springs, which increase their stiffness non-linearly when compressed. In [29], progressive springs were analysed and a possible stiffness variation from 12 kPa to 27.4 kPa estimated for the baseline wheel design, assuming a wheel load of 150 N and a 10 mm calibration length. It was also assumed that these springs could be continuously adjusted.

3.3.6 Concept 1 - Revision

In [29], it was questioned in what way the flexible bands and the BSD could be removed from the baseline wheel and replaced by the radial springs in order to adjust the stiffness. It was noted that such a design would require a new wheel development to cope with the fact that the springs would also have to carry the shear forces, which in the baseline wheel are carried by the spokes. It was therefore concluded, that this concept is too complex and was not taken into further consideration. However, when these radial springs are added in addition to the flexible spokes in the baseline wheel (Figure 3.17 Right) they could be chosen in order to carry lateral forces only and to serve their main purpose to adjust the stiffness of the wheel. Therefore, this concept was reintroduced in the wheel trade-off and analysed in more detail (see Section 3.5).

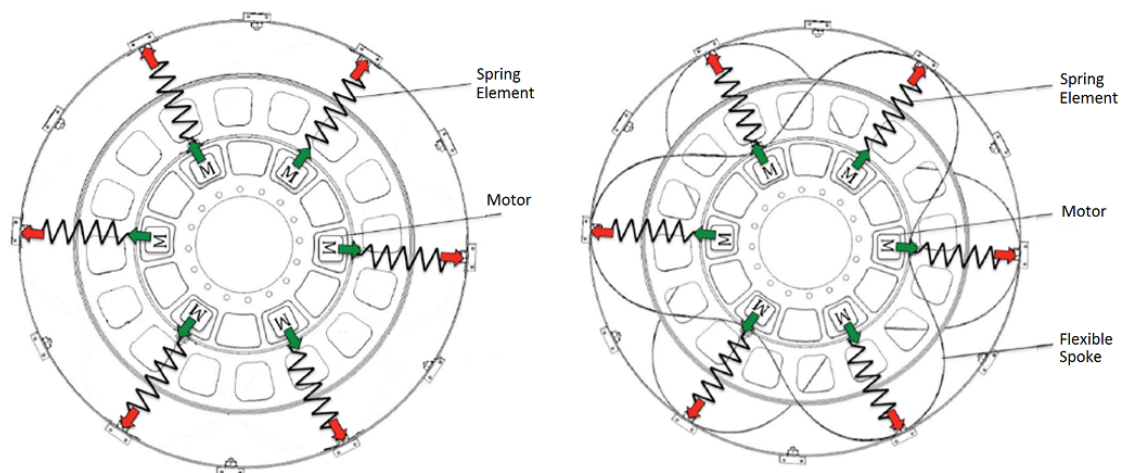


Figure 3.17: Concept 1 - Radial Springs. Left: Waved spokes replaced with radial springs. To vary the stiffness, these springs are preloaded through an internal linear actuator giving a defined force on the outer ring making it stiffer [29]. Right: Radial springs in addition to the waved spokes.

3.4 Assessment of Flexible Spokes

3.4.1 Waved Bands

During BB testing of the ExoMars Phase B1 Chassis and Locomotion Sub-System (LSS) in 2008, with the rovers "Bradley", tested by Oerlicon Space (OSZ), and "Bruno", tested by Macdonald Dettwiler and Associates (MDA), a phenomenon of excessive distortion of the flexible wheel elements was reported [31]. An example of this deformation is shown in Figure 3.18. It was also attempted to identify any possible causes for the occurrence of this anomaly. As any deformation in either the wheel rim or the wheel spoke would affect the wheel geometry and functionality by significant amounts, this is of vital interest.

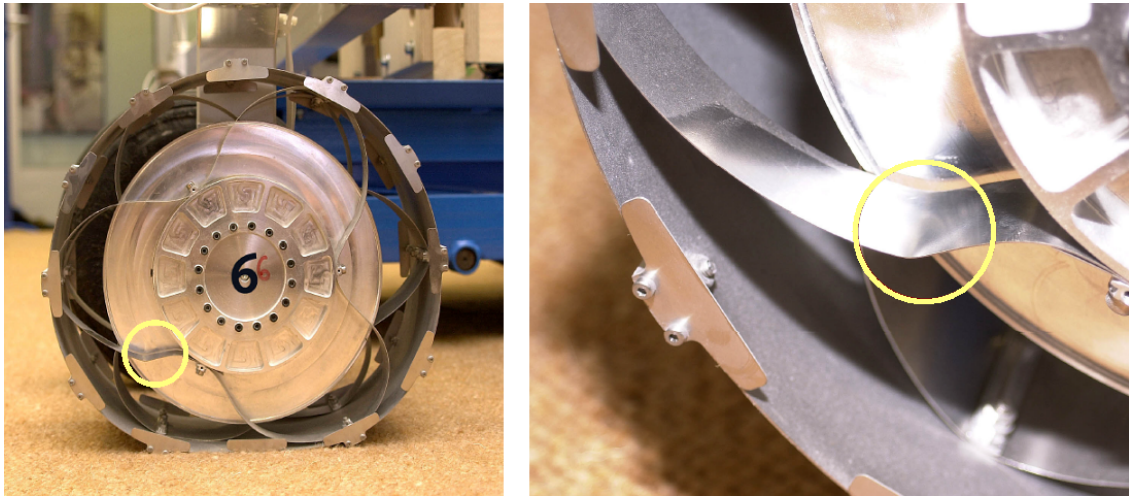


Figure 3.18: Left: Waved spoke plastic distortion occurrence as observed on all wheels during BB testing of the ExoMars Phase B1 in 2008. Right: Close-up on a fold location of one of the flexible spoke elements. (Credit: Astrium UK)

As possible causes a lower grade of the used spring steel and the method of forming the flexible lobed spokes were identified. It was also concluded that the three spoke design may be of insufficient strength to withstand the rough conditions in off-road type terrain. A preceding finite element analysis by OSZ in 2007 [25] had already noted that plastic deformation with this wheel design could be a potential problem when the wheel is subjected to high radial loads. It was recommended that the wheel design, the BSD in particular, should be adjusted. This would, however, have had a negative impact on the motion performance on soft soils, as the overall deflection of the wheel would have been decreased significantly. After the BB distortion occurrence, further analysis looking into the wheels behaviour during excessive torque situation, as well as the mechanical behaviour of the waved spoke design was undertaken at DLR.

Strain gauge measurements during a wheel torsion test in [32] depicted maximum stresses of around 900 N/mm^2 in compression and around 1860 N/mm^2 in tension which, depending on the quality grade of the spring steel (see Appendix C), may well exceed the yield limits of the spoke material. It was therefore concluded, that the step-down/up testing performed with the LSS BB demonstrator must have stressed the wheels beyond their design limit.

A simulation performed shortly after, described in [33], showed also that for the spokes with the materials and dimensions used, the critical bending radius, at which plastic deformation occurs, is ≤ 35 mm. The wheel design, however, including the limiting BSD's, was able to support a deflection down to a radius of 11 mm.

For the intention of introducing a stiffening system into the wheel, the waved spoke design suffers from another drawback. Due to the fact, that the inner and outer spokes are shifted by 60 degree to each other (refer to Figure 3.1), the stiffening system would require an equally adjustment of all inner and outer spokes. To achieve this, one would require at least 9 separate actuators (3 for the inner and 6 for the outer spokes) to implement a spring system as proposed for C1. This shift would be even more profound, when using only one central actuator inside the hub transferring a rotary into a linear motion, as was proposed for C2 and C3 (refer to Section 3.3.1 and 3.3.3). This would require the accommodation of all 9 manipulation points around the central element in one single system.

In summary, the waved spoke design is prone to plastic deformation due to both radial load cases as well as excessive torque. Thus, it can be concluded that this design, in combination with low quality spring steel, can neither support large radial deflections nor the acting shear forces due to the driving torque. In addition, including a stiffening system between the waved spokes would most likely result in a complex and delicate system which would incorporate multiple moving parts with fine margins to ensure a fail-safe operation mode.

3.4.2 Shear Plates

An alternative to the waved spoke design would be to simplify the spokes in order to increase the necessary space for a spring-damper-system and, in addition, handle the previously discovered problem of the plastic deformation. In [33] it was proposed to use "shear plates", which could be placed at equally distributed intervals around the wheel, connecting the hub and the outer ring (Figure 3.19).

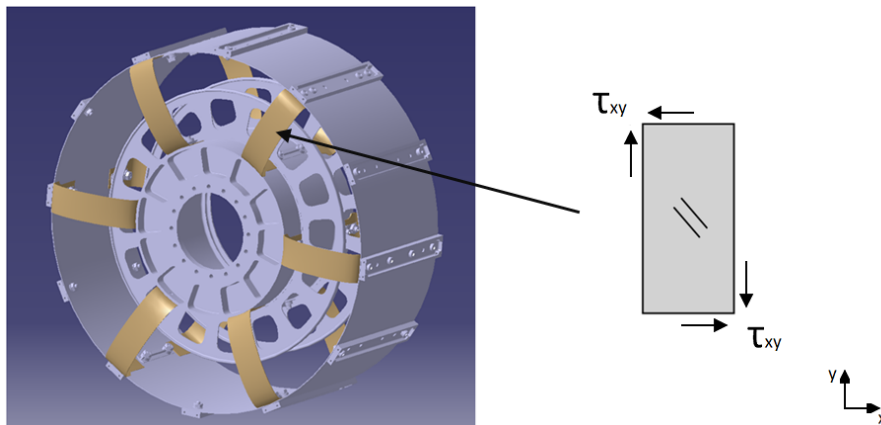


Figure 3.19: Left: Alternative to the waved spoke design using shear plates to withstand higher torque stresses. Right: Shear flow around a shear plate [33]

If the wheel is loaded in radial direction these shear panels can still deform, because they will bend outwards flattening the tread of the wheel to the ground. And when a torque is introduced from the drive unit, these panels would be well fitted to take the shear load and transfer the drawbar pull effectively to the ground (no deformation due to the increased moment of area in the rotational direction). This combines both rotational stiffness and radial flexibility!

To obtain a first impression and to visualise the behaviour of such a shear plate concept, a feasibility test was conducted. The spokes of the BB wheel were reconfigured to give the desired shear stiffness. The shear plates were equally distributed around the hub and depending on their position, they experience different cases of loading. The left image in Figure 3.20 shows the initial situation without loading (neglecting gravity). A radial load is introduced in the centre image showing the deformation of the shear plates, and a driving torque is simulated in the right image.

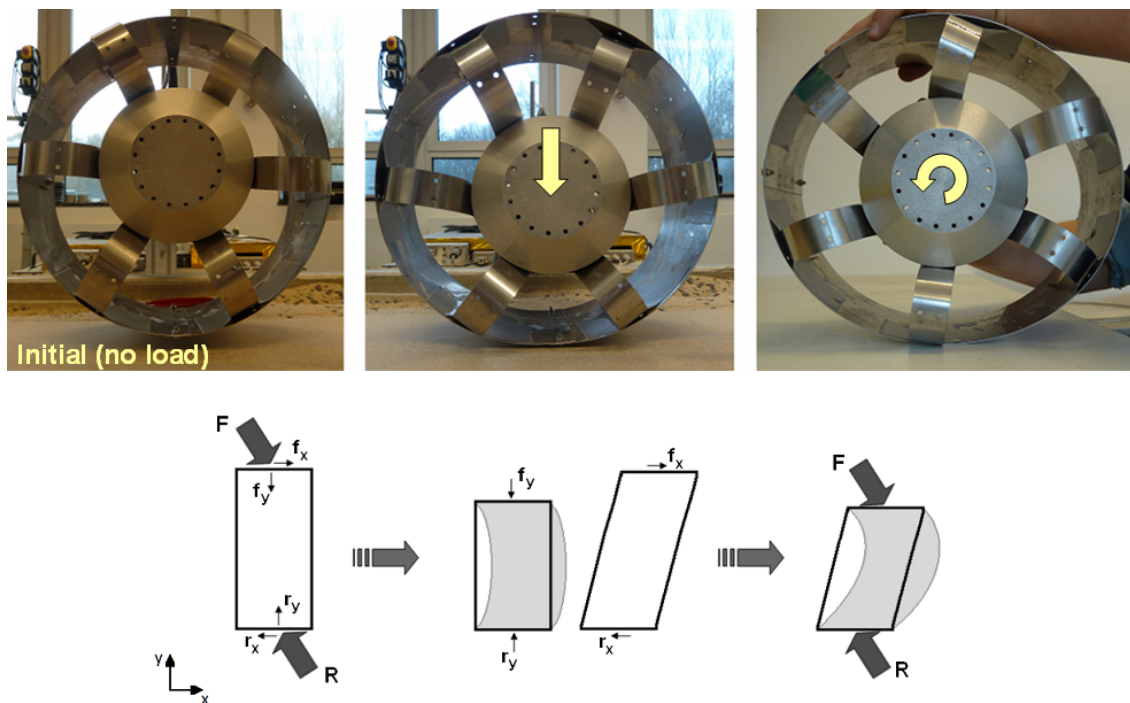


Figure 3.20: Shear plate feasibility test. Top left: Initial situation without load. Top centre: Wheel loaded in radial direction. Top right: Wheel subjected to a torque. Bottom: Shear plate load case of combined compression and shear

When the wheel load is not introduced in the principal axes of the shear plate a combination of compression/tension and shear is the effect (bottom of Figure 3.20). An additional driving torque leads to an increase in the shear component. Interesting to note is, that the shear plates are required to be slightly curved in order to guide the lateral deformation, in order to prevent buckling, but not so greatly curved that tension of the upper shear plates prevents the outer ring from deformation.

With this in mind, one can define the design factors which when combined determine the stiffness of the shear plates.

- Design factor 1: shear plate thickness
- Design factor 2: shear plate width
- Design factor 3: shear plate curvature

The number of the shear plate entities as well as their position and method of fixation, would need to be carefully investigated also. Due to the fact that the shear plates bend outwards, it is possible to argue that when deformed, they could interfere with the connected wheel drive and rover leg. However, as the deformation will occur in each case only at the ground contact the deflection will not interact with the rovers leg. As explained previously, this concept (now termed C4) allows space for the installation of a spring-damper-system, placed circumferential on top of the hub, by which the wheel flexibility could be adjusted.

In addition, such a concept would also separate the mechanisms of supporting the radial and the rotational loads, which is desirable as it simplifies the design in each case significantly.

3.5 Adaptive Mechanism

As explained above, this concept allows space for the installation of a mechanism dedicated to adjust the wheels flexibility. A possible idea picks up on the adaptation concept C1, where a spring is used to bring an additional force onto the ring, which then has a higher resistance to the wheel load and deforms less. In order to make such a spring adaptable a type of mechanism is needed to preload the spring. The higher the preloading, the higher the force onto the wheel and the higher the wheels stiffness. This can be done either by pushing against the ring at the ground contact or pulling the ring inwards at regions where the ring deflects outwards, in order to keep a circular shape. In terms of operation, pushing the hub away from the contact point and lifting the wheel upwards seems to be a good combination between a relative simple and reliable setup (pushing all springs around the hubs circumference evenly out) and a system, which can be easily adjusted to match certain ground conditions, as only one variable needs to be changed (compression distance of the springs).

In this way, an almost linear system can be created going from most flexible (zero preloading) to completely stiff, where the springs are compressed to their minimal solid length (Figure 3.21 Right). In order to preload the spring, a linear moving shaft needs to be implemented which presses the spring together. Such a mechanism could be achieved either via a single actuator in the hubs centre, which transforms a rotary motion into a linear movement pushing the shafts of the springs evenly outward or by direct linear actuators located peripherally around the hub, compressing each spring individually. For the reason that the hubs internal area is reserved for the sensor electronics, a hub internal stiffening system is not practical.

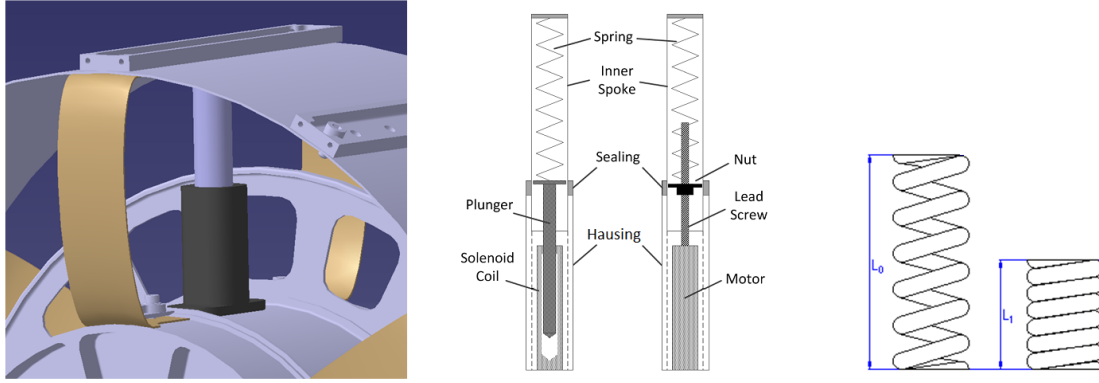


Figure 3.21: Left: Concept of a spring-damper-system inside the wheel, placed circumferentially on top of the hub, by which the wheel deflection could be adjusted. Centre: Schematic of a possible spring-damper configuration, with a solenoid actuator (left) or a lead screw actuator (right). The "inner spoke" is connected to the ring and can move all the way into the housing allowing for maximal wheel deformation. Right: Compression Spring unloaded (L_0) and loaded to minimal solid length (L_1).

A possible spring damper system is depicted in Figure 3.21. This idea utilises an electromechanical solenoid which is a thin and tightly packed loop of wire wrapped around a ferromagnetic core. When connected to an electronic current, this coil produces a magnetic field. Depending on the position of the positive and negative poles, and the strength of the current, the ferromagnetic core becomes a movable actuator with a linear motion. This linear movement would then be used to preload a spring increasing the force onto the outer wheel ring.

Figure 3.22, shows the operational principle of such a solenoid actuator. These type of actuators are usually designed for a particular force they need to produce and not for the traveled distance of the plunger. The force F is directly related to the applied electric current

$$F = \frac{\mu_0 \cdot A (N \cdot I)^2}{2 \cdot g^2} [N] \quad (3.8)$$

where μ_0 is the permeability of free space, also known as the absolute permeability, given by $4\pi \cdot 10^{-7} [H/m]$, N are the number of turns in the coil, I is the current in Amps, A is the area enclosed by the coil and g is the gap between the shell and the plunger (air gap). The energy to operate such a device is then found through the electromagnetic field energy E_f

$$E_f = \frac{1}{2} \cdot L \cdot I^2 [J] \quad (3.9)$$

The inductance L , is usually defined for a coil of length l

$$L = \frac{\mu_0 \cdot A \cdot N^2}{l} [H] \quad (3.10)$$

but needs to be extended here to the inductance of a coil with a ferromagnetic core and air gap to suit the equation for the required energy of a solenoid actuator.

$$L = \frac{N^2}{\mathfrak{R} + \mathfrak{R}_g} [H] \quad (3.11)$$

where \mathfrak{R} is the magnetic reluctance of the ferromagnetic core given by

$$\mathfrak{R} = \frac{l}{\mu_0 \mu_r A} \quad (3.12)$$

with μ_r being the relative permeability, which is the permeability of a conductor relative to that of free space. For soft iron it is around 6000, so its actual permeability is $6000 \cdot 4\pi \cdot 10^{-7} [H/m]$. And \mathfrak{R}_g is the magnetic reluctance of the air gap

$$\mathfrak{R}_g = \frac{g}{\mu_0 A} \quad (3.13)$$

Using Equation 2.5, we can relate the force given by Equation 3.8 to the traveled distance, which is then defined by the characteristic spring constant of the implemented spring. For the design it is then required to define that the springs when fully compressed balance the load onto the wheel.

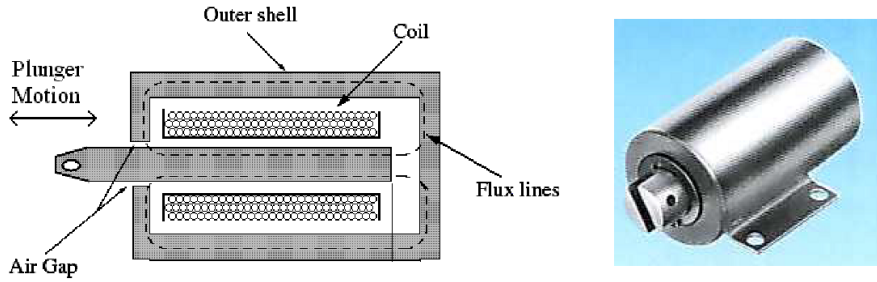


Figure 3.22: Left: Operating principle of an electro-mechanical solenoid actuator. When connected to an electronic current, the coil will produce a magnetic field. Depending on polarisation and the strength of the current, the metallic plunger will then move linearly in or out of the housing [34]. Right: Example of a standard solenoid actuator (Credit: Decco)

A similar method, which would require less energy, is the use of a linear lead screw actuator (also depicted in Figure 3.21). With this mechanism a rotary motor (stepper motor) is connected to the lead screw, making a lead nut move along the rotational axis. The direction of the translation then depends if the motor is rotated clockwise or counterclockwise.

The advantage of such a stiffening system is, that the lead screw has a continuous ramp that allows a small rotational force applied over a long distance. Hence, a large load can be lifted with a relatively low torque. Another advantage would be that such a system is self-locking. This means that when the power supply is switched off, the lead screw would prevent the lead nut from sliding down again. As a result, the adjusted distance of the lead nut, and therefore the compression load onto the spring, would be kept even when the power supply to the wheel fails.

3.6 Statement

The revision of Concept 3 and the experimental analysis of Concept 2 have identified major weaknesses in the previously proclaimed functionality. Recollection of the plastic deformation problem of the baseline wheel, including the complicated arrangement of the waved metal bands, leads to the conclusion that none of the previously devised concepts are suited to achieve the objective. The intention of the project, however, to develop a flexible metal wheel with adjustable stiffness was sustained. It was therefore decided to continue with the here proposed alternative Concept 4, albeit this raises the possibility of unforeseen difficulties (Table 3.7).

The new design will include the development and design of the shear plates and a spring-damper-system. The outer ring, hub, bump stop discs and grousers will be taken from the ExoMars design and scaled in order to fit the new dimensions. To meet the RIMRES project schedule the development and design of the shear plates and the spring-damper-system will be regarded separately. A detailed report about the trade-off and feasibility study outlined here can be found in [35].

Table 3.7: Decision matrix of the feasibility study showing the trade between the revised concepts (Concept 1 - 3) as well as the new alternative Concept 4. Concept 0 was added here representing a scaled ExoMars wheel with no adaptable capabilities.

	Complexity	System size/mass	Stiffness variation	Differences in GCP's	Risk	Time	Innovation
Concept 0	low	low	none	moderate	low	not critical	none
Concept 1	high	high	not tested	moderate	moderate	critical	moderate
Concept 2	moderate	high	little	moderate	moderate	ok	moderate
Concept 3	high	high	little	high	high	ok	moderate
Concept 4	moderate	moderate	not tested	not tested	high	critical	high

Colour code	good
	ok
	critical

4

WHEEL DESIGN

This chapter is concerned with the mechanical design of the RIMRES wheel and with the flexible spokes in particular. First, the requirements are reviewed in order to define specific boundary conditions for the evaluation process. The analysis method is explained and justified, giving examples to introduce the principle of the new design concepts, which are then analysed with a computer based method of non-linear finite elements. Each analysis is then concluded with a revision process where the mechanical characteristics of the design under consideration are summarised stating also possible refinements.

4.1 Requirements Review

4.1.1 Load Cases

As outlined in Section 3.2, the requirements for the RIMRES rover indicate the loads the wheel needs to sustain during operation. Different forces and moments are applied to the wheel structure due to the rovers own mass on different slopes as well as the torque applied by the drive actuators. It is obvious that different operation modes will change the momentary load on the wheel. For the first design, however, we will focus on the main three load cases, which are

1. The wheel load (W)
2. The drive torque (T), and
3. The side skid force (F_s)

These load cases are represented graphically in Figure 4.1. The wheel load is given by Equation 3.1 but will be rounded up to $W = 600\text{ N}$ to cover changes of the gravity vector when single module packages are shifted around the rovers body (refer to Section 3.2.1).

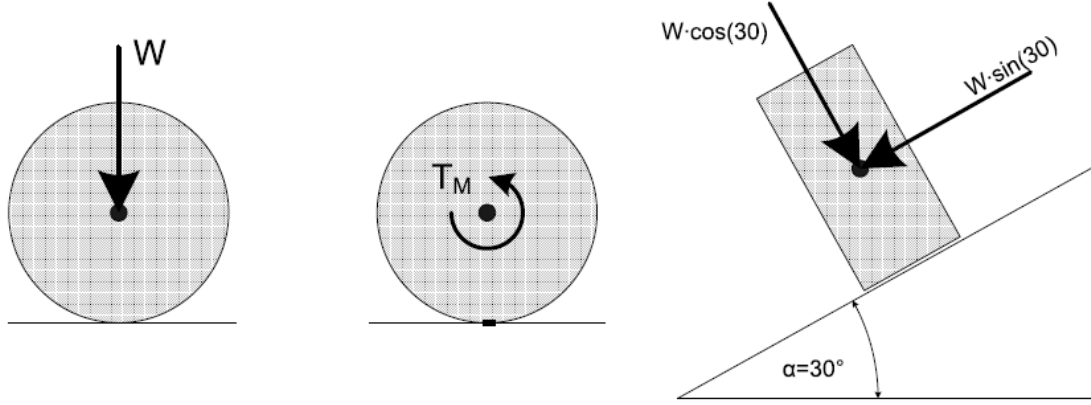


Figure 4.1: Different load cases resting on each wheel depending on the operational mode of the rover. Left: Load Case 1 - Maximal wheel load W acting in radial direction due to the rovers own system mass. Centre: Load Case 2 - Maximal torque load T_M due to the rovers drive unit (fixed at the bottom). Right: Load Case 3 - Maximal side skid force when driving cross slopes at an angle of 30°

The maximum torque is given by the momentary peak load of the used actuator $T_M = 127 \text{ Nm}$ (refer to section 3.2.1). To analyse the slope gradeability and to achieve at least the same performance as the baseline wheel a slope angle α of up to 30° was assumed. This corresponds to a side skid force of

$$\begin{aligned} F_s &= W \cdot \sin \alpha \text{ [N]} \\ &= 300 \text{ N} \end{aligned} \quad (4.1)$$

4.1.2 Materials and Stress Criterion

The loads are introduced at the centre of the wheel. The rigid hub, made of aluminum, builds the interface to the drive unit and evenly distributes the forces onto the wheel. As a result, the connection points located circumferentially around the hub are the points where the different load components are passed into the flexible elements. The material of the spokes and the outer ring will be spring steel, as is the case for the baseline wheel. Spring steel can be manufactured in different grades of quality, and specifically when formed into thin sheets with special treatments can sustain high stresses without yielding. For this analysis, however, we will focus on typical values of spring steel with reasonable quality. The material properties (Appendix C) are defined with

$$\begin{aligned} E &= 195 \text{ kN/mm}^2 \\ \nu &= 0.29 \\ R_{p0.2} &= 500 \text{ N/mm}^2 \end{aligned}$$

Where E is the module of elasticity, ν the Poisson's ratio and $R_{p0.2}$ the offset yield point of high strength steel such as spring steel. Referring to [25], the wheel shall be designed such that it can survive yield loading conditions and subsequently meet all performance requirements without any degradation. This will be ensured by a factor of safety for yield stresses of not less than

$$FS = 1.25$$

In order to ensure results which exclude plastic deformation all stress levels inside the material need to be below the yield limit. As we deal with the deformation of steel, which is a ductile material, we will use the von Mises yield criterion formulated in terms of the von Mises stress, also known as the equivalent tensile stress. It has to be noted here, that the von Mises stress is not an actual stress acting inside the members. The von Mises yield criterion is a hypothesis only, in which the assumption is made that the load inside the material is characterised by the part which corresponds to the change of the geometry at constant volume [36]. It is merely a comparison of normal stresses σ (compressive and tensile) and shear stresses τ giving a combined value to assist in predicting yielding of materials under multi-axial loading. The von Mises yield criterion is in agreement with most experiments for ductile materials, is always a positive value and can be expressed mathematically in the principle directions with

$$\sigma_v = \sqrt{\sigma_1^2 + \sigma_2^2 - \sigma_1\sigma_2} \quad (4.2)$$

and according to local axes

$$\sigma_v = \sqrt{\sigma_x^2 + \sigma_y^2 - \sigma_x\sigma_y + 3\tau_{xy}^2} \quad (4.3)$$

where σ_v , including the safety factor, must be below or equal the yield strength of the material σ_y .

$$\sigma_v \cdot FS \leq \sigma_y \quad (4.4)$$

4.1.3 Wheel Stiffness and Deflection

The stiffness of the wheel will depend on the deflection distance of the local ground contact point (GCP), in order to achieve a required ground pressure for either highest efficiency or highest traction (refer to Section 2.3.2). As has been previously discussed in Section 3.2.2, the "maximal nominal deflection" of the RIMRES wheel (no BSD contact) shall occur when the rover is loaded with its maximal payload capacity and operates on a solid surface with the electromechanical stiffening system not in use (passive/failure mode). For the calculation process of the required stiffness, we refer to the diagram in Figure 2.10 but neglect the sinking coefficient z_o for soft soil. Recalling Hooke's law of elastic deformation (Equation 2.5) we determine the characteristic spring constant by defining the desired deflection.

For a good starting point we have a look at the ExoMars baseline wheel, where the diameter of the BSD was set to $d_{bs} = 190 \text{ mm}$. This enables a maximal deflection of $\delta_{bs} = 30 \text{ mm}$, which is 12% of the wheels diameter. Using this value for the RIMRES wheel would result in a deflection with BSD contact of 48 mm. As we need to find a limit that lies below this value, and taking into consideration that different GCP's might deform more than this average value, we will define the "maximal nominal deflection" to a factor of 10% of the undeformed wheel diameter. This implies a possible passive/failure deflection of $\delta_{10} = 40 \text{ mm}$ for the designed wheel load of 600 N.

For both wheels, the exact value of the applied wheel load when reaching the BSD's is unknown. In order to obtain an estimate, and to be able to compare both wheels in terms of their equivalent stiffness p_{gr} , we calculate the design load for the ExoMars wheel using the same methodology as used for the RIMRES wheel (Equation 3.1). But now using values of $g = 3.7 \text{ m/s}^2$ (gravitational constant of Mars) and $n_w = 6$ (number of wheels used on the ExoMars rover).

The resulting relation of deflection and stiffness are summarised for both wheels in Table 4.1. The contact length l_t , the contact area A and the ground pressure are derived from Equations 2.6 to 2.8. Additionally, for comparing purposes, the measured values of the baseline wheel (refer to Chapter 3) are provided. As the RIMRES wheel foresees a system to adjust its stiffness it will nominally have a higher flexibility. In order to achieve smaller deflections, similar to the one for the ExoMars wheel ($\delta = 5\%$), the deflection must be balanced by the stiffening system.

Table 4.1: Determination of the wheel stiffness and allowable deflection. Top section: Key dimensions of the ExoMars and the new RIMRES wheel. Second section: Deflection limit when reaching the BSD of the baseline wheel gives an estimate of the BSD contact deflection for the RIMRES wheel. Third section: Definition of the equivalent stiffness for a nominal 10% deflection. Last section: Comparison of the measured equivalent stiffness to an envisaged RIMRES scenario, where the stiffening system will be used to balance the higher flexibility of the RIMRES wheel in order to achieve a smaller deflections of 5%.

ExoMars			RIMRES		
Variable	Value	Unit	Variable	Value	Unit
Key dimensions					
D	250	mm	D	400	mm
b	112	mm	b	200	mm
d_{bs}	190	mm	d_{bs}	≥ 300	mm
Deflection limit at bump stop					
W_{bs}	N/S	N	W_{bs}	N/S	N
δ_{bs}	30	mm	δ_{bs}	48	mm
δ_{bs}/D	12	%	δ_{bs}/D	12	%
l_{tbs}	162.5	mm	l_{tbs}	260	mm
A_{bs}	18197.9	mm^2	A_{bs}	51993.9	mm^2
Design for 10% deflection					
W_{Mars}	154.2	N	W_{Earth}	600	N
δ_{10}	25	mm	δ_{10}	40	mm
δ_{10}/D	10	%	δ_{10}/D	10	%
l_{t10}	150	mm	l_{t10}	240	mm
A_{10}	16800	mm^2	A_{10}	48000	mm^2
p_{gr10}	9.2	kPa	p_{gr10}	12.5	kPa
Measured			Adjusted		
W_{mv}	131	N	W_{adj}	600	N
δ_{mv}	12.5	mm	δ_{adj}	20	mm
δ_{mv}/D	5	%	δ_{adj}/D	5	%
l_{tmv}	109	mm	l_{tadj}	174.4	mm
A_{mv}	12204.9	mm^2	A_{adj}	34871.2	mm^2
p_{grmv}	10.7	kPa	p_{gradj}	17.2	kPa

4.2 Analysis Method

Figure 4.2 shows the expected deflection of an initially curved shear panel due to the influence of the wheel load W acting in the negative global Y-axis. The force R in the positive Y-direction is due to the reaction with the ground and holds the system in static equilibrium. Rotating the wheel schematic by 90° , it can be seen that the panels undergo a large deflection in the local yz-plane, with the point of maximum deflection changing horizontally by d_1 and vertically by d_2 . The loading remains vertical, so when the loaded support shifts along the local y-axis, the angle of attack into the plate changes significantly from α to β . This deformation is possible, because the plate is very thin compared to its length and permits bending around the local x-axis (low second moment of area in the local yz-plane).

From this it follows, that basic assumptions, such as the small angle approximation, are not longer valid and the solution of this large deflection cannot be obtained from elementary beam theory. Specifically, the elementary theory provides no correction for the shortening of the moment arm as the loaded end of the beam deflects [37]. This means that follower end forces can not be considered. However, they are of great importance when determination of the internal stresses in the member is required.

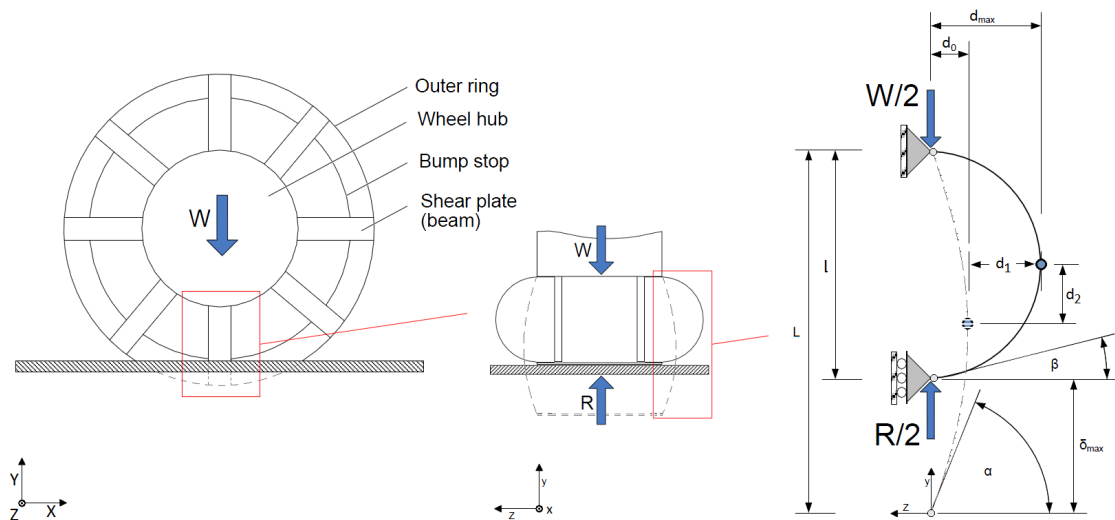


Figure 4.2: Schematics of a shear plate wheel showing the expected large deflection of the panels due to the radial load. As the assumptions in linear statics provide no correction for the shortening of the moment arm for such large deflections a non-linear approach will be necessary in order to determine the stresses and strains in the wheel members.

From the aforementioned information, it becomes clear that an approach from linear statics would not reveal a meaningful result and that a non-linear analysis of the given problem is inevitable. Investigations were conducted to identify the necessary means to perform a non-linear analysis of the problem and still be able to design and manufacture the system according to the underlying project schedule. Different methods were considered to approach such a question

- Analytically,
- Experimentally, or
- Numerically

by computer simulations. Over the last decades attempts have been made to describe non-linear large deflection problems on an analytical basis. A promising method is the use of non-linear differential equations based on the fundamental Bernoulli-Euler theorem, which states that the curvature is proportional to the bending moment [37]. However, it was found that such an approach would fall into a different domain and it was questioned to what extent this would help from a systems engineering point of view, as generally these mathematical models have no closed solution.

Another interesting mathematical approach for such problems, is the description via an equivalent system. The closest examples to the given problem were the publications of compliant mechanisms by L. Howell [38], where so called pseudo-rigid-body models were used to describe large deflections of cantilevered beams (Figure 4.3). However, beside the probable increase in assumptions and simplifications, it was questioned to what extent such an approach would provide answers to the internal stresses of the wheel components. Furthermore, the deflection of the whole wheel, including the different forces acting on each shear plate element, can not easily be determined. The system of a flexible wheel with its spokes and outer ring loaded with various combinations of compression, tension and shear appeared to be too complex, as such an analysis, utilising single beam elements only, would reveal the actual systems behaviour.

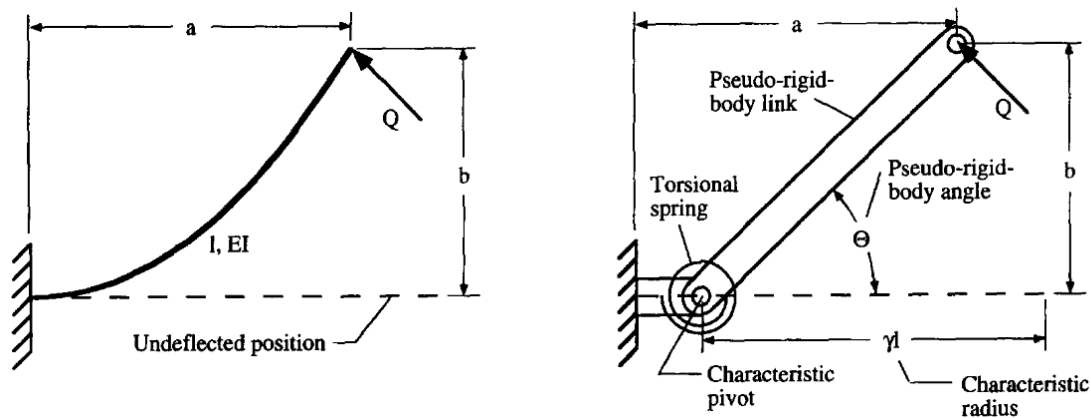


Figure 4.3: Compliant Mechanisms. Left: Flexible segment of a cantilevered beam. Right: Pseudo-rigid-body model describing the same deflection with simple elements. (Reproduced from [38])

The second method considered was to conduct experiments, to investigate the behaviour of the large deflections with different sets of metal strips equipped with strain gauges. Without values based on a mathematical approach, the experimental method is sometimes the only way to obtain practical results. However, without a starting point, trial and error experiments are complex, sensitive and very time consuming. It was therefore reasoned that such an approach would not lead to usable results in the given time frame.

Due to the fact that numerical codes for finite element analyses (FEA) have been developed to approach both linear and nonlinear mechanical problems, it was concluded that a computer based approach would be the most promising to achieve usable results in an acceptable time. The program bundle Marc/Mentat from MSC Software provides a complete solution to model systems with geometric nonlinearity, nonlinear forces, large displacement of boundary conditions (BC), as well as nonlinear contact conditions.

To reduce pre-processing time even further, the models were built and meshed in Patran and then imported into Mentat to apply the BC's. Marc, the nonlinear solver, was then used to solve the stiffness matrix and to find the resulting displacements of the element nodes. It should be noted, that the performed analysis is only a simplified investigation to obtain indications on how the system behaves in general and how the elements need to be designed in order to sustain the design loads. The results of this analysis will then serve as the baseline for the design and manufacturing process. However, the results need to be carefully tested afterwards with the new RIMRES BB demonstrator wheel.

4.3 Shear Plates

4.3.1 Buckling Columns

When thin beams undergo displacements due to a compressive force as described above, the term used for such a behaviour is "buckling", which may be either stable or unstable. Stable buckling can be achieved when the column has an initial deflection angle, which permits increasing displacements proportionally with increasing load. When a column has no initial deflection angle, however, and the loading reaches the critical value F_{crit} , the column will break-off uncontrolled and instantaneous to one side or the other.

$$F_{crit} = \frac{\pi^2 EI}{(KL)^2} \quad (4.5)$$

where E is the modulus of elasticity, I is the second moment of area, L the unsupported length of the column and K is the effective length factor, depending on the characteristic of the end supports (Figure 4.4).

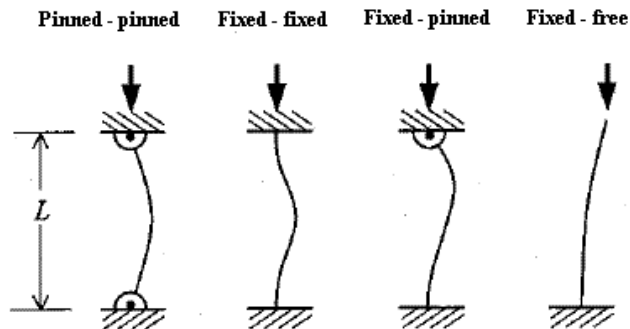


Figure 4.4: The boundary conditions affect the critical load of a slender column, which is characterised by the effective length factor K . Left: pinned-pinned ($K = 1$), Centre Left: fixed-fixed ($K = 0.5$), Centre Right: fixed-pinned ($K = 0.699$), Right: fixed-free ($K = 2$) [39].

The shear plate concept should enable stable buckling, where the transverse deflection increases steadily with increasing deformation of the wheel. For this purpose, the plates have to be slightly curved with an initial deflection offset. This in mind, and the fact that we deal with large displacements, we can not use the critical load theorem to derive the force required for stable deflections. As a result, we need to find a different way to estimate the plates deformation.

4.3.2 Deflection Curve Models

To introduce the deformation problem of the shear plate spokes and to obtain an idea of how the spokes would deflect under load, an attempt was made to find a good model, by which to estimate the curvature and the point of maximal deflection of such a bending beam. This information will be very valuable when evaluating the FEA results later.

Model A - Circle Segment

The first proposed model was already presented in Figure 4.2, where the assumption was made that the deflected beam would take the form of a half-circle when fully deflected, or a circle segment for smaller deformations. Referring to Figure 4.5 Left, the maximum distance the beam will bend outwards, assuming the shape to be that of a circle segment, can be stated mathematically as

$$d_{seg} = r - \sqrt{r^2 - \frac{l^2}{4}} \quad (4.6)$$

where r is the radius of the circle and l is the length of the direct connection between hub and ring. This can also be expressed in terms of the opening angle α

$$d_{seg} = \frac{l}{2} \tan \frac{\alpha}{4} \quad (4.7)$$

The length of the curved arc s is equal to the undeflected length of the beam, which is given with

$$s = l + \delta \quad (4.8)$$

where δ is the deformation of the wheel (shift of the support in Figure 4.2). When the beam is deflected, the arc length can also be expressed with

$$s = \frac{\pi \cdot r \cdot \alpha}{180^\circ} \quad (4.9)$$

From here we could determine the radius r , but we do not know the exact opening angle. As we have, however, two expressions for d_{seg} we equalise and solve numerically for the two unknown variables r and α . As a result, we find the deflected distance of the beam for a given beam length and a given wheel deformation.

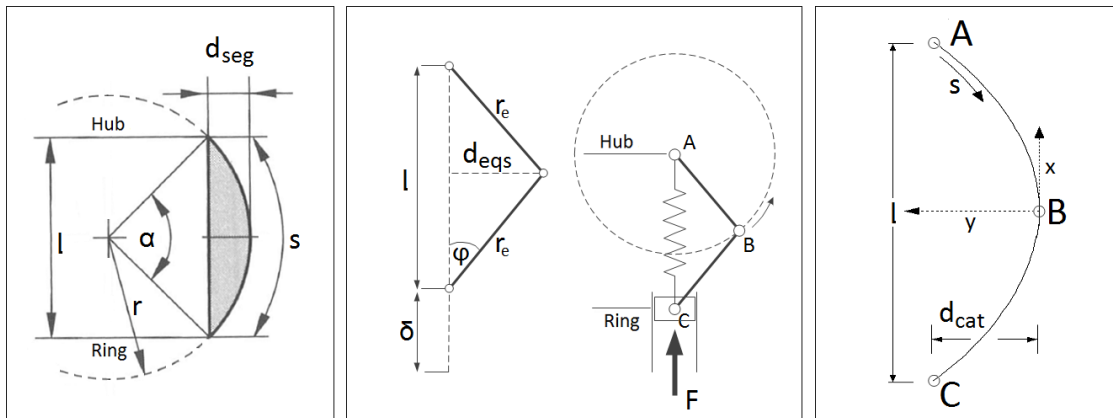


Figure 4.5: Deflection models of a bending beam for large deflections. Left: Circle Segment. Centre: Equivalent system. Right: Catenary

Model B - Equivalent System

Another approach to estimate the deflection of the beam is by replacing it with an equivalent system. Figure 4.5 Centre, shows such an example similar to a slider crank mechanism, where the beam is substituted with two rods of equal length r_e . A spring element placed between the hub joint (A) and the ring joint (C) symbolises the elastic behaviour of the beam. Assuming the pin joint (B) connecting the two rods has an initial offset from the vertical centre line (in order to prevent buckling) and the system is subjected to a force at the free end, the pin joint will move outwards in a circular trajectory. The distance this joint will travel is then defined by

$$d_{eqs} = \sin\varphi \cdot r_e \quad (4.10)$$

where the angle φ can be obtained by

$$\cos\varphi = \frac{l}{2 \cdot r_e} \quad (4.11)$$

The length l depends again on the radial deformation of the wheel

$$l = 2 \cdot r_e - \delta \quad (4.12)$$

Although we receive a better impression for the deflection of the thin beam with an equivalent system, it does not provide a clear picture of the curvature. The circle segment we outlined earlier is only valid for small deflections and is an oversimplification for large deflections. If for example a thin wire is pushed from both ends towards one another, the resulting curvature will first take the form of a thin circle segment, but for larger deflections it will form a near-parabolic shaped curve. This is because the distance of the lateral deflection does not increase proportionally with the distance of the axial shift.

Model C - The Catenary

This near-parabolic curve is known as the catenary, and it describes the shape of a rope hanging loosely from two fixation points under the influence of gravity (Figure 4.5 Right). The length s of such a rope between points A and C is given mathematically with

$$s = \int_a^c \sqrt{1 + y'^2} dx \quad (4.13)$$

where y' is the first derivative of the curvature. Assuming now a perfectly flexible rope with constant thickness, the curvature of a catenary is independent of the materials density [40] and takes the form

$$y = \frac{s_h^2 - d_{cat}^2}{2 \cdot d_{cat}} \cosh\left(\frac{2 \cdot d_{cat}}{s_h^2 - d_{cat}^2} x\right) - \frac{s_h^2 - d_{cat}^2}{2 \cdot d_{cat}} \quad (4.14)$$

where s_h is half the length of the arc (length between points A and B) and d_{cat} is the distance of maximal deflection for the catenary shape. From here also an expression for the length l can be obtained

$$l = \frac{s_h^2 - d_{cat}^2}{d_{cat}} \ln\left(\frac{s_h + d_{cat}}{s_h - d_{cat}}\right) \quad (4.15)$$

This formula provides the means to calculate l from d_{cat} and s_h . In order to obtain the unknown variable d_{cat} we solve this equation numerically [40].

To compare all three models, we define a radial wheel deformation of $\delta = 40 \text{ mm}$ and an undeflected length of the plates of 120 mm, which would be the case for a wheel with a ring diameter of 400 mm and a hub diameter of 80 mm. If we assume that Model C describes best the deformation curvature of the shear plate, it can be seen from Table 4.2, that the deflection model of the equivalent system (Model B) overestimates the beam deflection by more than 10%, whereas the model of the circle segment (Model A) clearly underestimates the deformation.

Table 4.2: Comparison of the maximal deflection distance d for the three alternative deflection models. A: Circle Segment. B: Equivalent system. C: Catenary

Model		Value (mm)
A	d_{seg}	37.2
B	d_{eqs}	44.7
C	d_{cat}	40.2

Relation to Stress

Assuming the catenary model is a good approximation of the deflection curve of the two-dimensional bending of the shear plate, it still does not provide information about the internal stresses of the beam. With the method of an equivalent system we could include a force and then relate the lateral bending to the axial compression. This force, however, would not act along the neutral axis of the member. The angle, and therefore the acting component of the force into the member, changes with each step. Such a force is also called a follower end force, as it follows the shifting end of the beam. The stress inside the member at each step is given by the momentary force component F_n over the cross sectional area A of the member

$$\sigma_n, \tau_n = \frac{F_n}{A} \quad (4.16)$$

The shear stresses due to strain can be neglected here as we have a slender beam which is much thinner than its length. Therefore, we deal with pure bending only (no regions of compression or tension along the neutral axis). Dividing the deflection process into n steps, we find the final stress level by the sum of all steps

$$\sigma = \frac{1}{A} \sum_{n=1}^n F_n \quad (4.17)$$

Splitting such an equivalent system even further into more members, we arrive at the concept of finite elements. The more elements and the smaller the step size, the more accurate will be the solution to the real world problem. Naturally, the greater the computational effort will be also. For this reason, the use of a computer based FE tool for this task is of significant assistance. The process used for the FEA of the wheel deformation, will be described in the following section.

4.3.3 Analysis

The overall goal of the FEA for the RIMRES wheel is to determine the stresses (σ , τ) and strains (ϵ , γ) inside the flexible elements in order to design the wheel so that it will sustain the loads acting on it purely elastically (no plastic deformation occurs in any of the elements). The dimensions found to fulfill this requirement, will then be used for the construction and manufacturing process.

FE Model

For this purpose a finite element model was generated based on hand calculations and sketches. Due to the fact that the wheel utilises thin-walled flexible elements the sketched dimensions were used to establish a surface model, which was then meshed using common meshing guidelines [41], including a structured and regular quad-element-mesh with no step changes and higher density only in regions of interest in order to reduce calculation time. This was enabled by subdividing the shell model into smaller sections, which were then meshed individually. However, in order to obtain a good estimate of how the wheel behaves as a system, the model was assembled as a full model. Although the wheel has a usable symmetry in the yz-plane (origin in the geometrical centre) this was not used in the first approach in order to avoid discretisation errors.

For this analysis we assumed that the shear plates would bend outwards and that they do not interact with the hub. For this reason, only the shear plate spokes and the outer ring were assigned as shell elements. The type of elements used were Quad4 (four-noded linear isoparametric flat plate elements), which behave well for irregular shapes. The use of Quad8 elements (parabolic isoparametric element with four corner and four edge grid points) was also considered as they behave slightly better for singly-curved shells [41]. This type has, however, the double amount of nodes and so processing time would be subsequently higher. Therefore, for the first iteration process Quad4 shell elements were used leaving the possibility for later refinements (e.g. p-refinement, h-refinement). These elements were then assigned the material properties (E and ν), which were already mentioned in section 4.1.2.

The FE model contained 12 shear panels (6 on both sides) as well as the outer ring of the wheel. A fine mesh was used for the shear plates, whereas a relative coarse mesh was defined for the ring. As the meshing was done in sections, additional nodes placed at the same location were equalised and merged into single nodes. Renumbering of the elements and nodes cleaned-up the element/node list, which is useful later when checking for errors. In order to prevent buckling, the shear panels were created using a 3-point circular curve with an initial lateral offset of $d = 5 \text{ mm}$.

For the first load case (wheel load) we simulate a situation where the wheel is pressed against a solid surface. To accomplish this, an additional flat plate was defined as the contact boundary for the wheel ring. For the given problem, there are two possible approaches to define the boundary conditions (BC's) in order to prevent rigid body motion and to hold the complete system in static equilibrium. One could locally fix (translational as well as rotational) the supports of the shear plates on the hub, moving the contact plate against the ring. Or one could fix the contact plate inside the simulation space and moving the hub, more precisely the shear plate supports on the hub side, in direction of the contact plate. The first method can be used in order to find the resistance/stiffness of the wheel according to the deformation length. The second method, on the other hand, could be used in order to determine the resulting deflection to a given load. The latter can also be used to simulate load cases two (torque) and three (side skid) as the supports can be set to move along or around a particular axis.

In the previous section we defined the deflection for the first load case to 40 mm. Therefore, we will use the first BC method of fixing the supports in all 6 degrees of freedom (dof), placing the contact plate just below the ring and moving it 40 mm upwards in the positive y-direction. Care needed to be taken with the contact sides of the two bodies. If the sides were not set facing each other, the bodies did not "know" each other and the simulation was unable to find a solution.

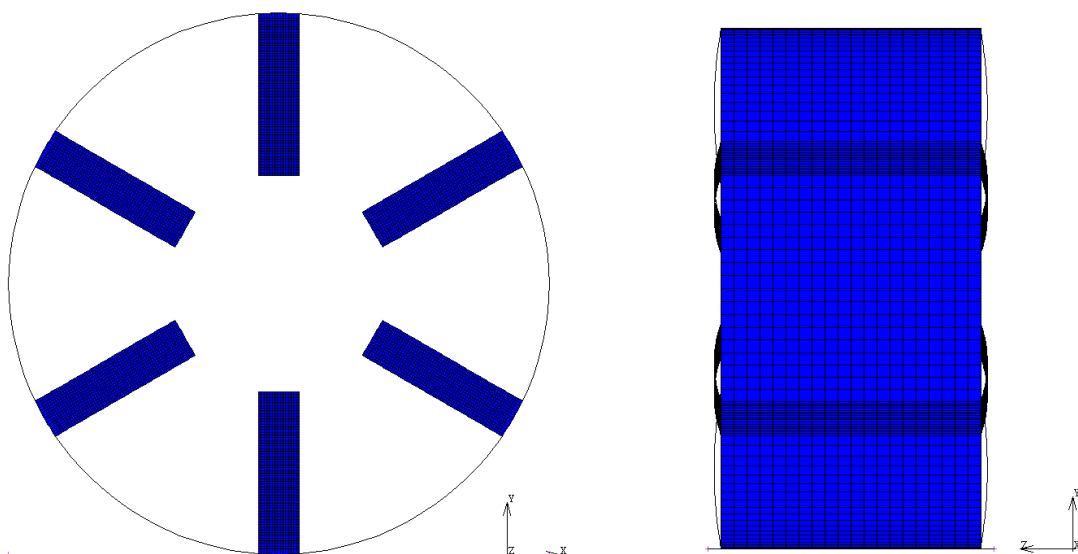


Figure 4.6: FE model of the shear plate concept using 6 panels on either side of the wheel ring. These panels have a length of 120 mm, a width of 20 mm and a thickness of 0.4 mm and are equally distributed at 60° intervals around the central axis.

To avoid slippage we set the static friction coefficient between the two bodies (wheel and plate) to $\mu_s = 0.5$, which is a good approximation for steel on a hard surface such as dry wood. The step size was initially set to 20 increments but needed to be increased to at least 50 in order to run the full simulation. The smaller step size, though faster, was unable to converge in some increments. The results of the first iteration process are shown in Figure 4.7.

Results

Looking at the results we see the expected outward bending of the lower panels which are in contact with the boundary surface. It is also visible that the deflection curve does not take the form of a circle segment. The assumption made previously of the catenary deflection model is therefore a good approximation, which is also supported by the deflection distance of 40.02 mm. This value is marginally less than computed earlier, because the deflection curve here has an initial deflection radius at both ends in the opposite direction.

To explain this, we look again at the supports and more specifically, at how they were defined. The supports were restrained on the hub in all translational, as well as in all rotational directions, which is a fixed-support able to support a bending moment (see again Figure 4.4 Centre Left). The estimation from the previous section assumed a pinned support, where the element would have been free to rotate around. This, however, is not possible with a continuous medium having no additional element in between which decouples the components. Due to continuity, if the support is fixed preventing rigid-body-motion a change at this point does not result in a displacement (translation or rotation) but in deformation (change in shape or size). The supports, though not matching the previous assumption, do reflect accurately the real world conditions. This can be shown in a more graphical manner with a look at the stress/strain relationship.

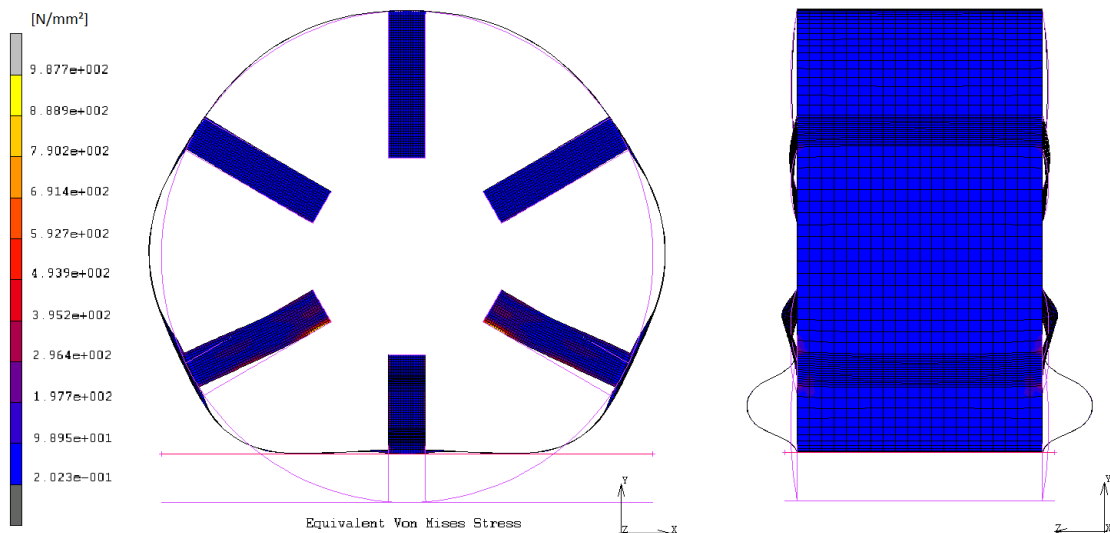


Figure 4.7: FE analysis of the shear plate concept. The upper central shear plate is in tension whereas the lower central one is loaded in compression. The upper left and right panels undergo a combination of tension and shear load. The highest stress levels reside in the lower left and right panels which are subjected to a combined compression and shear loading which heavily increases the local stress values at the corner points due to the relative large shear strain.

Figure 4.8, shows a diagram with the relation of stress and strain of steel. As mentioned above, the model was built as a continuous structure with the ring and the plates having a smooth curvature. The only sharp edges in this model are the connections from the plates to the ring on the one side and to the hub on the other side. These edges can be understood as sharp bends from one component to the next, which due to their sharpness are points of plastic deformation. Looking at the stress/strain diagram we see that a region which is plastically deformed becomes stronger due to dislocation inside the material's crystal lattice (strain hardening). If the beam is now subjected to a bending moment it will not bend at this locally strengthened region, which is why the compression of the plates will not bend at the connection points but rather at some distance away from it.

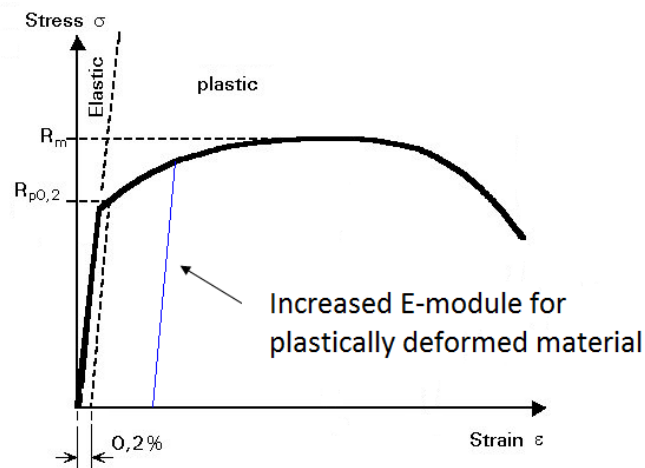


Figure 4.8: Stress/strain diagram of a high strength steel with continuous transition from elastic to plastic deformation [42]. $R_{p0,2}$ is the defined yield point at 0.2% deformation and R_m is the tensile strength of the material. The linear part of the curve is the elastic region and the slope is called the modulus of elasticity (E-module). If such material is plastically deformed, then a new increased E-module is created.

The stresses in this bent lower plate, as well as in the upper plate, which is subject to tension, are not critical and well below the yield limit. A more pressing matter are the plates on the left and right side of the lower plate, which are subjected to a combination of compressive and shear deformation. As explained in section 3.4.2, this combined loading was expected. However, as can be seen from the stress scale the values exceed the set yield limit by a factor of two. The problem here is that the hub moves downwards, because the upper plate has an initial curvature and permits the vertical shift. The ring on the other hand is pressed to the ground and does not retain its shape, which is why there develops a relative shift of the connection points between the hub and ring. The side plates can not bend the same way as the upper and lower plate as they have a higher moment of area in this global direction. As a result, the shear plates are subjected to a shift they can not compensate via bending, but by deformation.

In order to verify this problem we do a simplified static calculation. Figure 4.9 shows a panel set between two walls, which in this case are the hub on the lower side and the ring on the upper side.

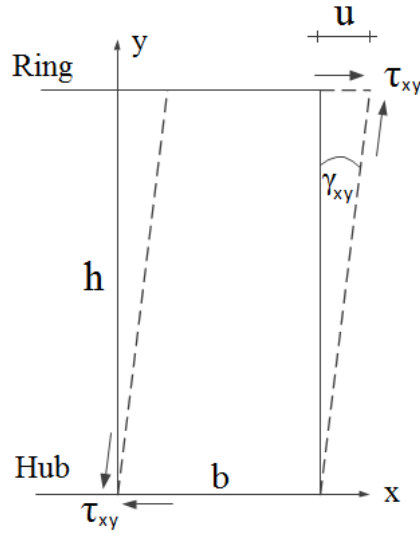


Figure 4.9: Shear displacement due to the shift of one side and the resulting stress-strain relationship obeying Hooke's law of elastic deformation. The length of the panel is given by h , its width by b and the displacement from its original position by u .

The idea of the shear plate was to provide rotational stiffness. If one applies a torque T at the hubs centre then the acting force F at the bottom side of the panel will be given with

$$F = \frac{T}{r} \quad (4.18)$$

where r is the radial distance from the centre to the bottom side of the panel. This force acts over the cross sectional area A of the panel and produces a shear stress τ (Equation 4.16).

If one assumes a hub diameter of 160 mm ($r = 80$ mm), a width $b = 20$ mm and a thickness $t = 0.4$ mm then the resulting shear stress due to $T_m = 127$ Nm acting on the panel is approximately 200 N/mm^2 , which is a factor of two (incl. FS) below the yield limit. However, If one takes a look at the resulting stresses due to the radial movement of the hub one obtains much higher stress values. From structural mechanics [36] we can relate the change in angle at the corner of an original rectangular element, also called shear strain γ , to the displacement kinematically by

$$\gamma_{xy} = \frac{\partial u}{\partial y} + \frac{\partial v}{\partial x} \quad (4.19)$$

where the displacement along the x-axis u and the displacement along the y-axis v are given with

$$u = \frac{\partial u}{\partial x} dx \quad (4.20)$$

$$v = \frac{\partial v}{\partial y} dy \quad (4.21)$$

As we have constraints preventing displacements from occurring in the vertical direction, and we want to determine the full displacement of the shear panel, Equation 4.19 simplifies to

$$\gamma_{xy} = \frac{du}{dy} \quad (4.22)$$

where $du = u$ and $dy = h$, which is the length of the panel. It follows the expression for the displacement

$$u = \gamma_{xy} \cdot h \quad (4.23)$$

The strain is found through the stress relation via Hooke's law

$$\gamma_{xy} = \frac{1}{G} \tau_{xy} \quad (4.24)$$

where G is the shear modulus, which depends on the modulus of elasticity E and the Poisson's ratio ν of the material

$$G = \frac{E}{2(1 + \nu)} \quad (4.25)$$

Inserting Equations 4.23 and 4.25 into 4.24 we find an expression for the shear stress due to the displacement u

$$\tau_{xy} = \frac{u}{h} G \quad (4.26)$$

If one now assumes a relatively small displacement of $u = 2 \text{ mm}$ and using the material properties given in Section 4.1.2, then the resulting shear stress for a panel of length $h = 120 \text{ mm}$ becomes $\tau_{xy} = 1260 \text{ N/mm}^2$ which is well above the yield limit and in the same order of magnitude as the values provided by the simulation (refer to Figure 4.7). Although in the simulation the panel is subjected not only to shear but also to a bending moment, which is the reason for the stress concentration in the corner, one can clearly see that due to the displacement the resulting stress at the contact interface reaches a critical value.

Design Revision

It becomes clear that the problem above does not arise due to the bending normal stress of the plates, but due to the strain of the material. Whilst the plates are well equipped to take a rotational load from the drive, they do not behave well for large shear displacements, which cause very high shear stresses at the contact interfaces. The von Mises yield criterion given in Equation 4.3 gives the interaction of normal stresses (here due to bending) and shear stresses. According to this, the shear stresses are assumed to be taken into account with a factor of three. From here it follows, that shear stresses inside a member have a much greater effect to the overall stress value than the components in the normal direction. It is therefore advisable to reduce shear stresses, or even avoid them altogether, as they are most likely to be the cause of failure.

Looking at Equation 4.26, it is possible to increase the length h of the panel in order to reduce the shear stress, but this is not practical as one would have to lengthen h to at least 300 mm before the resulting stress reduces below 500 N/mm^2 . Besides, with the given wheel diameter of $D = 400 \text{ mm}$ this not possible. Changing the width or the thickness of the panel would not have an effect, as we see in Equation 4.24, that the shear strain due to a defined displacement does not depend on these factors. With this in mind, an attempt was made to find a solution that does not take the load via shearing but through bending and/or tension.

It was mentioned earlier, that the displacement of the hub is due to the initial curvature of the upper plates. Ignoring such an initial curvature would equalise the downwards movement of the hub and the ring. The ring would press against the ground and deform into a uniform ellipse. The plates on the left and right side would, however, prevent this, pulling the wheel into a multi-curved shape (Figure 4.7). For the fact that these tensile forces do not act in the principal axes, we would have to deal again with high shear forces. Additionally, neglecting an initial curvature would result in a stability problem, in which due to unstable buckling (refer to Section 4.3.1), it would be unpredictable as to when and in which direction the plates would snap.

4.4 Tension Blades

Although designed to take the acting torque, the shear strain weakness of the shear plate concept is a major problem. The only possibility in this case seems to be to convert the shear plates into tension blades. Rotating the shear plates by 90° the lower moment of area would then enable the deformation due to the downward movement of the hub. The stress problem would then transform into a tension problem rather than a shear deformation problem.

As we have seen earlier, the plates sustain loads along their principle axes better than across it, just like tension rods on a truss structure. The load carrying principle of tension cables was first used on bridges where the roadway was suspended from a load carrying arc fixed to a pylon, which then transmitted the load into the ground. Since the end of the 19th century [43] this concept materialised also in the form of the tensioned spoke wheel, or more commonly known as the bicycle wheel. The reaction of such a wheel to a radial load is that it flattens a little at the contact area to the ground, whereas the rest remains approximately circular (Figure 4.10). The tension on those spokes directly beneath the hub reduces therefore slightly and the wheel could be understood to "hang" from the arc above the hub via the spokes, which have now a relatively higher tension (refer to Figure 2.13, top-loader principle).

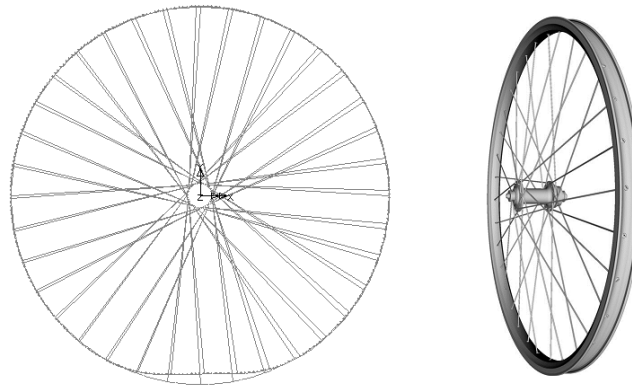


Figure 4.10: Principal of the deformation of a bicycle wheel due to the contact with the ground (exaggerated view by factor 100) which locally decreases the tension at the spokes directly below the hub. As a result, the wheel hangs from the arc above the hub via the other spokes which have now a relatively higher tension [44]

4.4.1 Variant A - End Curved

In bicycle wheel building there are basically two methods for placing the spokes between the hub and the rim, which are tangentially or radially [45]. The spokes in the latter go straight from the hub to the rim and do not cross others. Tangential spokes on the other hand run diagonally from the rim to the particular tangential point on the hub. This allows a better transfer of the torque and is therefore commonly used for drive wheels. Bicycle wheels have a high load to weight ratio, which is why they are often preferable to full-disc wheels (train wheel) or wheels with their spokes loaded in compression (horse carrier wheel). But they are of stiff design and do not support large deflections. In order to convert this concept into a flexible design the spokes would have to be slightly curved, to support bending and most importantly, prevent unstable buckling.

Single Spoke Analysis

Looking back at the ExoMars design, we see that the waved bands have a relatively large curvature which enables the bands to bend outwards when subjected to compression. They do, however, take the complete wheel load via the compression of the bottom spokes rather than in tension of the upper ones. To enable the upper spokes to carry part of the loading we must reduce this curvature. To save time and to obtain a good image of how the spokes would deform for different curvatures, we set up an intermediate FE model of a single spoke sub assembly.

These sub-assemblies were again created as surface models, which were then section-wise meshed with quad-elements of thickness 0.4 mm. Four different geometries were constructed, in each case a pair of blades builds a spoke element. The blades were attached to the hub at an angle of $\pm 60^\circ$ from the local vertical and shifted with respect to each other along the hub width in order to open the possibility for sideways movement. In two models, the blades initially crossed each other and had different connecting points at the ring. The blades in the other two models shared a common connecting point on the ring. The blades were created having no initial curvature but were bent either inwards or outwards at the ring interface. A section of the hub was also included as it was expected that in some models the blades would lean themselves against it. This hub section, including all nodes, was related to the hubs central point. This point was then moved, and with it the hub section as a rigid element, 60 mm downwards onto the contact plane which had been fixed in all directions. The material properties, frictional coefficient and step size were the same as used before. The question here was to find the bending behaviour of such low-curved strips and to foresee problems before setting up a full model.

The results can be seen in Figures 4.11 to 4.14. The crossed blade set (Figures 4.11 and 4.12), shows that the blades indeed lean against the hub as predicted. Interestingly, this independent from the end curve. The second set (Figures 4.13 and 4.14), shows an effect of the end curve. If curved inwards, the blade will bend inwards and lean against the hub. In the second case, where the end curve is outwards, the blades will tend to deform outwards. Such an outward bending is preferable compared to an inward bending, as this could interfere with other connection points on the hub of other spoke elements. In addition, the last model (Figures 4.14) is also the stiffest providing the highest resistance to the deformation, which can be seen in the relative smooth bending curvature and the low stress level. The following table lists the maximal stress levels for all models (Table 4.3).

Table 4.3: Summary of the single spoke bending test. The results show that a spoke element with two blades sharing a connection interface at the ring and an outwards curved end will achieve the lowest stress level and highest resistance to the applied force.

Model	Shared Connection	End Curve	Max. Stress (v.Mises) [N/mm] ²	Applied Force [N]
1	N	in	180	126
2	N	out	200	148
3	Y	in	250	71
4	Y	out	116	176

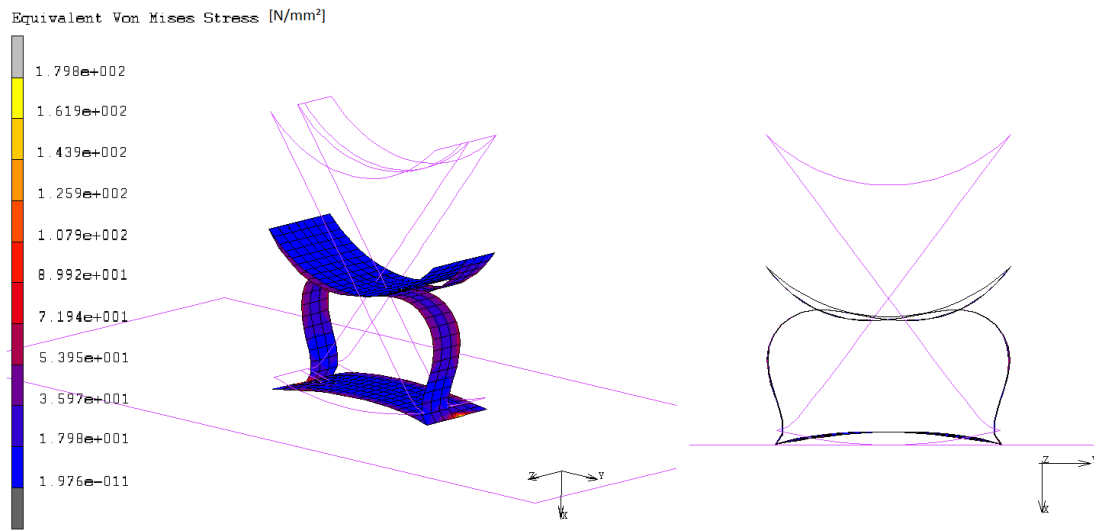


Figure 4.11: Single spoke analysis with two blades crossing and an "inwards" ring-end-curve, placed between the hub (top) and the ring (bottom). Left: Perspective projection of the spoke assembly showing the distribution of the equivalent tensile stress (von Mises). Right: Projection in the xy-plane showing the initial undeformed state and the deflection when moving the hub halfway (60 mm) in positive x-direction.

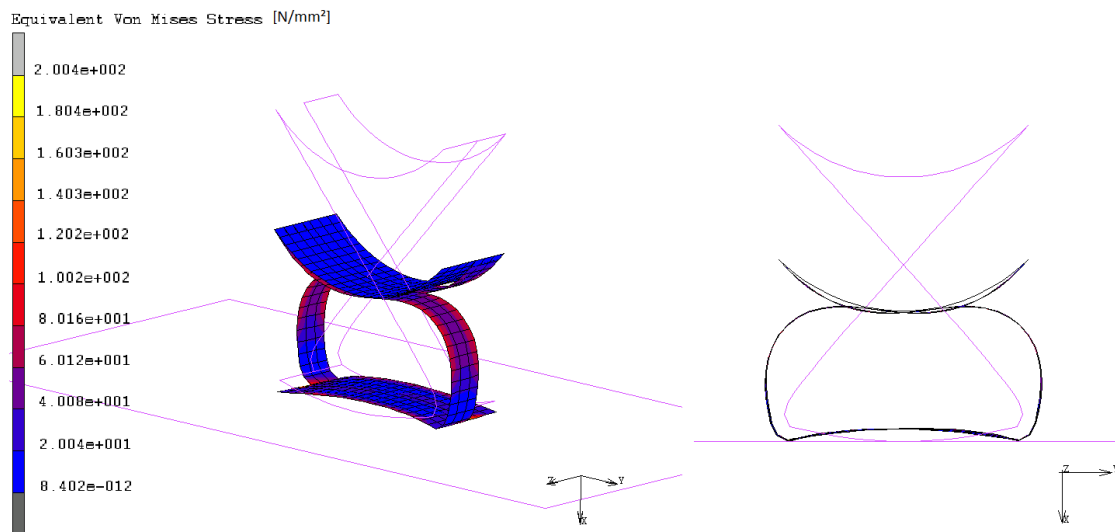


Figure 4.12: Single spoke analysis with two blades crossing and an "outwards" ring-end-curve, placed between the hub (top) and the ring (bottom). Left: Perspective projection of the spoke assembly showing the distribution of the equivalent tensile stress (von Mises). Right: Projection in the xy-plane showing the initial undeformed state and the deflection when moving the hub halfway (60 mm) in positive x-direction.

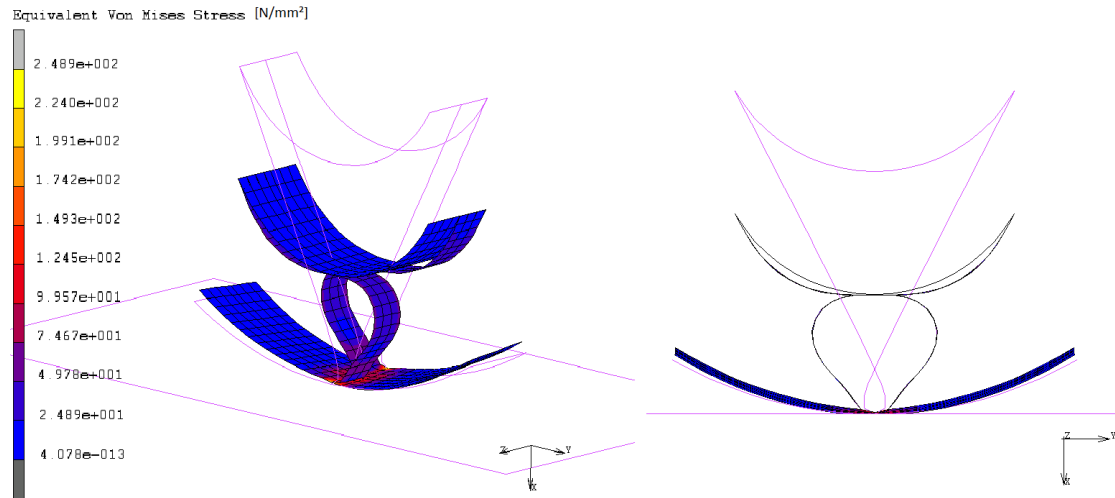


Figure 4.13: Single spoke analysis with two blades placed between the hub (top) and the ring (bottom), sharing a line of connection at the ring and an "inwards" ring-end-curve. Left: Perspective projection of the spoke assembly showing the distribution of the equivalent tensile stress (von Mises). Right: Projection in the xy-plane showing the initial undeformed state and the deflection when moving the hub halfway (60 mm) in positive x-direction.

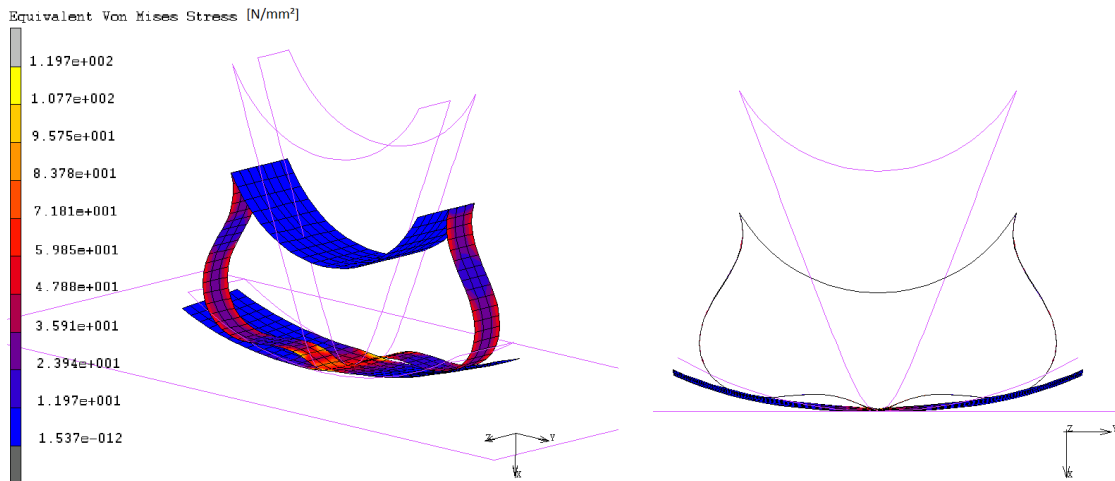


Figure 4.14: Single spoke analysis with two blades placed between the hub (top) and the ring (bottom), sharing a line of connection at the ring and an "outwards" ring-end-curve. Left: Perspective projection of the spoke assembly showing the distribution of the equivalent tensile stress (von Mises). Right: Projection in the xy-plane showing the initial undeformed state and the deflection when moving the hub halfway (60 mm) in positive x-direction.

Full Wheel Analysis

The previous analysis showed how the blades would deform depending on their connection type and end-curve geometry. The best performance was achieved with model 4 (refer to Figure 4.14), which was characterised by the lowest stress value and the highest stiffness. This was due to the outward bending of the blades, which allowed the load to be spread over a wider area as the bent blades pushed the ring segment back against the ground. To see how such a geometry would react when implemented in a wheel system, the next FE model was set up again as a full wheel model. In order to create a very harmonic wheel, where the stiffness does not change much along one full turn, the blades were attached to 12 points equally rotated with a shift of 30° around the circumference and mirrored in the xy-plane. As mentioned earlier, a pair of two blades builds a spoke sharing one line of connection on the ring. This results in a total number of 48 blades, 24 spokes with 12 spokes on either side of the wheel.

A special feature in this model are the included grousers. Recalling Figures 2.11 and 3.1, grousers are attached around the wheels circumference in order to improve traction. Their secondary effect is that they also work as stringers, which stiffen the wheel preventing the ring from bending around the x-axis. In the shear plate model (refer to Figure 4.7), grousers were not included. As a result, the ring is pulled inwards at the connections. In the new model presented here, this would, however, imply a relative torsion of the blades sharing a connection on the ring. The outer blade would be pulled inward, whereas the inner blade would be pulled outward (increased shear stresses at corner points). The grousers were added by defining a thin section spanning the width of the ring, which were then assigned with quad elements of higher thickness $t_{grouser} = 3 \text{ mm}$ (Figure 4.16). The results of this analysis with a wheel deflection of 40 mm can be seen in Figure 4.15.

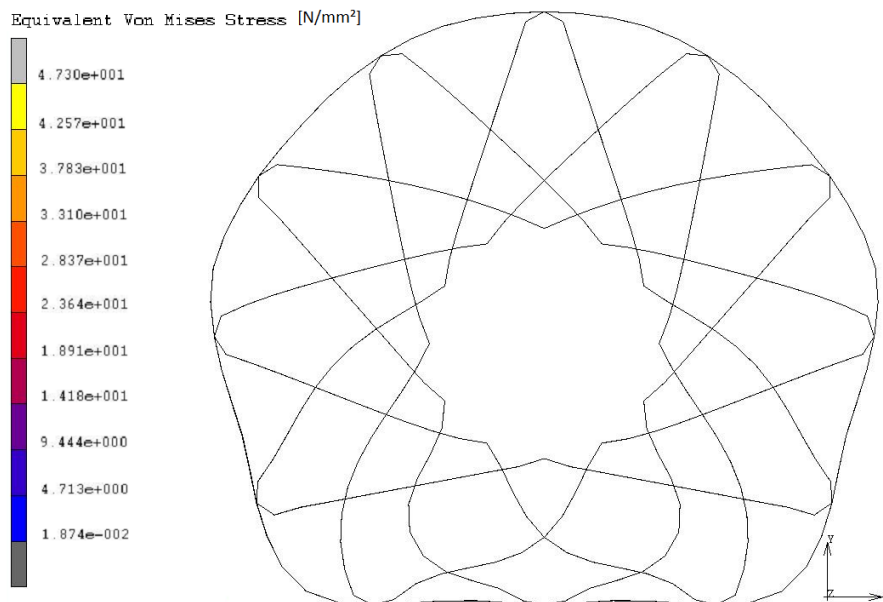


Figure 4.15: Full wheel analysis of the tension blade variant A, where the blades have a curved end at the ring connection. Note the multi-curve shape of the ring as it gets pulled inwards by the lower left and right fully stretched tension blades.

Design Revision

The maximal stress along the 40 mm deflection progress reached approximately 50 N/mm^2 . This is significantly lower compared to the high shear stress values from the previous concept (990 N/mm^2 , refer again to Figure 4.7). The draw back in this model is, that the blades when fully tensioned pull the ring inwards resulting in a deformed shape. This may well effect the rolling capabilities of the wheel, as the multi-curved ring would be carried along in the form of a standing wave when driving.

The simulation with the second GCP (point between two spokes) did also show a stability problem of some for the blades (due to instable buckling). As was explained already in the single spoke test, the deformation at GCP 2 deformed the blades in the opposite direction. This is of course undesirable, as for the operation the blades would be required to bend all in the same direction (e.g. outwards). The curved-end variant does therefore seem insufficient to support such an equalised deformation behaviour. To overcome this problem, as well as the aforementioned multi-curved ring deformation, one can increase the curvature of the blades so that they not only have a curved end but a gradually curved shape along their full length.

4.4.2 Variant B - Near-Parabolic Curved

Learning from the previous simulations, a final model was created in order to reduce multi-curved ring deformation and to ensure a uniform outwards bending of the spokes. For this purpose, the blade configuration from variant A was maintained, whereas only the geometry of the blades was changed to that of a near-parabolic curved (NPC) shape (Figure 4.16 Left).

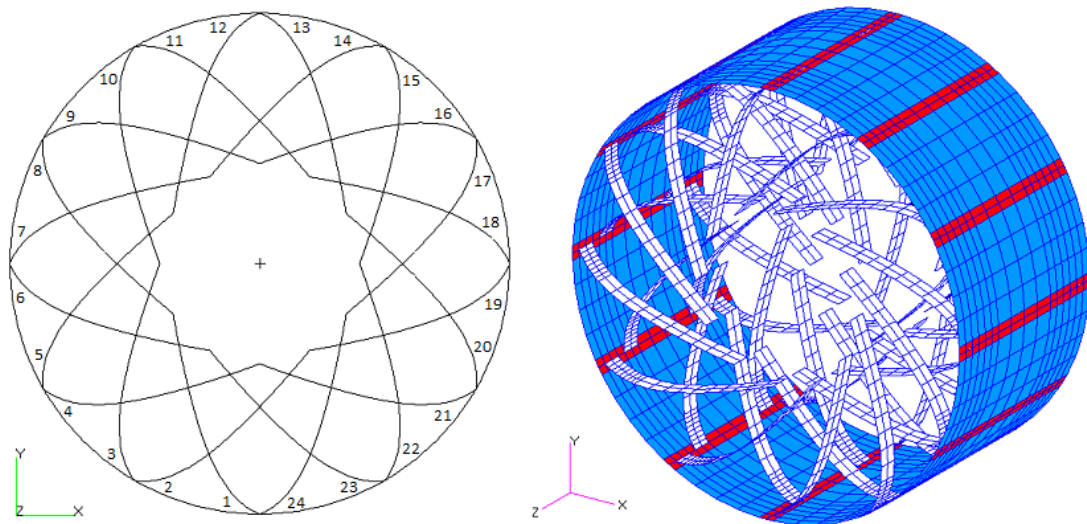


Figure 4.16: Tension blades variant B. Left: View in the xy-plane showing the near-parabolic curved blades. The blades were numbered from 1 to 24, beginning on the left blade from the lower centre, running clockwise around the ring. Their mirrored counterparts (not visible in this plane) received a prime suffix ('). Right: Perspective view on the undeformed tension blade wheel showing the different assigned thicknesses of the FE elements ($t_{\text{blades}} = 0.3 \text{ mm}$, $t_{\text{ring}} = 0.5 \text{ mm}$, $t_{\text{grouser}} = 3 \text{ mm}$).

This model prior to the simulation can be seen in Figure 4.16 Right. Note here the different levels of section thicknesses.

- Blade thickness $t_{blades} = 0.3 \text{ mm}$
- Ring thickness $t_{ring} = 0.5 \text{ mm}$
- Grouser thickness $t_{grouser} = 3 \text{ mm}$

As an additional feature, a bump stop was included to simulate a situation where the deformation reaches a defined limit and to obtain an estimate of how the pressure to the ground would change. This bump stop ring had a diameter of 300 mm, a width of 80 mm and was placed to fit between the inner blades. The diameter allowed for a maximum deflection for the ring of 50 mm.

Load Case 1 - Wheel Load

The first load case was simulated with the second method of defining the BC's (refer to section 4.3.3) by fixing the contact surface and relating the geometrical centre to the hub supports. In doing so it was possible to define a single load at the centre point which was then transferred outwards. The net effect is that the set load is equally distributed onto the hub nodes which then behave as a combined solid object.

Figures 4.19 and 4.20 show the deformed wheel when reaching the included stop (which also moved in relation to the centre point). It can be seen that due to the increased curvature of the blades the ring does not get pulled inwards as strongly as in the previous end-curved case (see again Figure 4.15) and remains a relatively harmonic oval shape. It can also be noted from these figures, that an even and flat ground contact occurs, which would imply a large contact surface and therefore a high tractive effort when rolling on soft soils (see again Equation 2.6).

For a detailed explanation, the blades were numbered from 1 to 24, beginning on the left blade from the lower centre, running clockwise around the ring (refer again to Figure 4.16 Left). Their mirrored counterparts receive a prime suffix ('). The blades taking most of the load at the final deformed state are the blades # 4, 4' and # 21, 21'. But some part of the load is also carried by the blades which are also in tension (blades # 6, 8, 10, 12, 13, 15, 17, 19 and their prime counterparts). Thanks to this, the load on the bent bottom blades is reduced significantly.

In Figure 4.17 the resulting force onto the ground is plotted over the deflection distance. At low deflections the load onto the wheel is taken via compression of the bottom blades as the slope increases gradually from point 0 to point 1. After this, the slope angle increases mildly indicating a transition phase, where some of the other spokes begin to carry some part of the load. At point 2, the blades at the side and above the hub have now fully stretched balancing their initial curvature. As a result, they begin to take over and become the primary load carrying mechanism. The resistance to the applied force is now much higher, because almost the whole structure is involved in working against it. The only exception are blades # 5, 7, 9, 11, 14, 16, 18 and their counterparts on the other side, which are bent upwards. The ring, just like a bicycle rim, holds the tensioned blades together transferring the force through it down to the ground.

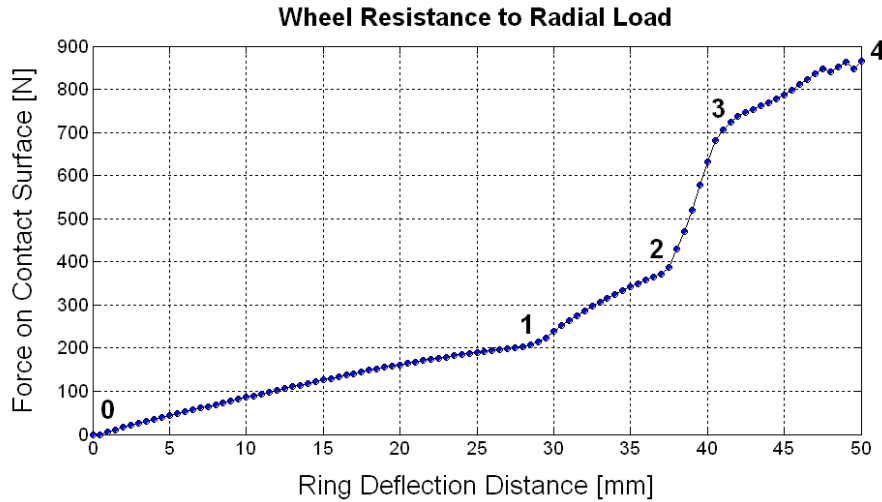


Figure 4.17: Resistance of the wheel when loaded in radial direction. The resulting force onto the ground provides information of how the blades contribute in the load carrying process (compare with Figures 4.19 and 4.20). Point 0 to 1, compression of the bottom blades. Point 1 to 2, transition to tension of the upper blades. Point 2 to 3, the side and upper blades take all the load via tension. Point 3 to 4, slope flattens out marginally due to a slight upwards shift of the ring at the bottom centre. Point 4, contact with included bump stop.

In terms of structural volume ($V_{ring} + V_{blades}$) and subtracting the upwards bent blades, approximately 85% of the wheel structure now takes part in the load carrying process. Based on this, the wheel can now be characterised as a top loader.

From point 2 to 3, the force increases strongly and the wheel deforms only minimally as the tension in the blades increases steadily with the applied load. The slope of the curve flattens out marginally from point 3 to 4, as the ring bends slightly upwards locally at the bottom centre and lifts itself from the contact surface. This occurs because the set friction permits that the material is pushed inwards. Finally, at point 4 the included bump stop makes contact with the ground and the applied force is transmitted through it directly. The load onto the wheel at 40 mm deflection is about 640 N, which matches the requirements of 600 N for each of the four RIMRES wheels. Throughout the deformation process, stresses in the members did not exceed a value higher than 100 N/mm² (von Mises).

Load Case 2 - Torque

For the second load case, the deformation in the negative Y-direction was combined with a torque along the positive Z-axis (Figure 4.21). As explained above, the BC's permit the movement of the hub supports but in order to have the wheel react to this torque, the centre bottom line of nodes spanning across the full width of the ring was translationally fixed in X and Y, permitting only side slipping. The real world scenario would be a so called "step down/up" manoeuvre, where the rover attempts to climb a rock and only a single grouser clings to this obstacle forcing the wheel upwards. The wheel was deflected to 40 mm and then subjected to a torque of 127 Nm (counterclockwise).

In Figure 4.22 it can be seen that the peak torque forces the blades to pull the ring inwards. Due to this, the tension in the blades which have stretched by the deflection does not increase much and the stress level stays below 100 N/mm^2 . From this, it can also be seen that the torque load is distributed on the blades which are already in tension. It should be noted that this deformed state is only due to the momentary peak torque of the drive unit at a collision. The ring retains its radially deformed shape at normal driving torques ($T_N = 33 \text{ Nm}$)

Load Case 3 - Side Skid

The last load case, simulating driving along the side of a slope, was also combined with the radial deflection. The side skid force component at an angle of 30° ($F_s = 300 \text{ N}$) was applied at the rotationally centre of the wheel in positive Z-direction. To avoid slipping this time, the centre bottom line of nodes was restrained in the Z-direction also.

Looking at Figure 4.24, one can see that the side force produces a bending moment trying to rotate the blades. Because the blades have a high second moment of area in this direction, they develop regions of compressive stress and tensile stress along the neutral axis which increase linearly with distance away from it (Figure 4.18). This can be seen at the highest stress levels at the diagonal opposite blade corners.

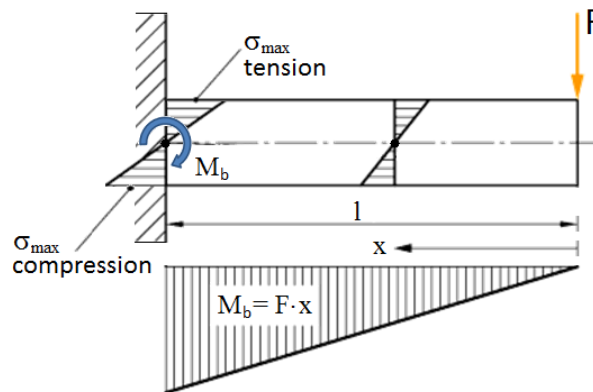


Figure 4.18: Engineering beam theory of a cantilever beam. Part of the beam is in tension, and the other is in compression, passing through a zero value at the neutral axis. The distance between the tensile and compressive regions determine the bending moment M_b . The maximal stress level occurs at the fixed end [46] [47].

Interesting in this result is that the blades also twist (Figure 4.23). Due to the fact that the blades are not straight but curved, the side force not only produces the bending moment described above but also a torsional moment around the blades longitudinal axis. This torsional moment produces an additional shear stress which superimposes with the bending normal stress. Because in this load case a force is applied in addition to the radial deformation it is unsurprising that the stress level here are higher than in load cases 1 and 2. The von Mises stress level reaches a maximum of 260 N/mm^2 which is still a factor of 1.5 (incl. FS) below the defined yield limit. It can therefore be argued that the wheel has sufficient side stability. An attempt to derive and verify the resulting stress level using a linear static approach can be found in Appendix A.

Ground Contact Points

Finally, we compare the deformation behaviour of the different ground contact points (GCP). Due to this new design, there are only two different types instead of the three for the ExoMars wheel. Figures 4.25 and 4.26 show the 40 mm deflection of GCP 1 (direct spoke contact) and GCP 2 (contact between two spokes), respectively. Here can be seen that in both cases the blades bend outwards which, as explained earlier, is most important to prevent buckling and ensure a smooth driving operation.

GCP 1 produces a long and flat base with 3 grousers making contact with the ground, whilst distributing the wheel load evenly over the whole surface. At GCP 2 on the other hand, only two grousers make contact with the ground and the ring lifts slightly upwards. The wheel load will therefore be locally increased at these supports. GCP 2 also has a slightly higher stiffness. If the wheel is loaded with the designed wheel load of 600 N, GCP 2 will deform ≈ 3 mm less than GCP 1, which is round 7.5% for the 40 mm deflection average. Recalling the low driving speed of the rover (≤ 100 m/h), this will not be critical as one can assume that no bouncing motion will develop.

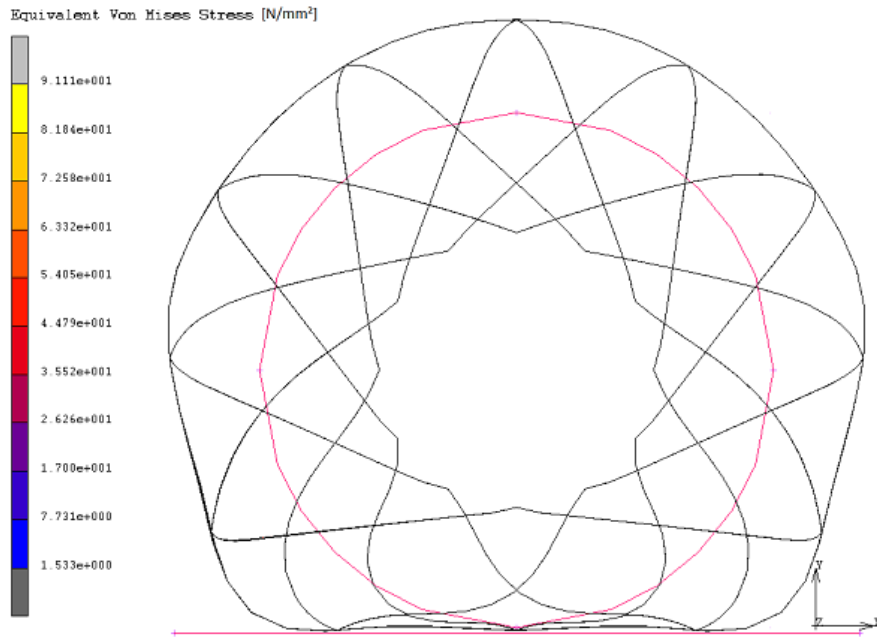


Figure 4.19: Tension blades variant B: Full wheel analysis load case 1 (xy-plane). The load was applied at the centre of the wheel in negative Y-direction, pressing the ring down to the contact surface until the included bump stop was reached at 50 mm deflection.

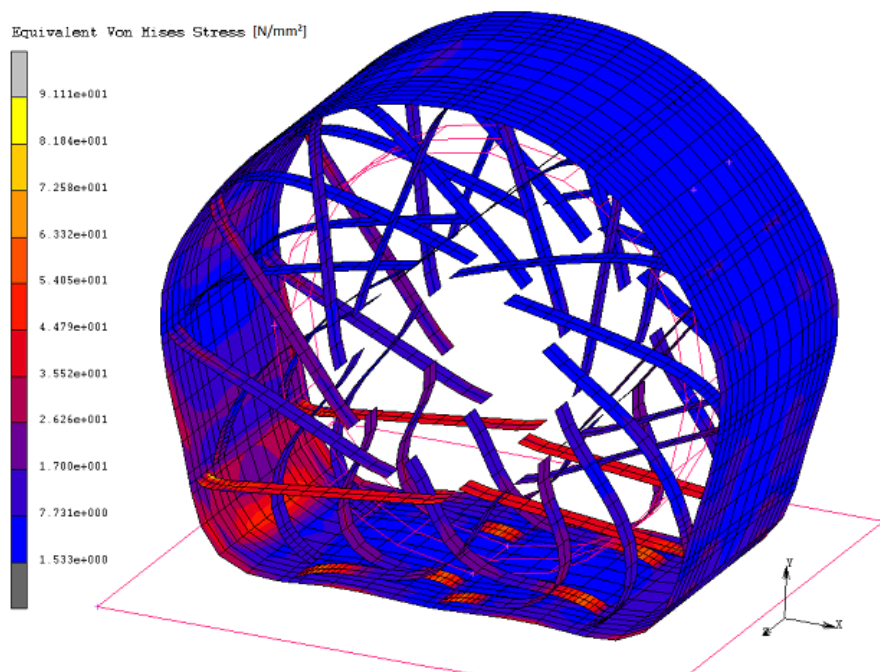


Figure 4.20: Tension blades variant B: Full wheel analysis load case 1 (perspective view). The load was applied at the centre of the wheel in negative Y-direction, pressing the ring down to the contact surface until the included bump stop was reached at 50 mm deflection.

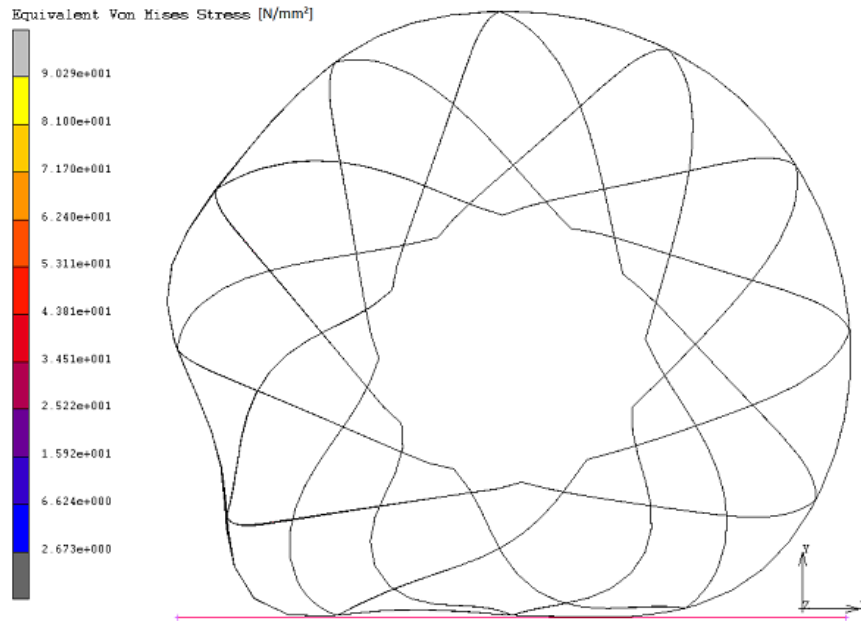


Figure 4.21: Tension blades variant B: Full wheel analysis load case 2 (xy-plane). The wheel was deflected to 40 mm and then subjected to a torque of 127 Nm. The bottom centre of the ring was restrained allowing to apply the torque (counterclockwise) at the wheels centre.

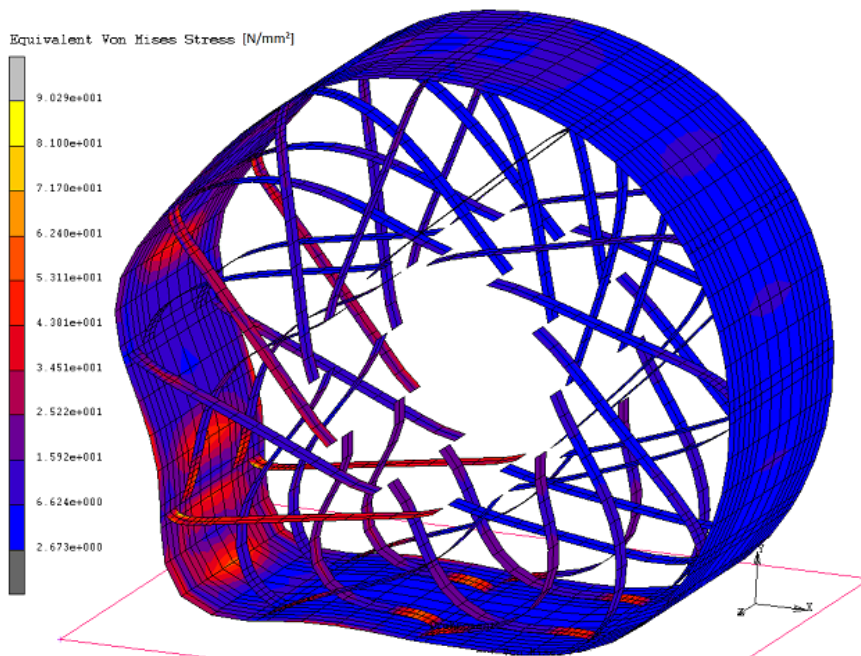


Figure 4.22: Tension blades variant B: Full wheel analysis load case 2 (perspective view). The wheel was deflected to 40 mm and then subjected to a torque of 127 Nm. The bottom centre of the ring was restrained allowing to apply the torque (counterclockwise) at the wheels centre.

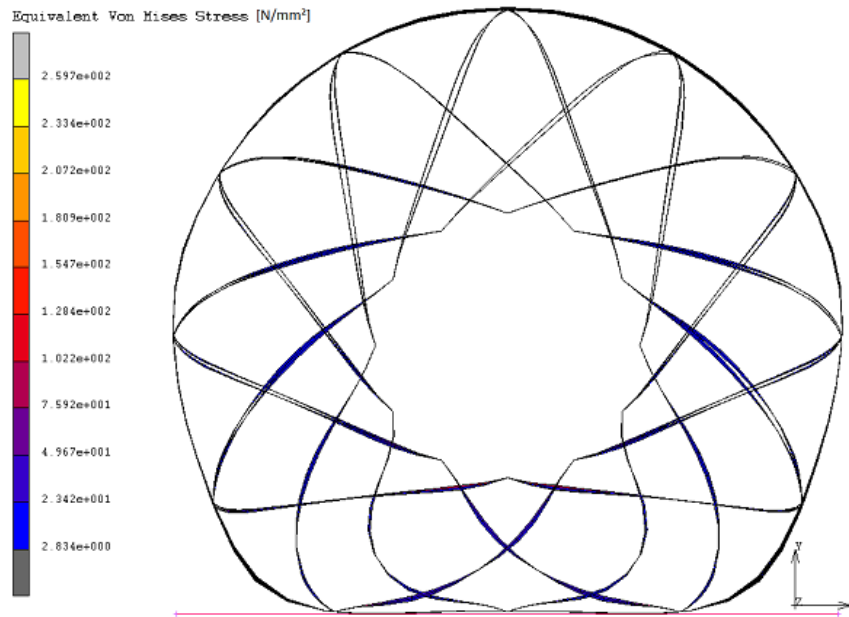


Figure 4.23: Tension blades variant B: Full wheel analysis load case 3 (xy-plane). The wheel was deflected to 40 mm and then subjected to a side skid force of 300 N. The bottom centre of the ring was restrained allowing to apply the side skid force (in positive Z-direction) at the wheels centre.

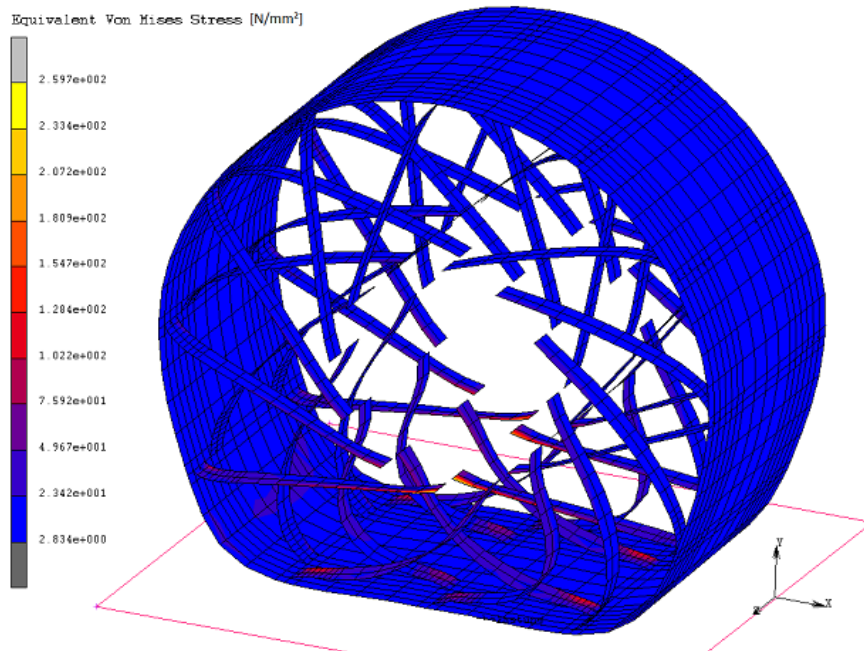


Figure 4.24: Tension blades variant B: Full wheel analysis load case 3 (perspective view). The wheel was deflected to 40 mm and then subjected to a side skid force of 300 N. The bottom centre of the ring was restrained allowing to apply the side skid force (in positive Z-direction) at the wheels centre.

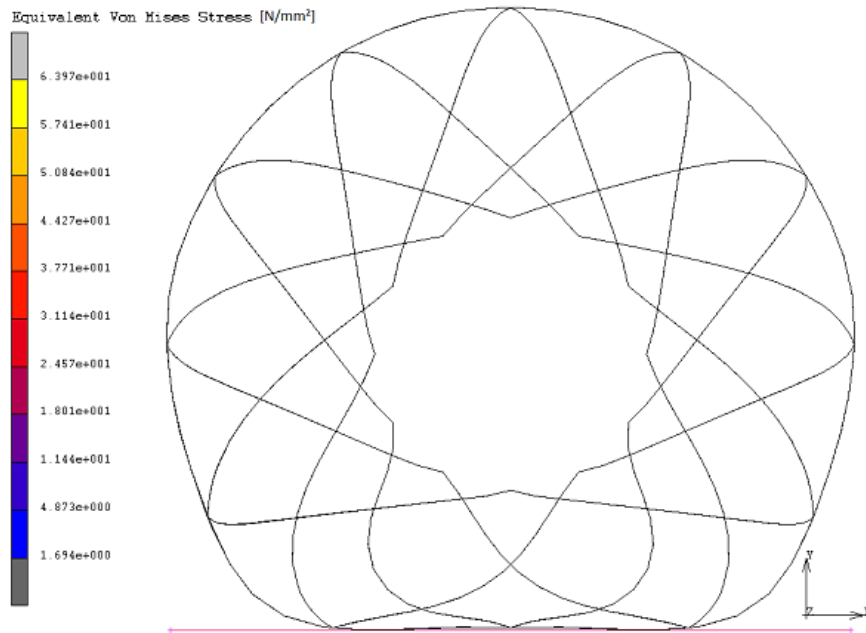


Figure 4.25: Tension blades variant B: full wheel analysis GCP-1. The wheel was subjected to the designed wheel load of 600 N, to allow the evaluation of the deflection behaviour for the two different ground contact points. Compare with Figure 4.26.

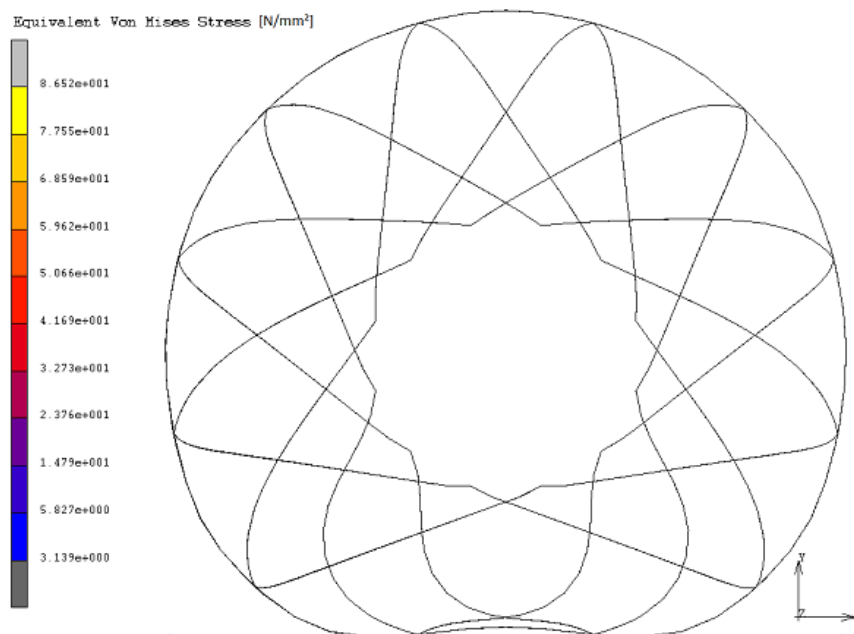


Figure 4.26: Tension blades variant B: full wheel analysis GCP-2. The wheel was subjected to the designed wheel load of 600 N, to allow the evaluation of the deflection behaviour for the two different ground contact points. Compare with Figure 4.25.

Part III

CONCLUSIONS

5

RESULTS

The previous investigated concepts to adapt the baseline wheels stiffness have been analysed in detail leading to a better understanding of their working principles. Additionally, the experimental analyses of concepts 2 and 3 have disproved the previous proclaimed functionality. Recollection of the plastic deformation problem of the baseline wheel design, including the unfavourable arrangement of the waved metal bands for concept 1, concluded that the baseline wheel is not suited for the intention to develop a flexible metal wheel with adjustable capabilities.

Based on the experiments performed, a new wheel design was proposed using a shear panel concept, able to accommodate an electromechanical wheel stiffening system. With the help of a computer based finite element analysis the non-linear deformation of the flexible elements could be investigated. The first analysis identified a weakness in the spokes shear deformation behaviour. Looking in detail into the displacements found by the simulation, the problem could be verified with simplified hand calculations and by analysis of the materials properties. In summary, forcing the shear plate to make a specific displacement develops excessive shear stresses which will cause the elements to deform permanently.

With these lessons learned, a second design was proposed based on the tensioned spoke wheel (bicycle wheel) in order to overcome the previously identified shear deformation problem. The new idea with curved blades was then analysed, leading to a design which permits large deflections $\geq 10\%$ of the wheels diameter and with low stress levels by maintaining a relative harmonic oval shape. In addition, it could also be shown that the new design could sustain loads of high torque and side skid. In each load case the wheel deformation behaviour was analysed and cross checked from a structural mechanics point of view. The results found with the simulation, which achieved the best performance in terms of deflection distance and applied load, were then used to design and construct a new breadboard demonstrator wheel. A final CAD-model is presented in Appendix B.

It should be noted, that for this first design the curvature of the shaped blades was not fully defined. Accordingly, the blades in the established CAD model may well have a slightly different shape. It is therefore possible that the manufactured blades behave differently to those in the simulation. This needs to be tested with the new breadboard demonstrator wheel. Care should also be taken with the selection of the material. The concept proposed herein for the flexible elements is designed for high strength spring steel of reasonable quality having a thickness between 0.3 to 0.5 mm and a yield limit of no less than 500 N/mm². This value may be able to be reduced when the tests of the breadboard demonstrator confirm the values found in the simulations.

The achieved results and the work of this thesis have been presented at the Institute and written down in the form of a "trade-off document" [35] and a "detailed mechanical design document" [28]. With respect to the defined objectives by DLR, it can therefore be said that the undertaken project, to develop and to design a flexible metal wheel with an adaptive mechanism for soft planetary soils, has been fulfilled with complete satisfaction.

6

DISCUSSIONS

In this thesis, the principle and necessity of flexible wheels used for off-road vehicles has been studied. In particular the difference between the wheel soil interactions for hard and soft ground conditions, stated in the literature review, have shown that a carefully designed wheel concept for a given or expected ground condition can achieve great advantages in terms of energy efficiency and the ability to cope with rough and difficult terrains. The focus here was on the development of systems for planetary surface operations beyond the Earth. The advantages of a rolling mobility system has been presented, as well as the expected improvements in motion performance of an adaptable system able to adjust its state to current conditions.

The previously investigated concepts for such an adaptable system have been assessed and revised, which has helped to identify the requirements for the design process. Based on the revisions, which included obtaining data through laboratory experiments, a new design was proposed and analysed. The requirement for a new design concept was justified by showing that the former design concepts did not comply with the defined requirements. Using the experience gained with the baseline wheel and utilising FE simulations, the new design was refined to improve the flexible performance, in order to sustain higher loads whilst at the same time accounting for the desired stiffening system. This was possible by incorporating an innovative load carrying mechanism.

It must be noted, that although the presented design takes a future stiffening system into consideration, the focus on such a mechanism should be on the implementation and the ability to tolerate the flexible deformation of the wheel. The problem experienced with the shear panel design and the identified cause due to the relative shift of the hub and ring has shown, that radially implemented stiffeners would encounter the same shearing problem. This relative shift will not only be present at the sides of the hub but also beneath it at the contact point to the ground. When the ring is pressed to the surface at a point between two stiffening elements, the downwards movement of the hub will produce a moment trying to rotate the elements. For this reason, the supports of the stiffening mechanism need to be carefully investigated, in order to decouple them from the hub and ring, and consequently avoid shearing. This could be achieved by a dedicated joint, which would then balance the relative shift of the hub.

In order to refine the presented tension blade concept for the current project, or to utilise the design to different rover missions in the future, the key variables (design factors) should be mentioned. These are,

- The size of the hub,
- The blade and ring thickness,
- The position and number of the blades, and
- The length and curvature of the blades.

Resizing the hub can be used to either make the design stiffer or more flexible. When the interface points of one spoke element (two blades forming the NPC arc) on the hub are maintained at 120° , then an increase in the hub's diameter will make the wheel more flexible. As was presented earlier, when the supports are taken further apart with respect to each other, the flexibility of the spoke increases (refer to section 3.3.3).

The thickness of the blades and the ring is also a vital factor in terms of the wheel's flexibility. Especially when the thickness of the ring is increased, the deflection is reduced as the resistance to the deformation load is raised. Additionally, the circular shape of the wheel could be maintained for higher loads. This can be used to avoid a multi-curved ring due to the inwards pulling force of the tension blades. The resulting stress levels of the blades at the connection points, however, are then required to be investigated carefully.

The number and positioning of the blades has been designed in order to achieve a highly harmonic wheel where the stiffness, and therefore the deflection, does not change significantly through a wheel's turn. This is important for the overall efficiency, as every change would increase the rolling resistance. The baseline wheel implied 3 different ground contact points (GCP) with varying stiffness values through a turn of 120° . The new design has only 2 different GCP's with varying stiffness through a 30° turn. The net effect is a more even deflection performance and therefore a lower resistance to motion.

The most critical point of this design is the shape of the curved blades. The curvature has not been fully defined and therefore may lead to differences to the predicted performance. The curvature is required to be high enough in order to prevent unstable buckling and not to deform the ring unnecessarily even at high deflections. On the other hand, the curved length should not exceed a certain amount in order to maintain the principle of a "top loader" when deflected. The spoke curvature of the baseline wheel for example, does not permit the upper spokes to stretch enough in order to take on the load via tension.

Although it is predicted that the tension blade design will improve the baseline wheel's deflection and load carrying ability, the drawbacks of this design should also be stated. The pro and contra arguments are presented in Table 6.1.

Table 6.1: Advantages and Disadvantages of the proposed tension blade wheel concept compared to the ExoMars baseline wheel.

Pros	Cons
<ul style="list-style-type: none">• Large deflection and large contact surface• Only 2 different GCP's evenly distributed by 30°• High load carrying capability and no critical curvature radius when deformed• Increased ability to take high torques due to distrib. on all blades in tension• All blades have the same form, good for manufacture	<ul style="list-style-type: none">• Lower side skid stability• Higher mass, More elements, More connection points• Oval shape of ring requires careful design

On a side note, drawing upon the results obtained, a new name was proposed for the DLR RIMRES wheel. For the reason that this new design concept is not limited to the RIMRES project and may be used on a different type of rover or another future mobility system, it can be regarded as a system on its own. For later identification purposes it is therefore proposed to term this type of concept the "DLR INFLATE wheel".

Following the concept of an adjustable wheel, like an inflatable rubber tyre, the INFLATE wheel adjusts its stiffness via an electro-mechanical system. The effect of increasing or decreasing the ground contact area is the same as for an inflatable tyre. Secondly, INFLATE is also an acronym identifying the wheel as a system - INtelligent FLexible Adaptive TEnsion-blades (INFLATE). This incorporates the intelligent sensor concept, which will be used to determine the present ground properties during operation on which basis the flexible wheel can then be adjusted using the included stiffening system.

7

CONCLUSION

To draw upon the results and discussions presented above, the achievements of this thesis can be summarised in three points.

1. To clarify that the previous investigated concepts do not fulfill the requirements.
2. To perform a FEA and not to rely on hand calculations and simple bending test only.
3. To include tension blades based on the bicycle load carrying principle.

The first achievement, though obvious, may be in fact the point with the highest importance. The previous work has been examined and critically analysed, revealing major discrepancies in the results given earlier. The test data accumulated and used for the previous analysis was not processed according to the recommended procedure, resulting in false values. The test setup itself did not comply with the underlying principle of the devised concepts leading to misinterpretations and wrong assumptions. Clarifying these issues and revising the concepts led to the decision not to pursue the solutions presented earlier but to develop a new and more elaborate concept.

The decision to perform a computer based finite element analysis helped to clarify the working principle of the new concept. Only with the use of a relative quick simulation, in order to analyse the full systems behaviour, could the actual stress problems be identified in the given time frame. Though the first new concept was more sophisticated than the previous concepts, it also revealed a major weakness. The anticipated bending problem turned out to be non-critical, however, the developing shear strain produced stresses above the materials yield limit.

The third achievement was to use the information obtained from the FEA, combine it with the well known tensioned spoke principle and to develop a working concept for the new design, which

- Does not induce the shear strain problem,
- Enables high deflections $\geq 10\%$ of the wheels diameter,
- Improves the load carrying performance of the baseline wheel, and
- Provides enough room for the envisaged stiffening system.

The work presented here provides a good basis for the DLR wheel development in the RIMRES project. However, as with every new design, the assumptions and calculations made may work in theory, but until tested in real life have no practical purpose. The simulations performed attempt to estimate, as best as possible, the wheel behaviour in certain situations. However, on the whole they remain estimates. The results presented here, though looking very promising, require verification in a real world test setup. It is therefore recommended to perform extensive testing on the DLR Landing and Mobility Test-facility. The new developed and specifically for this test facility designed Single Wheel Test-rig needs to be initiated and tested in order to achieve accurate test data, which can be reproduced and to make reliable conclusions of the INFLATE wheels performance.

Summarising the project and the work of this thesis in one statement. The findings were used to design and construct a new breadboard demonstrator wheel, which when tested successfully, will be part of a complete wheel set for the RIMRES rover. With this new concept, pioneering new rover mission scenarios on varying soil surfaces as can be expected to be encountered on the Moon and other planetary bodies, can be undertaken. Consequently, the DLR wheel development has made a full turn forward.

REFERENCES

- [1] M.G. Bekker, *Theory of Land Locomotion - The Mechanics of Vehicle Mobility*. The University of Michigan Press in Ann Arbor, 2nd ed., 1962.
- [2] A. Seeni, B. Schäfer, and G. Hirzinger, “Robot Mobility Systems for Planetary Surface Exploration - state-of-the-art and future outlook: A literature survey,” in *Aerospace Technologies Advancements*, p. 492, January 2010.
- [3] B. Leitenberger, “Das Luna Programm - Fahrzeuge auf den Mond (Luna 17, 21).” www.bernd-leitenberger.de/luna.shtml, accessed on May 16, 2011.
- [4] L. Richter, “Exomars Rover Chassis & Locomotion Phase B1 - Wheel Concept Trade-off,” Tech. Rep. EXM.RM.TNO.DLRRY.0001, DLR - German Aerospace Centre, January 2008.
- [5] A. Kemurdjian et al, “Design Features of Planet-rover Assemblies and Systems,” in *Kemurdjian et al, Planetokhodyi. Machinostrojenie*, 1993.
- [6] Goodyear, “MET Project - Modular Equipment Transporter Tires,” Tech. Rep. issue 1, Goodyear Tire & Rubber Company, Technical Center, Akron, OH., year unknown.
- [7] V. Asnani, D. Delap, and C. Creager, “The Development of Wheels for the Lunar Roving Vehicle,” *Journal of Terramechanics* 46, pp. 98–103, 2009.
- [8] J. Matijevic, “Sojourner - The Mars Pathfinder Microrover Flight Experiment,” *Jet Propulsion Laboratory - California Institut of Technology, Pasadena, CA*, 1997.
- [9] A. Eisen et al, “Mechanical Design of the Mars Pathfinder Mission,” *Proceedings of the 7th European Space Mechanisms & Tribology Symposium*, ESA ESTEC, Noordwijk, The Netherlands, 1997.
- [10] JPL Caltec, “Mars Exploration Rover Mission - Update: Spirit and Opportunity.” <http://marsrovers.jpl.nasa.gov/mission/status.html>, accessed on May 18, 2011.
- [11] R. Lindeman and C. Voorhees, “Mars Exploration Rover Mobility Assembly Design, Test and Performance,” *Jet Propulsion Laboratory - California Institut of Technology, Pasadena, CA*, 2005.
- [12] JPL Caltec, “Mars Science Laboratory - NASA’s next Mars Rover.” <http://marsprogram.jpl.nasa.gov/msl/mission/rover>, accessed on May 16, 2011.
- [13] JPL Caltec, “Building Curiosity Update - Video: Rover Rocks Rocker Boggie - 09.06.10.” http://www.nasa.gov/mission_pages/msl/building_curiosity.html, accessed on May 16, 2011.
- [14] ESA, “Robotic Exploration of Mars - The ESA-NASA ExoMars programme 2016-2018.” <http://exploration.esa.int/science-e/www/object/index.cfm?fobjectid=46048>, accessed on April 8, 2011.

-
- [15] L. Waugh et al, "Locomotion Field Trials for a Mars Rover Testbed," *9th ESA Workshop on Advanced Space Technologies for Robotic and Automation (ASTRA) at ESA ESTEC, Noordwijk, The Netherlands*, November 2006.
- [16] L. Richter and S. Weiß, "Exomars Rover Chassis & Locomotion Phase B1 - Breadboard Wheel Detailed Design Document," Tech. Rep. EXM.RM.TNO.DLRRY.0003, DLR - German Aerospace Centre, April 2008.
- [17] J.Y. Wong, *Theory of Ground Vehicles*. John Wiley & Sons, Inc., 2nd ed., 1993.
- [18] Functionbay Inc., "Soil Tire Force Formula, in recurdyn help library." http://www.kxcad.net/RecurDyn/RecurDyn_Ver6.3/index.htm, accessed on May 23, 2011.
- [19] A. Gibbesch, B. Schäfer, and S. Michaud, "3D Simulation and Validation of RCL-E and MER Rover Types Mobility," *9th ESA Workshop on Advanced Space Technologies for Robotic and Automation (ASTRA) at ESA ESTEC, Noordwijk, The Netherlands*, November 2006.
- [20] M. Scharringhausen et al, "A Wheel-Soil Interaction Model for Planetary Application," *11th European Regional Conference of the International Society for Terrain-Vehicle Systems (ISTVS), Bremen, Germany*, October 2009.
- [21] GM-DRL, "Lunar Wheel and Drive Experimental Test Program," *Summary Technical Report, NASA TR67-18*, vol. 1, June 1967.
- [22] J. Meraldi and A. Delfino, "The Michelin Lunar Wheel." Internal presentation at DLR, Michelin Recherche Technique, Switzerland, May 2009.
- [23] F. Cordes and F. Kirchner, "Heterogeneous Robotic Teams for Exploration of Steep Crater Environments," *International Conference on Robotics and Automation (ICRA), Anchorage, Alaska*, May 2010.
- [24] L. Richter, M. Scharringhausen, and S. Weiß, "Exomars Rover Wheel Preliminary Definition & Performance Prediction," Tech. Rep. EXM.RM.TNO.DLRRY.0002, DLR - German Aerospace Centre, September 2007.
- [25] S. Michaud and B. Despont, "ExoMars Phase B1 BB Wheel Design Report," Tech. Rep. issue 1, Oerlikon Space AG, Zürich / Switzerland, November 2007.
- [26] C. Lange, "Schnittstellenspezifikation_Rad," Tech. Rep. rev 2, RIM-RAD-DLR-004-0-2, DLR - German Aerospace Centre, June 2011.
- [27] DFKI, "Dokumentation Arbeitspaket AP6100 Spezifikation / Definition Demonstrator," Tech. Rep. issue 1, DFKI Bremen - Robotics Innovation Center, June 2010.
- [28] C. Grimm, C. Lange, and R. Rosta, "Wheel Design Report," Tech. Rep. RIM-RAD-DLR-006-0-1, DLR - German Aerospace Centre, July 2011.
- [29] K. Heller, "Entwicklung und Bewertung mechanischer Konzepte zur Variation der Steifigkeit an adaptiven Rädern für weiche Untergründe," bachelor thesis, Universität Bremen, Fachbereich Produktionstechnik, January 2011.
- [30] M. Scharringhausen, "Beviameter Calibration Report," Tech. Rep. rev 2, DLR - German Aerospace Centre, August 2010.

- [31] N. Patel, “ExoMars Rover Flexible Wheel Distortion Occurrence Report (OCR),” Tech. Rep. EXM.RM.OCR.ASU.001, EADS Astrium (UK), August 2008.
- [32] M. Scharringhausen, A. Brucks, and L. Richter, “LSS Phase B1 Breadboard Wheel Distortion NC - Strain Gauge Measurements During Wheel Torsion Test,” Tech. Rep. issue 1, DLR - German Aerospace Centre, November 2008.
- [33] W. Bauer and O. Romberg, “ExoMars Rover Wheel Distortion Investigation.” Internal presentation at DLR, February 2009.
- [34] N. Ozog, “Lab Notes - Introduction to Electronics and Electromechanics: Linear Solenoid Actuator.” University of British Columbia, January 2011.
- [35] C. Grimm, “Adjustable Stiffness Concept Trade-off,” Tech. Rep. rev 2, RIM-RAD-DLR-001-0-1, DLR - German Aerospace Centre, July 2011.
- [36] D. Gross et al, *Technische Mechanik 2 - Elastostatic*. Springer-Verlag, 8th ed., 2005.
- [37] E. Bisshopp and D. Drucker, “Large Deflection of Cantilever Beams,” *Quarterly of applied Math*, vol. 3, pp. 272–275, 1945.
- [38] L. Howell, *Compliant Mechanisms*. John Wiley & Sons, Inc., 2001.
- [39] T. Lovett, “Beams - Beam Buckling.” <http://www.ejsong.com/mdme/modules/FEA/Beams.htm>, accessed on June 25, 2011.
- [40] R. Gessel, “About the Curve of a Free Hanging Rope.” <http://members.chello.nl/j.beentjes3/Ruud/catfiles/catenary.pdf>, accessed on May 23, 2011.
- [41] K. Hughes, J.C. Brown, and T. De Vuyst, “Lecture Notes - Applied Finite Element Modelling: Tips, Tricks and Good Practise.” Cranfield University, 2011.
- [42] University of Ljubljana, “Lecture Notes - Applied Metallurgy: Introduction to the Engineering Properties of Steels.” Faculty for Civil and Geodetic Engineering, University of Ljubljana, Slovenija, 2011.
- [43] Pedaling History Bicycle Museum, “A Quick History of Bicycles.” <http://www.pedalinghistory.com/PHhistory.html>, accessed on June 7, 2011.
- [44] www.astounding.org.uk, “Bicycle Wheel Analysis.” <http://www.astounding.org.uk/ian/wheel/>, accessed on June 7, 2011.
- [45] S. Brown, “Wheelbuilding.” <http://www.sheldonbrown.com/wheelbuild.html>, accessed on June 7, 2011.
- [46] Eidgenössische Technische Hochschule Zürich, “Biegebeanspruchte federn - biegestabfedern.” http://diglib.ethz.ch/system/temporary/get_fed.ind18.de.htm, accessed on June 30, 2011.
- [47] K. Hughes, “Lecture Notes - Structural Mechanics: Basic Structural Response Part 2, Truss and Beam Elements.” Cranfield University, 2011.

APPENDIX



STRESS LEVEL DUE TO SIDE SKID

In Section 4.4.2 it has been shown that due to the side skid force the blades are not only bend under the loading but also twisted. The following is an attempt to derive the resulting stress level and to verify the von Mises stress obtained by the simulation.

The overall wheel deformation is a non-linear bending problem, however, if the blades are bent around their width rather than their thicknesses, then we deal with small deflections only and can therefore view the problem as a linear static case. In order to find the resulting stress we first look at the blades with the highest stress level. Blades #4, 4' and #21, 21' are under the highest tension loads and therefore have the highest normal stress level. This can be seen in Figure 4.25, where only normal stresses are present due to the radial wheel deformation. Looking in particular at blade #4, it has a width $w = 20 \text{ mm}$ and a thickness $t = 0.3 \text{ mm}$, but we do not know the exact length of the tensioned blade as the NPC-shape was not fully defined. We therefore estimate the length to be $a = 175 \text{ mm}$, via interpolation. Although the blade is in tension it remains slightly curved which leaves an offset $b = 10 \text{ mm}$ (obtained through interpolation) from the neutral line. Due to this offset the side skid force component acting on this blade, remembering that there are 48 blades in total, is

$$F_{sB4} = \frac{F_s}{48} \quad (\text{A.1})$$

This force produces not only the bending moment

$$M_b = a \cdot F_{sB4} \quad (\text{A.2})$$

but also a torsional moment

$$M_t = b \cdot F_{sB4} \quad (\text{A.3})$$

The normal stress due to the bending moment can then be found from

$$\sigma_{F_s} = \frac{M_b}{I_y} z \quad (\text{A.4})$$

where

$$I_y = \frac{1}{12} t w^3 \quad (\text{A.5})$$

is the second moment of area in bending direction and

$$z = \frac{w}{2} \quad (\text{A.6})$$

the maximal distance from the neutral line of the blade. The torsional moment M_t produces a shear stress, which is given by

$$\tau_{F_s} = \frac{M_t \cdot t}{J_{open}} \quad (\text{A.7})$$

where J_{open} is the torsional constant of an open section

$$J_{open} = \frac{1}{3} w t^3 \quad (\text{A.8})$$

Using equation 4.3 and superimposing the stress from the radial deflection $\sigma_w \approx 64 \text{ N/mm}^2$ (refer to Figure 4.25) with stress from the side skid force σ_{F_s} and τ_{F_s} we find

$$\sigma_v = \sigma_w + \sqrt{\sigma_{F_s}^2 + 3 \cdot \tau_{F_s}^2} \quad (\text{A.9})$$

Assuming that the interpolated length a and the offset b of the blade are good estimates, we find

$$\begin{aligned} F &= 6.25 \text{ N} \\ I_y &= 200 \text{ mm}^4 \\ J_{open} &= 0.18 \text{ mm}^4 \\ M_b &= 1094 \text{ Nmm} \\ M_t &= 62.5 \text{ Nmm} \\ \sigma_{F_s} &= 54.7 \text{ N/mm}^2 \\ \tau_{F_s} &= 104.2 \text{ N/mm}^2 \end{aligned}$$

and with Equation A.9 gives

$$\begin{aligned} \sigma_v &= 64 \text{ N/mm}^2 + \sqrt{(54.7 \text{ N/mm}^2)^2 + 3 (104.2 \text{ N/mm}^2)^2} \\ &= 252.5 \text{ N/mm}^2 \end{aligned}$$

This value is close to the stress level obtained from the simulation (refer to Figures 4.23 and 4.24). It can therefore be argued that the simulation provides reliable results.

B

CAD MODEL

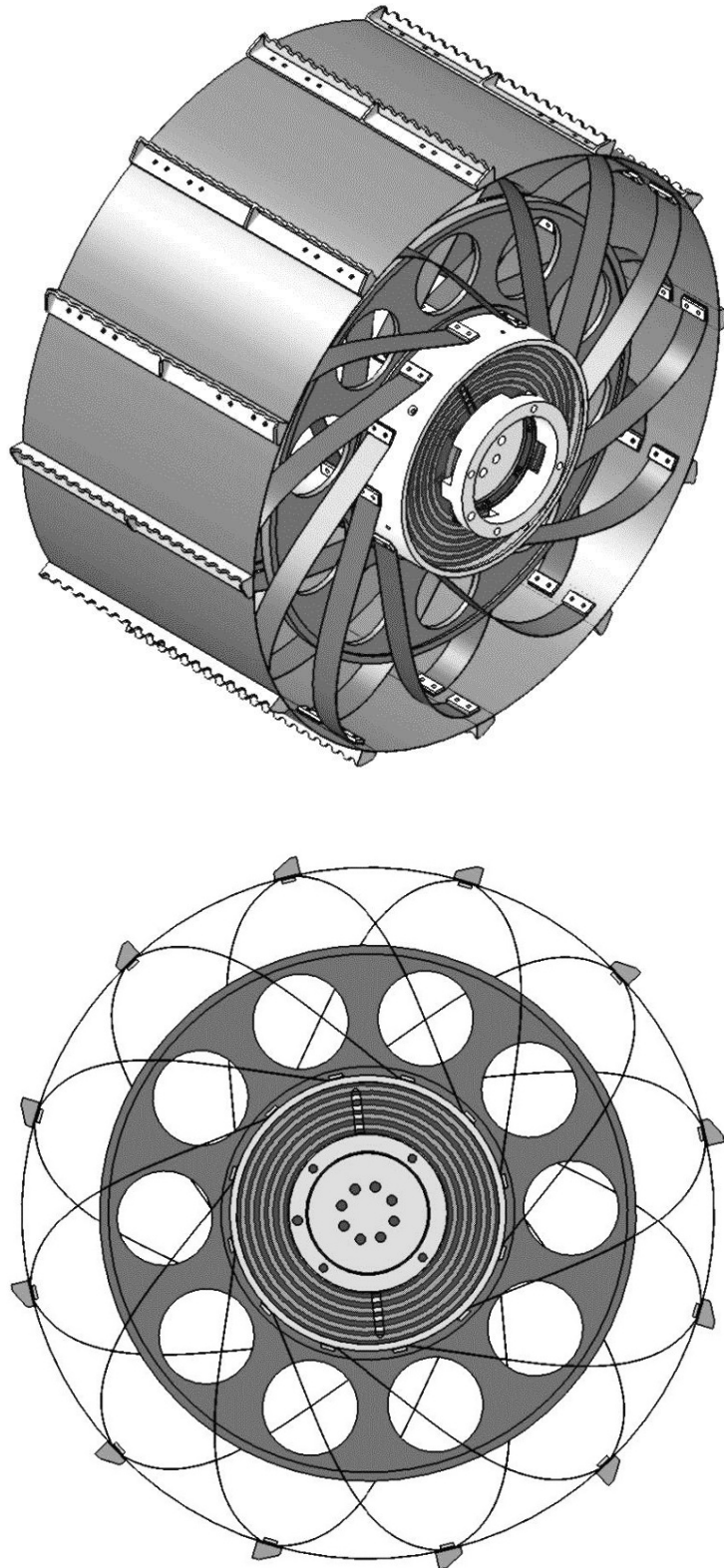
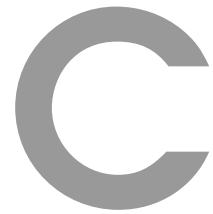


Figure B.1: The new DLR INFLATE (INtelligent FLeXible Adaptive TEnSion-blades) wheel design has a diameter of 400 mm, a width of 200 mm and features flexible metal blades, an included bump stop and an electronic collector ring for sensor data transmission. When loaded, the lower blades will deform and flatten the tread of the wheel to the ground, while the upper blades stretch and carry the load like a bicycle wheel.



DATA SHEETS

Designation	X10CrNi18-8	EN 1.4310	UNS S30100	AISI 301	LMSA D101
-------------	-------------	--------------	---------------	-------------	--------------

Chemical composition (Weight %)

Fe	C	Cr	Ni	Si	Mn	P	S	Mo	N
Balance	0.05-0.15	16.0-19.0	6.0-9.5	≤ 2.0	≤ 2.0	≤ 0.045	≤ 0.015	≤ 0.80	≤ 0.110

In order to achieve maximum homogeneity and consistent quality, the actual tolerances on both alloy components and impurities are significantly tighter and more precisely defined than the standard composition indicated.

Typical chemical composition for Lamineries MATTHEY stainless steel 1.4310.4 (Weight %)

Fe	C	Cr	Ni	Si	Mn
Balance	0.10	17.0	6.5	1.0	1.0

Main technical properties and features

The tensile strengths of austenitic stainless steels are average but can be increased considerably, for certain types, by cold rolling. The 1.4310, X10CrNi18-8, is the most widely used stainless steel for the production of springs. It reaches very high mechanical strength through cold working. Its austenitic structure is rather unstable and its corrosion resistance is lower than, for example, that of the 1.4435, 316L, or of the 1.4301, X5CrNiMo 18-10. An increase of the mechanical strength of the 1.4310, X10CrNi18-8, by more than 250 N/mm² can be achieved by tempering at 280 to 420°C after having been highly cold worked. This tempering is interesting in that it also increases the fatigue strength limit.

Lamineries MATTHEY SA proposes a special version of the 1.4310: the 1.4310.4. Its chemical composition has been adapted in order to increase the reaction to work hardening (Ni content between 6.4 and 6.6%). 1.4310.4 is also specially cast in order to avoid unwanted inclusions. Its austenitic structure is unstable and a high mechanical strength can be reached, using a significantly weaker rate of cold deformation than is the case for the conventional 1.4310. The stainless 1.4310.4 also offers an improved fatigue strength limit as well as a higher increase of the tensile strength after tempering than with the conventional 1.4310. These properties make the 1.4310.4 highly suitable for demanding spring applications such as the manufacture of snap domes.

Typical manufacturing range

		Thickness (mm)	Width (mm)	Length (mm)
Rolled products	Strip in coils ¹⁾	0.010 – 0.400	1.5 - 200.0	-
	Strip as sheets ¹⁾	0.015 – 0.400	10.0 - 200.0	100 - 3000

1) Not all our production possibilities are presented here. Other dimensions or other product forms available upon request. Certain combinations of thicknesses and widths are not possible.

Mechanical properties of strips

Temper	R _{p0.2} (N/mm ²)	R _m (N/mm ²)	Hardness HV
C700 ¹⁾ dead soft	-	700 - 1000	170 - 250
C1000 ¹⁾ soft + skin pass	-	1000 - 1300	310 - 410
C1300 ¹⁾ ¼ hard	≥200	1300 - 1500	390 - 480
C1500 ¹⁾ ½ hard	≥370	1500 - 1800	410 - 520
C1700 ¹⁾ Hard	≥490	1700 - 2000	450 - 630
C1700 ¹⁾ Springs	≥550	≥1900	≥ 580

1) These tempers do not correspond exactly to the EN 10151 standard and are only indicative.

Designation	EN	UNS	AISI	LMSA
X10CrNi18-8	1.4310	S30100	301	D101

Physical properties

Modulus of elasticity	KN/mm ²	195 ¹
Poisson ratio		0.29
Density	kg/dm ³	7.90
Melting point / Melting range	°C	1400-1450
Linear dilatation coefficient (20-300°C)	10 ⁻⁶ /°C	16.8
Thermal conductivity at 20°C	W/m °K	14.7
Electrical resistivity	μΩcm	70
Electrical conductivity	MS/m	1.4
Specific heat at 20°C	J/(kg K)	460
Magnetic properties		Amagnetic in soft temper ²
Permeability		μ = 1.002 - 1.004

- ¹ The Modulus of elasticity of 1.4310.4 varies slightly with the amount of cold working and depends, therefore, on the temper as well as the direction of measurement, longitudinal or transverse to the rolling direction. In the longitudinal direction, the Young's Modulus decreases from approx. 205 kN/mm² in the annealed temper to 185 kN/mm² for a cold working of about 40% (Rm approx. 1400-1600N/mm²) and then increases gradually with further cold working. In all cases, the tempering process will increase the Young's Modulus and decrease its tendency to change as a function of cold working.
- ² The magnetic permeability increases very quickly with cold working and mechanical resistance. For the 1.4310.4, the austenite is very unstable and a significant amount can rapidly change to α - martensite and the alloy will become ferromagnetic (μ_r reaches 6 for a cold working of 50%, Rm approx. 1600 N/mm²).

Typical uses

Often used for the manufacture of springs and other products requiring a good fatigue resistance such as switches, watch and clock components, snap domes, etc.

Bestellbezeichnungen Ordering Code

Tabelle / Table 85.1

Baureihe Series	Baugröße Size	Untersetzung ¹⁾ Ratio ¹⁾					Version Version	Sonderausführung Special design
CSG	14	50	80	100			2UH Unit unit	Nach Kundenanforderung According to customer requirements
	17	50	80	100	120			
	20	50	80	100	120	160		
	25	50	80	100	120	160		
	32	50	80	100	120	160		
	40	50	80	100	120	160		
	45	50	80	100	120	160		
	50		80	100	120	160		
	58		80	100	120	160		
	65		80	100	120	160		
Bestellbezeichnung Ordering Code								
CSG	–	25	–	100	–	2UH	–	SP

¹⁾ Die in der Tabelle aufgeführten Übersetzungsverhältnisse gelten für die Standard-An- und Abtriebsanordnung (CS fixiert, WG Antrieb, FS Abtrieb). Andere Anordnungen sind ebenfalls möglich. Die sich dann ergebenden Übersetzungsverhältnisse entnehmen Sie bitte dem Kapitel „Projektiertechnik“. Bitte geben Sie in Ihrer Bestellbezeichnung unabhängig von der Antriebsanordnung immer eine positive, geradzahlige Untersetzung an (z.B.: 100).

¹⁾ The ratios shown here are for a standard driving configuration with the circular spline fixed, the Wave Generator used for the input and the Flexspline attached to the output. Other configurations are possible. Please consult the chapter "Engineering Data". Please indicate a positive, even-numbered ratio in your ordering code (e.g. 100), regardless to the driving arrangement used.



Technische Daten Technical Data

Leistungsdaten

Rating Table

Tabelle / Table 86.1

CSG- ZUH Baugröße	Unter- setzung ¹⁾	Grenze für wieder- holbares Spitzen- drehmoment	Grenze für Durchschnitts- drehmoment	Nennndrehmoment bei Nenndrehzahl 2000 min ⁻¹	Grenze für Kollisions- drehmoment	Max. Antriebsdrehzahl [min ⁻¹]		Grenze für mittlere Antriebsdrehzahl [min ⁻¹]		Massen- trägheits- moment ⁴⁾	Gewicht
Size	Ratio ¹⁾	Limit for repeated peak torque	Limit for average torque	Rated torque at rated speed 2000 rpm	Limit for momentary peak torque	Max. input speed [rpm]		Limit for average input speed [rpm]		Moment of inertia ⁴⁾	Weight
	i	T _R [Nm]	T _A [Nm]	T _N [Nm]	T _M [Nm]	Öl ²⁾ Oil ²⁾	Fett ³⁾ Grease ³⁾	Öl ²⁾ Oil ²⁾	Fett ³⁾ Grease ³⁾	[kgm ²]	[kg]
14	50	23	9	7	46	14000	8500	6500	3500	0,033x10 ⁴	0,52
	80	30	14	10	61						
	100	36	14	10	70						
17	50	44	34	21	91	10000	7300	6500	3500	0,079x10 ⁴	0,68
	80	56	35	29	113						
	100	70	51	31	143						
20	120	70	51	31	112	10000	6500	6500	3500	0,193x10 ⁴	0,98
	50	73	44	33	127						
	80	96	61	44	165						
25	100	107	64	52	191	7500	5600	5600	3500	0,413x10 ⁴	1,5
	120	113	64	52	191						
	160	120	64	52	191						
32	50	127	72	51	242	7000	4800	4600	3500	1,69x10 ⁴	3,2
	80	178	113	82	332						
	100	204	140	87	369						
40	120	217	140	87	395	5600	4000	3600	3000	4,5x10 ⁴	5
	160	229	140	87	408						
	50	281	140	99	497						
45	80	395	217	153	738	5000	3800	3300	3000	8,68x10 ⁴	7
	100	433	281	178	841						
	120	459	281	178	892						
50	160	484	281	178	892	4500	3500	3000	2500	12,5x10 ⁴	8,9
	50	523	255	178	892						
	80	675	369	268	1270						
58	100	738	484	345	1400	4000	3000	2700	2200	27,3x10 ⁴	14,6
	120	802	586	382	1530						
	160	841	586	382	1530						
65	50	650	345	229	1235	3500	2800	2400	1900	46,8x10 ⁴	20,9
	80	918	507	407	1651						
	100	982	650	459	2041						
	120	1070	806	523	2288	3000	2500	2200	1900		
	160	1147	819	523	2483						
	80	1223	675	484	2418						
	100	1274	866	611	2678	2800	2400	2000	1700		
	120	1404	1057	688	2678						
	160	1534	1096	688	3185						
	80	1924	1001	714	3185	2500	2000	1700	1400		
	100	2067	1378	905	4137						
	120	2236	1547	969	4329						
	160	2392	1573	969	4459	2200	1800	1500	1200		
	80	2743	1352	969	4836						
	100	2990	1976	1236	6175						
	120	3263	2041	1236	6175	1900	1600	1300	1000		
	160	3419	2041	1236	6175						

¹⁾ Diese Untersetzungen sind gültig für eine An- und Abtriebsanordnung gemäß Variante Nr. 1, s. S. 395. Bitte berücksichtigen Sie, dass sich die in der Tabelle genannten Untersetzungen je nach An- und Abtriebsanordnung ändern.

²⁾ Ölschmierung ist optional möglich. Gegebenenfalls müssen die Gehäuseabmessungen bei Ölschmierung geändert werden. Bitte Rücksprache mit der Harmonic Drive AG.

³⁾ Gültig bei Fettschmierung mit Harmonic Drive SK-1A Fett für die Baugrößen 20 bis 65 und SK-2 für die Baugrößen 14 und 17.

⁴⁾ Das angegebene Massenträgheitsmoment bezieht sich auf die Antriebsseite und gilt für einen Standard Wave Generator.

¹⁾ The ratios refer to driving arrangements according to variant no.1, see page 395. Please note that the ratios quoted in the table may change depending on the driving arrangement.

²⁾ Oil lubrication only as option. The housing dimensions may have to be changed for oil lubrication. Please ask Harmonic Drive AG.

³⁾ Applicable for Harmonic Drive SK-1A grease for sizes 20 to 65 or SK-2 for sizes 14 and 17.

⁴⁾ The moment of inertia refers to the input side and is valid for a standard Wave Generator.

T30R0C2

Cable Tie, 30lb, 5.9", Max Bun Dia. 1.38" PA66 Black, 100/Pk

Article Number: 111-00438

Part Number: T30R0C2

Type: T30R

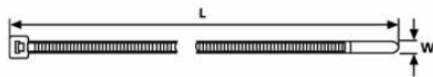


- [→ Find a Distributor](#)
- [→ Order Samples](#)
- [→ Get Technical Drawings](#)

1. Base Data


Part No.	T30R0C2
Type	T30R
Color	Black
Features	HellermannTyton manufactures a full line of high quality cable ties in a variety of styles, sizes, materials, and colors. HellermannTyton cable ties are engineered and manufactured for maximum performance and quality.
Application	Used to bundle and secure wire and cable.
Application Method	Quick, simple fixing by hand or with HellermannTyton tensioning tools
Identification Plate Position	none
Releasable Closure (Yes/No)	No
Tie Closure	plastic pawl

2. Product Dimensions



Min. Tensile Strength	30 lbs / 135 N
Length (L)	5.9 " / 150 mm
Width (W)	.14 " / 3.5 mm
Min. Ø Bundle	.06 " / 1.5 mm
Max. Ø Bundle	1.38 " / 35.0 mm

4. Material and Specifications

Material	Polyamide 6.6 (PA66) / PA66
Certification	MIL 53421 / UL ZOD22.E64139
CSA Certified	No
Flammability	UL94 V2
Material Specification	HF / RoHS
Operating Temperature	-40 °F to +185 °F (-40 °C to +85 °C) continuous
ROHS Conformity	

Logistic and Packaging

Packaging Type	bag
Pkg. Qty.	100
Carton Qty.	5000
UPC	08930607560

